Production of resonances by pions

Kitchen, C. A.

ABSTRACT

of the Thesis

"Production of Resonances by Pions"

presented by C. A. KITCHEN

for the degree of Doctor of Philosophy

January, 1967.

This thesis contains a description of investigations that have been undertaken to examine the inelastic interactions of positively charged pi-mesons with protons. The experiment was carried out at the European Centre for Nuclear Research in Geneva using a separated beam of 5 GeV/c pions produced by the 27 GeV Proton Synchrotron. Pictures were taken of the interactions of the pions with the protons of the 150 cm. British National Hydrogen Bubble Chamber.

To analyse the interactions recorded on the films of the chamber a digitized measuring apparatus was constructed. The machine provided data about the interactions encoded in a suitable manner for automatic processing. The numerical and statistical methods used in the computation of the most probable dynamical interpretation of each interaction are given.

In the sample of these high multiplicity interactions that have six or seven particles in the final state of the reaction, evidence was found for the production of intermediate particles or resonances.

The statistical analysis carried out was consistent with a large production of the well-known resonances $N^{*}3/2, \rho^{o}, \omega^{o}$ which decay in to two or three particles. Apart from a small number of X^{o} particles, no evidence was found for a large production of any other resonances including those of which the $N^{*}3/2, \rho^{o}$, and ω^{o} constitute one of the decay products. The production of resonances in high multiplicity interactions therefore does not proceed by the quasi two-body mode which has been shown to be a dominant feature of the lower multiplicity interaction.

It was found that the mechanism of resonance production in 4, 5 and 6 body intermediate states could not be described adequately by the statistical model. The distributions of dynamical parameters showed similar effects to those observed for the peripheral production of resonance in the quasi two-body mode of lower multiplicity interactions.

Preface

This thesis is an account of the work carried out by the author whilst at Durham University and contains a description of the investigations made into various aspects of the interactions of pi-mesons with the protons of a liquid hydrogen bubble chamber. The work on the analysis of the six-pronged events forms the first part of a general experiment on the interactions of 5 GeV/c positive pions with protons undertaken by the High Energy Physics Group of Durham University in collaboration with similar groups from the Universities of Bonn, Nijmegen, Paris (E.P.) and Turin.

The author was concerned with all stages of the experiment, the exposure at C.E.R.N., the analysis of the events in Durham and the investigation of the results undertaken in Bonn, Durham and Paris. Specific contributions by his collaborators are clearly indicated.

PRODUCTION OF RESONANCES BY PIONS

A thesis presented

by

Cedric Alan Kitchen B.Sc.

for the

Degree of Doctor of Philosophy

at the

University of Durham

January 1967

CONTENTS

LIST OF TABLES

Tables

LIST OF FIGURES

Chapter 1

Chapter 2

Chapter 3

Introduction

The construction of the present generation of powerful particle accelerators has enabled physicists to produce monoenergetic beams of the well known particles with high energies and high fluxes. They have been used to make far more searching studies into the fundamental structure of matter.

The forces giving rise to interactions between the elementary particles are classified in terms of the strength of the interaction into strong, electro-magnetic, weak and gravitational. It is with the strongly interacting particles - the so-called "Hadrons", that this thesis is mainly concerned and especially those inelastic interactions producing many secondary particles.

A significant contribution to the previous work in the field of inelastic reactions has been carried out using bubble chambers which constitute the most versatile technique at present available in that they provide a complete and permanent record, on film, of all the different types of interactions.

The dominant feature of these investigations has been the discovery of a large number of resonances and the determination of their properties of lifetime, spin, parity etc. Although the question of describing these short-lived particles as elementary is somewhat of a philosophical nature, it has been clearly

demonstrated that there do exist meaningful relationships of one with respect to another. These relationships are provided by a Group Theoretical approach to the quantum numbers of the resonant states.

In Chapter 1 a review is given of the Symmetry schemes that have been applied to the particles and resonances together with a description of the theoretical models proposed to explain the dynamical mechanism of their production in the lower multiplicity events. This is then compared with the situation for higher multiplicity interactions.

The second and third chapters contain a survey of the exposure undertaken at C.E.R.N. and the methods used to analyse the interactions recorded on the film of the chamber.

The results obtained from the experiment are presented in Chapter 4 and discussed in the light of the topics reviewed in the first chapter.

CHAPTER 1

REVIEW OF INELASTIC INTERACTIONS

1.0 Resonances

A natural consequence of the discovery of so many new resonances having well defined quantum numbers has been the attempts to arrange the particles into groups or multiplets according to their properties. This work has now been extended from the familiar representations of spin and isotopic spin with the SU_2 group to higher symmetry schemes such as SU_3 and SU_6 which conserve both isotopic spin and hypercharge.

SU_3

The eight charged states of the well known baryons p, n, Λ^o, Σ and Ξ were for a long time considered as obvious candidates to occupy some higher symmetry multiplet. Gell-Mann (1961) and Ne'eman (1961) were able to derive a representation for them in the simplest generalization of isotopic spin viz. the unitary, unimodular 3x3 matrices of the SU_3 group. In this formulation there arises an 8 component unitary spin which, with symmetry breaking, reduces to conservation of isotopic spin and hypercharge.

As well as the octet for the baryons, this group also gives other representations for the pseudo-scalar and vector mesons in terms of singlets and octets and a decuplet for the baryon isobars

The applications of the SU_3 group have met with some remarkable successes which include the accurate prediction of the mass assignments within the multiplets by the Gell-Mann - Okubo Mass Formula (1962) and the subsequent discovery of the Ω^- (Barnes et al. 1964).

SU_6

The SU_3 symmetry of the known elementary particles has been interpreted (Gursey, Radicati and Zweig 1964) in terms of bound states of more fundamental systems of unknown, fractionally-charged particles - the "quarks". This approach has led to an extension of the symmetry to that of the SU_6 group by assuming that the quarks possess spin which gives rise to the observed scheme of spin assignments for the SU_3 multiplets.

For the mesons, considered as bound states of quark and anti-quark, the SU_6 group for the "s" state interaction gives rise to a singlet of spin, parity assignment $J^p = 0^-$ and a 35-fold multiplet which comprises a 0^- octet and a 1^- nonet. Higher orbital angular momentum states of the quark - anti-quark system give the higher mesons multiplets in this scheme.

In this model, the baryons are considered to be the bound states of three quarks and the totally symmetric "s" state of these three gives rise to a 56-fold multiplet which decomposes into the $1/2^+$ octet and the $3/2^+$ decuplet.

Particle Classification

The process of assigning particles and resonances to particular multiplets has lead to a consistent scheme for many of the well known resonances e.g. the 0^- nonet containing the η, X^o, π and K, the 1^- nonet containing the ω, ϕ, ρ and K^* (891) and the 2^+ nonet with the f^o (1253), f' (1500) A_2 and K^* (1405). There exists, however, considerable doubt as to the correct assignments for the less firmly established resonances, which should be resolved with the availability of more experimental data.

The present knowledge of the nucleonic isobars is more extensive due to the availability of accurate πN total cross-sections obtained from formation experiments as well as the usual data obtained with production experiments in track chambers. Recent advances in phase shift analysis (Donnachie and Lea 1965, and Bransden et al. 1965) have revealed new resonances that may be assigned, according to their spins, to the various octets and decuplets for the baryons. There are still however gaps in these multiplets with respect to undiscovered strange baryons.

Although SU_6 has achieved good results for particle masses and magnetic moments, it suffers from the inherent failing of being non-relativistic. Attempts to remedy this fault by extending the system to an even higher, but extensively broken

symmetry e.g. the $\tilde{U}12$ group proposed by Salam (1965) have not yet been successful. These symmetries require the existence of very large or possibly infinite multiplets of high spins and perhaps also higher isotopic spins depending upon the nature of the interaction forces between the quarks.

There is good experimental evidence for the existence of some multiparticle resonances that may be considered as excited states of the well established two and three particle resonances such as the ω^{o}, ς and η etc. It is to be expected therefore that if there are other such states that are still undiscovered, they too will have multi-particle decay schemes in a manner similar to that observed for the A_1, A_2, X^{o} and B resonances. Consequently it will become necessary to investigate the high multiplicity interactions more fully than hitherto in order to find them.

1.1 Production Mechanisms

General

Mesonic and baryonic resonances are produced in a large proportion of the inelastic events as for example in the reaction

$$K^+ p \rightarrow K^o \pi^+ p \ldots\ldots \quad \text{at 3 GeV/c}$$

studied by Ferro-Luzzi et al. (1964) where the K^* (892) resonant state of the $K^o\pi^+$ system and the N^* (1236) resonant state of the π^+p system, occur in 80% of all events.

In four and five body particle final states this effect of quasi two body interactions is still quite marked with combined production of two resonances in the intermediate state being a prominent feature. For example in the reaction

$$\pi^+ p \rightarrow \pi^+ \pi^+ \pi^- p \ldots\ldots \quad \text{at 3.65 GeV/c}$$

investigated by Goldhaber et al. (1964), it was found that the production of the resonant states of the $\rho\pi$ system, the A_1 and A_2, occurred in 10% of the events. Furthermore there was also some 34% of combined production of either ρ^o (763) or of f^o(1250) together with an N^* (1236) giving a quasi two body reaction in 44% of all events by the reactions

$$\pi^+ p \rightarrow \begin{cases} A_1^+ p \\ \quad \hookrightarrow \pi^+ \rho^o \\ \qquad \hookrightarrow \pi^+\pi^- \end{cases}$$

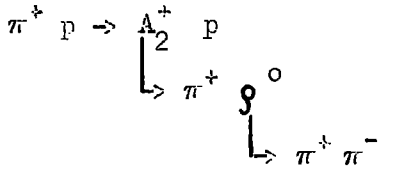

and 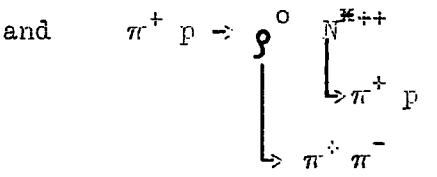

or 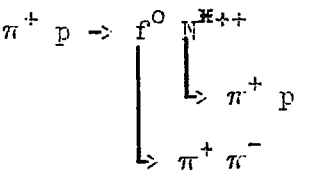

These estimates of resonance production at present constitute only a lower limit because of the inability of resolving the many small contributions of known and unknown resonances.

One of the first models proposed to describe high energy inelastic collisions of the hadrons was the Statistical model of Fermi (1950) which required the production of a single short-lived composite state that decayed to give a symmetrical distribution of its decay products in the overall centre of mass system.

The study of the production mechanism of the resonances in these quasi two-body reactions soon revealed a preference for small four-momentum transfers between the primary and target particles. This effect is strikingly demonstrated by the angular distributions of the secondary resonances in the overall centre of mass system. The reaction products appear to be strongly collimated with the secondary particles maintaining the same general direction as those of the intial beam and target particles.

The predominance of small four-momentum transfers implies the existence of long range forces that may be attributed to the scattering of the incident particle by the mesic cloud surrounding the baryon. The interaction takes place with the exchange of a virtual particle and the production amplitude is dominanted by the nearby singularity in the invariant mass distribution of the exchange particle.

The Peripheral Model

The Peripheral Model was introduced by Geobel (1958) and Chew and Low (1959) to give a simple explanation of the observed preference for low four-momentum transfers in the quasi two-body inelastic interactions of the type

$$a + b \rightarrow c + d$$

This process is illustrated in the Feynmann diagram given in Fig. 1 where c and d may be resonances.

As shown by Pilkhun (1965), the amplitude for such an interaction may be described in terms of the sum of all the different one particle exchange amplitudes

$$T = T_p + T_v + T_b + \cdots\cdots$$

where T_p is the amplitude for the exchange of a pseudo-scalar meson, T_v, that for a vector meson and T_b is the amplitude for baryon exchange. In each specific reaction the contributions to this amplitude will only come from those particles that satisfy

Fig. 1

Feynmann Diagram of Quasi-two-particle Interaction.

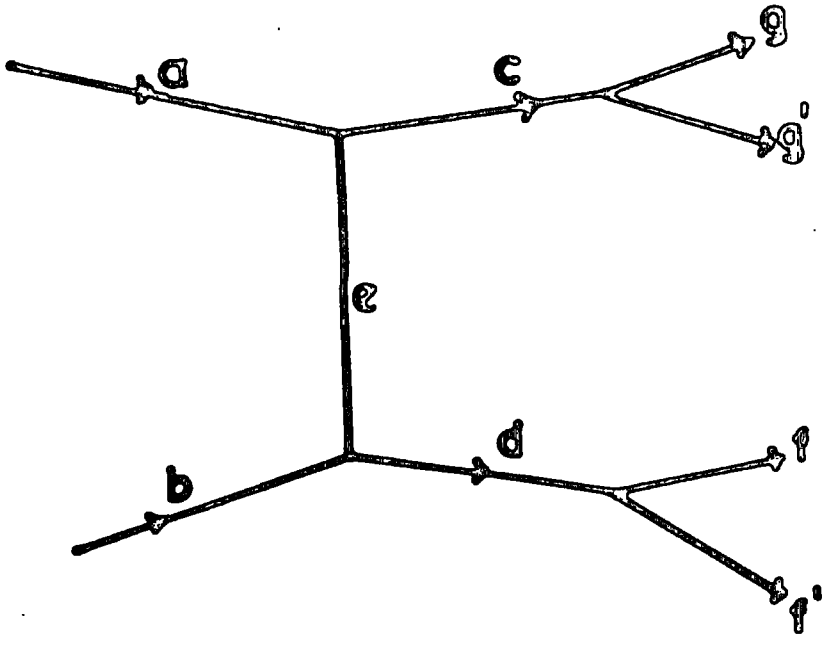

the strong interaction conservation laws at both vertices. The individual amplitudes for such particles may be expressed, with the aid of the Feynmann Rules, in lowest order Perturbation Theory as the product of three terms; a term "V" for each vertex and a term for the propagator of the exchange particle. Thus

$$T(s.t) = V_{aec}(t) \cdot \frac{F(s.t)}{(m_e^2 - t)} \cdot V_{bed} \qquad \ldots (1)$$

with the well known Mandelstam variables s,t and u defined in terms of the four-momenta a, b, c and d of the particles as

$$s = (a + b)^2 = (c + d)^2$$
$$t = (b - d)^2 = (c - a)^2$$

and

$$u = (a - d)^2 = (c - b)^2$$

The differential cross-section, $d\sigma$, is then given by

$$d\sigma = \text{const.} \left| T \right|^2 \cdot d\phi_s \qquad \ldots (2)$$

where ϕ_s is the Lorentz invariant phase space.

At first the form of the vertex functions could only be approximated by the appropriate scattering amplitudes and the effect of the propagator on the differential cross-section for production $d\sigma/dt$, was studied. This term has a pole in the unphysical region at $t = -m_e^2$. Extrapolation into the physical region, therefore, should yield distributions more sharply peaked for the exchange of particles of lower mass in the region of low t where

$$T_p >> T_v >> T_b$$

Such distinctions in the distributions of $d\sigma/dt$ are apparent in those reactions where both a and c are pseudo-scalar mesons and pion exchange is forbidden, and also in $p\bar{p}$ reactions where the main contribution comes from baryon exchange.

Form Factors

It was found, however, that the distributions of $d\sigma/dt$ for resonance production were much more sharply peaked at lower values of t than would be expected from the propagator term alone.

With the discovery of more resonances and the determination of their quantum numbers, it became possible to calculate the form of the vertex functions. For example in the combined production of baryon isobars and vector mesons it has been shown (Jackson 1964) that for the exchange of a pseudo-scalar meson the vertex functions are given by

$$V_{aec} = i.g_{aec}.(a - e).\epsilon^{\lambda}$$

$$V_{bed} = G_{bed}.\gamma_5$$

where g and G are coupling constants that may be evaluated from the experimentally determined decay widths of the resonances and ϵ^{λ} represents the polarization of the vector meson. The amplitude for the process then becomes:

$$T_p = i.g_{aec}.G_{bed}.(a-e).\epsilon^{\lambda}\,\bar{u}_j\,(d).\gamma_5.u_j(b)\,\frac{F_p(t)}{(m_p^2-t)} \quad \ldots (3)$$

As discussed by Huff (1964) the angular distributions for the decay of c may be suitably described by the angle between the incoming particle and one of the out-going particles in the rest

system of the resonance. The polarisation vector $e^{(\lambda)}$ can then be replaced by a unit vector in the direction of this decay particle.

In such a system as illustrated in Fig. 2 the decay distributions are described in terms of the two angles θ and ϕ where the latter is related to the Treimann-Yang angle. The spin-density coefficients, ρ_{ij}, are dependent upon the nature of the exchange particle so that in the general distribution $W(\theta,\phi)$ for a $J = 1$ particle

$$W(\theta,\phi) = \frac{3}{4}\rho_{oo}\cos^2\theta + \rho_{11}\sin^2\theta - \rho_{1,-1}\sin^2\theta.\cos 2\phi - 2\mathrm{Re}\,\rho_{10}\sin 2\theta.\cos\phi \quad \ldots\ (4)$$

The decay of a $(1^- \Rightarrow 0^-0^-)$ produced by pseudo-scalar exchange requires that only the ρ_{oo} coefficient be non-zero. The resulting amplitude obtained by averaging over the spin of the baryon and decay of the vector meson is

$$\frac{d\sigma_p}{dtd} = \frac{\pi}{sq^2}\,\frac{g^2}{4\pi}\,\frac{G^2}{4\pi}\cdot\left|\frac{F_p(t)}{m_p^2-t}\right|^2\cdot a_c^2\left[(m_b-m_d)^2-t\right]\cos^2\theta \quad \ldots\ (5)$$

If, however, the baryon vertex produces a spin $3/2$ resonance such as the $N^*(1236)$ then the vertex is modified to become

$$V_{bed} = \frac{G^*}{m_p}\cdot e_\mu$$

Fig. 2

DIAGRAM OF DECAY OF DIPION IN ITS OWN REST SYSTEM

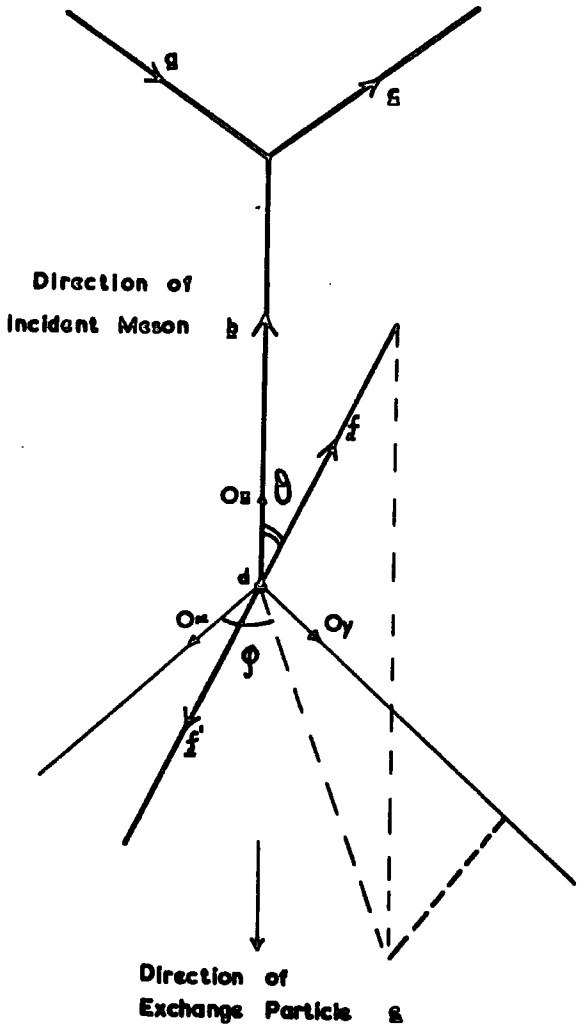

$$Ox = \frac{q \wedge c}{|q \wedge c|}$$

$$Oy = Oz \wedge Oy$$

$$Oz = \frac{b}{|b|}$$

the corresponding amplitude is

$$T_p = i.g.\frac{G^*}{m_p} . (a - e)\epsilon^{\lambda} \bar{U}_{\mu}^{(j')}(d)\ e_{\mu}.u_j(b) . \frac{F_p(t)}{(m_p^2-t)} \qquad .... (6)$$

The evaluation of the cross-section is performed by summing over the isobaric spins giving

$$\frac{d\sigma_p}{dt} = \frac{2\pi}{3sq^2} . \frac{g^2}{4\pi} . \frac{G^{*2}}{4\pi} . \left| \frac{F_p(t)}{(m_p^2-t)} \right|^2 . \frac{a_c^2-b_d^2}{m_p^2} \left[(m_b+m_d)^2-t\right] \qquad .... (7)$$

where

$$a_c^2 = \frac{1}{4m_c^2} . (t - (m_a-m_c)^2).(t - (m_a-m_c)^2)$$

and

$$b_d^2 = \frac{1}{4m_d^2} . (t - (m_b-m_d)^2).(t - (m_a+m_d)^2)$$

The term $F_p(t)$ is a form factor introduced initially by Ferrari and Selleri (1962) who assumed that the vertex and propagator functions have renormalizations effects that involve unknown functions of t.

In order to achieve reasonable fits with the experimental data on the differential cross-sections quite steeply varying function are required for the form factors. The effect of these empirical factors is to mask the original t dependence of the propagator which reflects the inadequacy of the simple peripheral model.

Absorption Model

In an attempt to explain the reason for this discrepancy Sopokovich (1962) postulated that the one particle exchange

interactions are modified by elastic scattering in the initial and final states as illustrated in Fig. 3. The exchange particle amplitudes are multiplied by the S-matrix elements for the scattering in the initial and final states for each total angular momentum channel.

i.e. $$T^{j'} = S_{ab}(j).S_{cd}(j).T^{j}$$

Various derivations of these S-matrix elements have been put forward by Sopokovich, Omnes (1965) and Ball and Frazer (1965), all of which give rise to a suppression of the lower angular momentum channels. This model has been used (Svensson 1964) with additional form factors for the vertices developed from angular momentum barrier considerations to simulate the data of the Anglo-German collaboration on the differential cross-section for production of the resonances in the reaction

$$\pi^{+} p \rightarrow N^{*++} \omega^{o} \quad \ldots\ldots \text{ at } 4 \text{ GeV/c}$$

Similar studies have been undertaken (Morrison et al. 1966) for double resonance production in 8 GeV/c π^{+} p interactions. The density matrix elements evaluated from the decay angular correlations of the two resonances compare well with the predictions of the Absorption Model. For those reactions, however, where the exchange of a ϱ meson is postulated and not a pion as in

$$\pi^{+} p \rightarrow N^{*++} \omega^{o}$$

FIG. 3

FEYNMANN DIAGRAM OF ONE PARTICLE EXCHANGE PROCESS WITH ABSORPTION

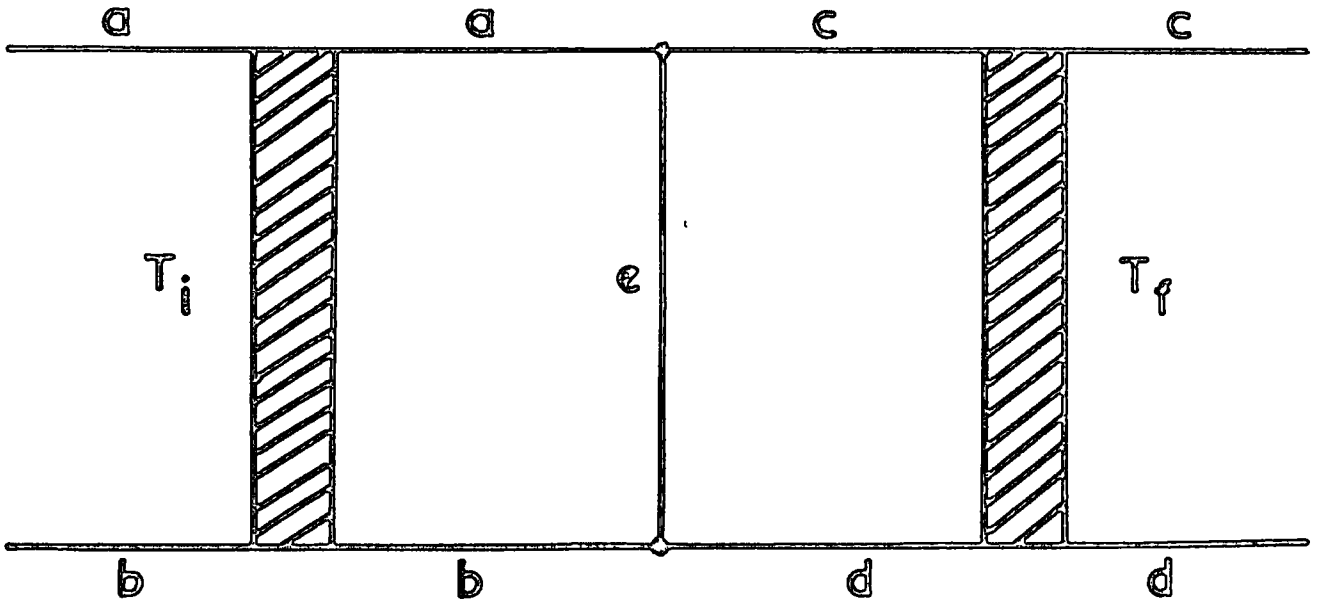

the agreement with the experimental distributions of the differential cross-section is not very good. Much better agreement to the distributions of those reactions requiring vector meson exchange has been obtained with the Regge pole model.

Regge Pole Model

In this model the reactions are considered in terms of the exchange of the Regge trajectory on which the particle lies. For reactions requiring the exchange of a pseudo-scalar meson or a vector meson then the corresponding R or ρ trajectories dominate. In the region of low t , it is believed that the R and ρ trajectories tend to be parallel. Therefore similar differential cross-sections are expected for both reactions despite the large disparity in the masses of the two particles.

Detailed calculations (Thews 1966) have yielded good agreement with the experimental data on the reaction

$$\pi^+ p \rightarrow N^{*++} \pi^o \quad \ldots\ldots\ldots \text{ at } 2.75,\ 3.54,\ 4.0 \text{ and } 8.0 \text{ GeV/c}$$

and

$$K^+ p \rightarrow N^{*++} K^o \quad \ldots\ldots\ldots \text{ at } 3.0,\ 3.5 \text{ and } 5.0 \text{ GeV/c}$$

Further support for this model is provided by the data on the variation of cross-section of inelastic quasi two body reactions with the incident momentum. An analysis of available data (Morrison 1966) has shown that the distributions may be well represented by an empirical function of the form

$$\sigma = \text{const.} \left(\frac{P}{P_o}\right)^{-n}$$

where the constant is universal, depending only on a common normalization of P_o, and the exponent may be related to the Regge trajectory that is dominant in the exchange process. As the differential cross-section $d\sigma/dt$ in Regge theory is related to the trajectory $\alpha(t)$ by

$$d\sigma/dt = \text{const.}\ s^{2.\alpha(t)-2}$$

then, for small values of t where most of the reaction takes place, the integrated differential cross-section σ should be approximately equal to $s^{-2\alpha(0)-2}$. Thus for high primary momenta when s is directly proportional to P the exponent "n" should be approximately equal to $2.\alpha(t) - 2$. These relations are found to be correct for reactions in which only one resonance is produced but agreement is not so close for those reactions where two resonances are produced. This discrepancy is thought to arise from the difficulty of estimating the proportion of combined resonance production.

At present, unfortunately, no one has been able to reconcile the successful features of the Absorption Model in predicting angular correlations and the Regge pole model in describing differential cross-sections in to one unified model.

1.2 Higher Multiplicity Interactions

Experimental situation

At the present time very little work has been published on interactions with a high multiplicity of secondary particles i.e. those interactions producing six or more particles in the final state. Although the cross-section for these is small for incident pions with energies below 3 GeV, it appears to rise rapidly above this energy as illustrated in Fig. 4 where some of the available data on the six-prong cross-section of positive pions is plotted. Furthermore, at 11.7 GeV/c preliminary scanning statistics obtained in this laboratory indicate that the six-pronged events have a cross-section $\sigma \simeq 3.6$ mb and that eight-pronged events are quite common ($\sigma \simeq 0.8$ mb) and some ten-pronged events have been observed.

In the energy region above 1 GeV it is found that the total reaction cross-section and elastic cross-section for the interactions of pions and protons with nucleons is almost constant as shown in Fig. 5. Therefore the contribution to the inelastic cross-section of higher multiplicity interactions is increasing with primary energy. This trend is supported by the data available from cosmic ray experiments where large multiplicity interactions are observed (Peters 1966). Thus it would seem reasonable to assume that events of large

FIG.4

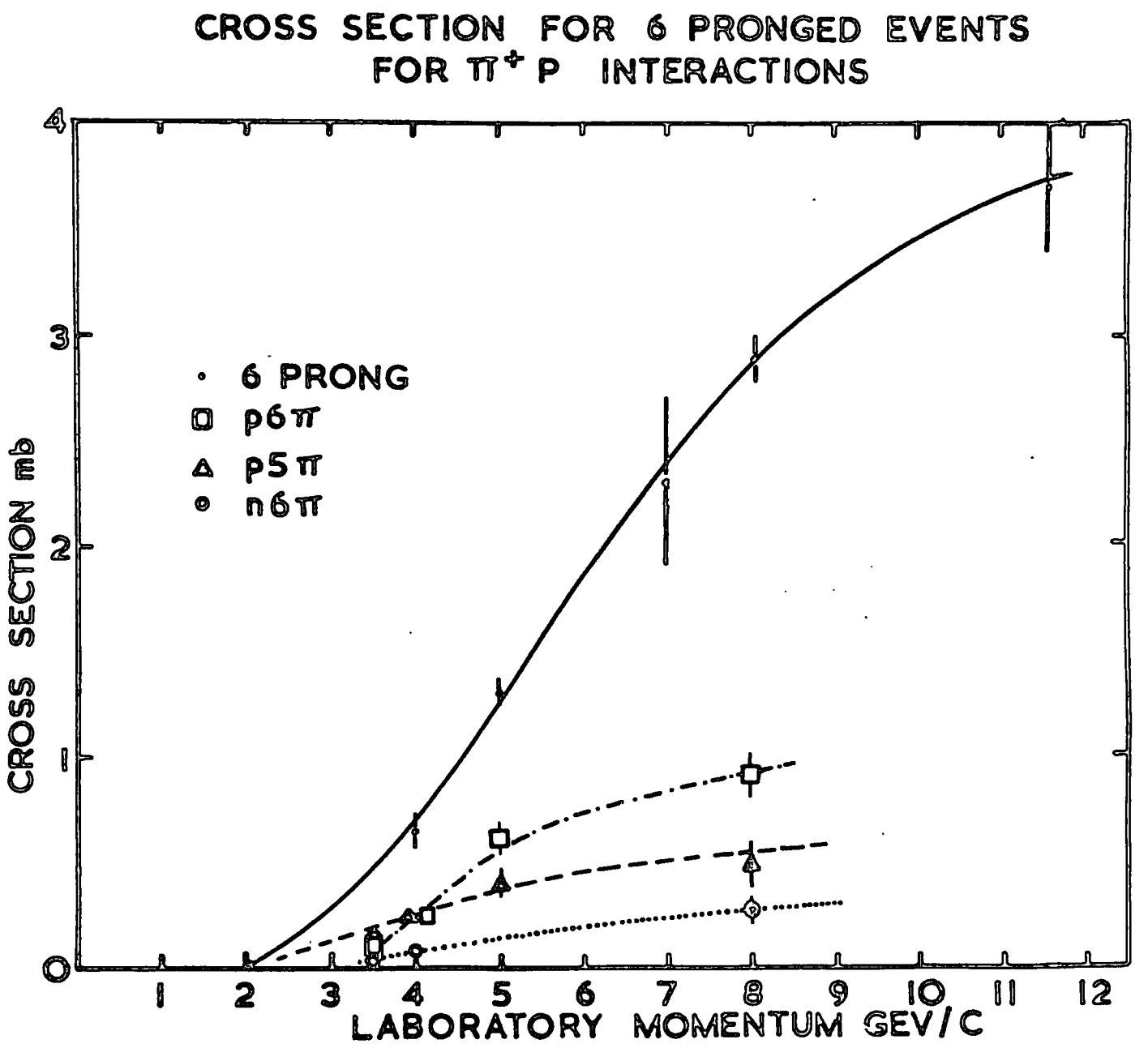
CROSS SECTION FOR 6 PRONGED EVENTS
FOR π⁺ P INTERACTIONS
6 PRONG
p6π
p5π
n6π
CROSS SECTION mb
LABORATORY MOMENTUM GEV/C
0
1
2
3
4
1
2
3
4
5
6
7
8
9
10
11
12

FIG. 5

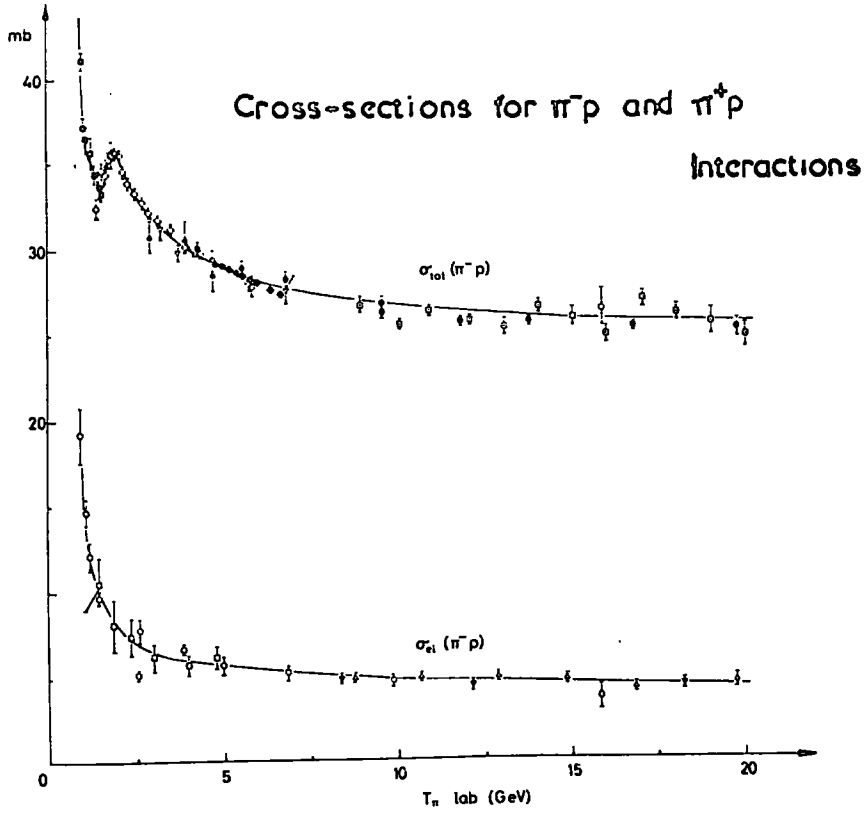
Cross-sections for π⁻p and π⁺p
Interactions
mb
40
30
20
0
5
10
15
20
σ_{tot} (π⁻p)
σ_{el} (π⁻p)
T_π lab (GeV)

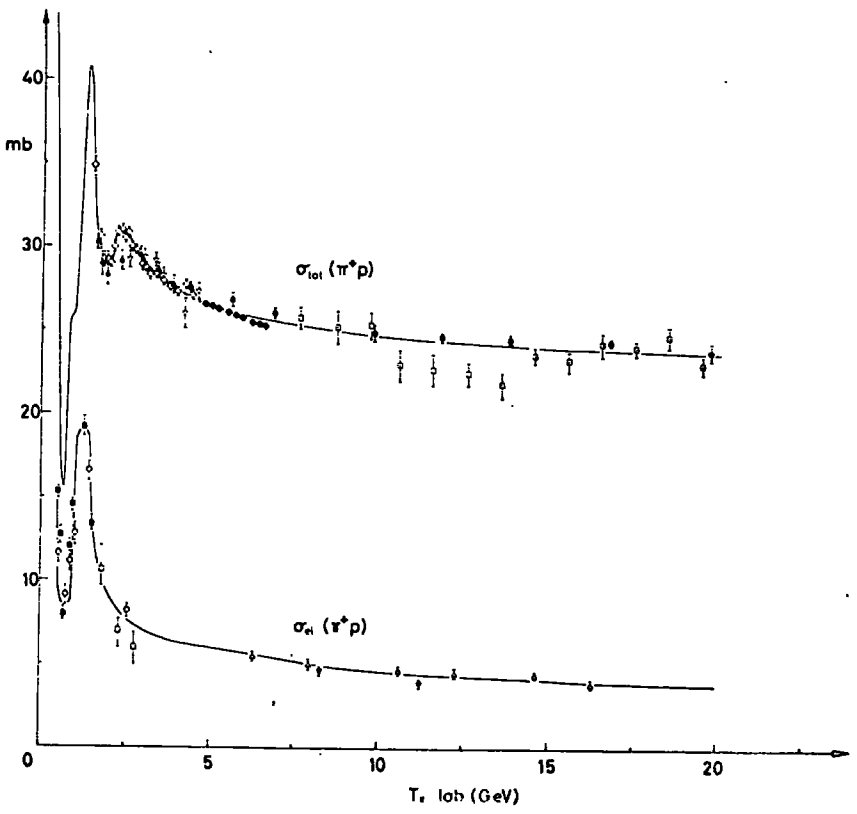
mb
40
30
20
10
0
5
10
15
20
σ_{tot} (π⁺p)
σ_{el} (π⁺p)
T_π lab (GeV)

multiplicites are the dominant feature of inelastic interactions at the higher energies.

The previous experiments in this field have been carried out at 4.0 GeV/c (ABBHM Collaboration 1966) and 8.0 GeV/c (Bardidin et al. 1966 and Bartke et al. 1966) for π^+p, 10.0 GeV/c (Bardidin et al. 1966) for π^-p and $\bar{p}p$ at 3.25 GeV/c (Ferbel 1963) and 5.7 GeV/c (French et al. 1966). These experiments all find strong production of the well known two and three particle resonances such as the $N^*(1236)$ and the ρ^o and ω^o. Apart from a few examples of $X^o(950)$ production and a small percentage of $N^*(3.68)$ reported for the eight-pronged events at 8.0 GeV/c, no new multi-pion or higher baryon resonances have been found. Although such states may still be undiscovered as the statistics in all these experiments is small, it now seems clear that quasi two-body production does not form a major process in these collisions.

Production Processes

In an attempt to try and explain the production of multi-particle final states in inelastic interactions Amati and Fubini and Stanghellini (1962) introduced the Multi-Peripheral Model. In this model the concept of peripheral production was extended in to the realm of multiple particle production by processes involving a large number of vertices. Assuming the feasibility of such complex processes as that illustrated in

Fig. 6(a) they derive general conclusions about the dominant multi-vertex graph at each energy and also the behaviour of the total amplitude in the limit of high energies.

This principle has been used by Joseph and Pilkhun (1964) in a "Double-Peripheral Model" which envisages a three vertex graph, Fig. 6(b), with two particles being exchanged. Their model contains assumptions on the nature of the vertex at which the two exchange particles are joined to the real particle. By using the vacuum, pi and the rho as three possible exchange particles, together with the appropriate form factors, they were able to derive differential cross-sections that compare favourably with the data of the Anglo-German collaboration for the inelastic interactions at 4 GeV/c:

$$\pi^+ \, p \Rightarrow \pi^+ \pi^o \, P$$

In the previous experiment there does indeed appear to be some degree of forward-backward collimation of the secondary particles in these high multiplicity interactions. For the comparatively low energies, however, at which machine experiments are performed the resulting assymetries are not always sharply defined. This feature has lead Bartke and Cyszewski (1966) to postulate that high multiplicity events can be divided between central (i.e. statistical) and peripheral collisions, with no sharp limit separating the two types. In the limit of low energy and high multiplicity an extrapolation from the available

Fig. 6

(a) Feynmann Diagram of Multi-Peripheral Interaction

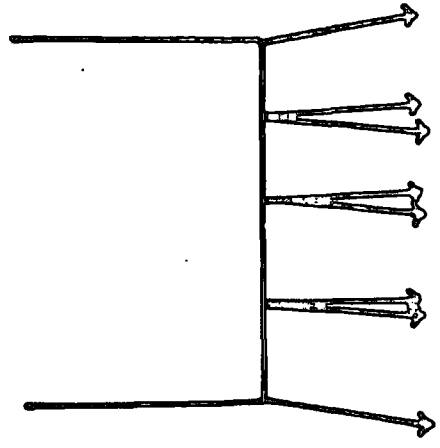

(b) Feynmann Diagram of Double-Peripheral Interaction

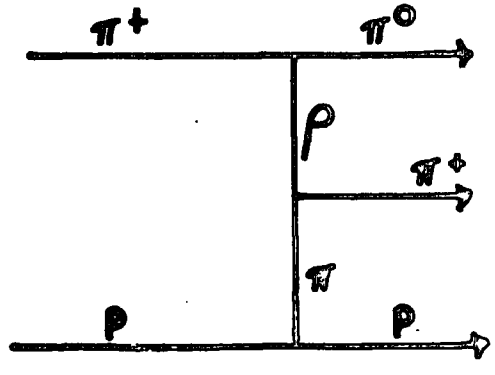

data reveals a total lack of any observable assymetries. Further support for this view of a high degree of "central" collisions is provided by their investigations in to the distributions of final states in pure isospin space. For the data already available these distributions are approximately equal to the predictions of the statistical model.

The purpose of the present experiment has been to make more complete study of high multiplicity interactions with increased statistics compared with previous experiments, in order to clarify the position concerning the contribution of resonances and their production mechanisms.

CHAPTER 2

THE EXPERIMENTAL CONDITIONS OF THE EXPOSURE

2.0 Introduction

The film of the interactions of 5 GeV/c positive pions with protons was obtained in three separate exposures at the C.E.R.N. Proton Synchroton. The O_2 beam and the British National Hydrogen Bubble Chamber, (B.N.H.B.C.), were used for this experiment. Throughout each run the beam was operated by members of the collaboration and the author was one of the representatives of the Durham group.

The collaboration members also investigated the "test-strips" from the films taken of the chamber (c.f. Section 2.3). The information obtained from these test-strips was used to optimise the operating conditions for the beam and the chamber.

Secondary tests were performed on the complete films which indicated that instabilities due to camera malfunctions existed in the films taken during October and November of 1964 which rendered them useless for analysis. The instabilities were not found to be present in the film taken during February of 1965 and hence only these 150,000 pictures were analysed.

An estimate of the magnitude of the errors due to the chamber was made by measuring beam tracks in a film taken with

no (i.e. ≤ 4 gauss) magnetic field present.

2.1 The O_2 Beam

General

The O_2 beam was constructed in the East Experimental area of the C.E.R.N. Proton Synchrotron in order to supply the B.N.H.B.C. with reasonably pure beams of pions, kaons, protons and anti-protons at many different momenta up to 15 GeV/c. The complex beam designed by E. Keil and W. Neale (1963) to fulfill this difficult role contained many separate components including both electrostatic and radio-frequency separators. Either of these two types of separator could be used to cover a wide range of momenta; the radio-frequency separators being more effective at the higher particle energies.

For ease of operation, all the collimators of the beam were remotely adjustable and in order to reduce the contamination due to scattered particles, all the vertical and horizontal images were separated.

The beam consists of three separate stages of analysis. Initially those particles lying within the correct momentum interval were selected. The second stage of mass analysis used the electrostatic separators which were more suited to the lower momentum of 5 GeV/c for the pions in this experiment. In the final stage the momentum selection was redefined and the beam shaped for entry in to the chamber.

Beam Layout

The layout of the various components of the 180 m long beam is illustrated in Fig. 7. When the circulating protons in the synchrotron had attained an energy of 19.6 GeV, the beryllium target was placed in their path for a period of approximately 1 millisecond. The secondary particles produced were shielded by an iron pipe, B.P., from the effects of the fringing field of the following magnet in the synchrotron ring.

The angular acceptance for secondary particles was defined by the product of the target area and the vertical and horizontal apertures of collimators C_1 and C_2. The quadrupole lens triplet Q_1, Q_2 and Q_3 produced horizontal and vertical images at the centers of collimators C_3 and C_4 respectively while the bending magnets M_1 and M_2 produced dispersion in the horizontal image at C_3 where momentum selection took place.

The quadrupole magnet Q_4 together with the bending magnets M_3 and M_4 subsequently removed the dispersion from the beam. The lens triplet Q_4, Q_6 and Q_7 produced an intermediate horizontal focus within the electrostatic separators and the triplet Q_{10}, Q_{11} and Q_{12} produced a vertical focus at the collimator C_6 where mass analysis was performed.

The triplet Q_{13}, Q_{14} and Q_{15} refocussed the beam on to the

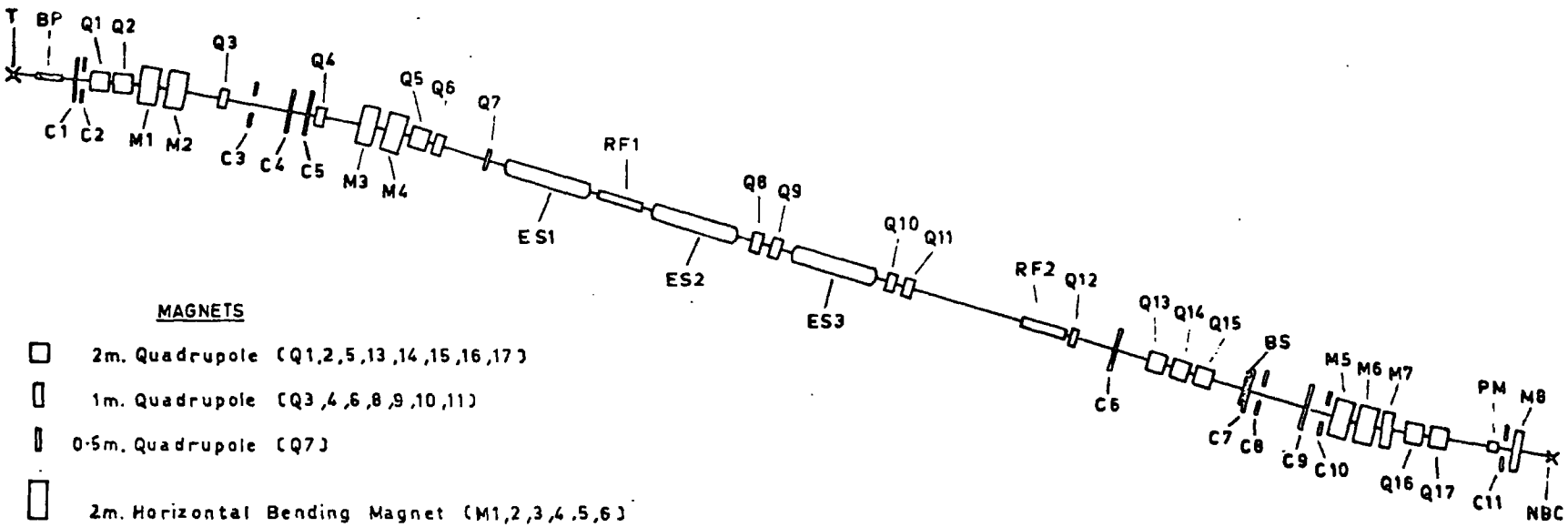

MAGNETS

- 2m. Quadrupole (Q1,2,5,13,14,15,16,17)
- 1m. Quadrupole (Q3,4,6,8,9,10,11)
- 0·5m. Quadrupole (Q7)
- 2m. Horizontal Bending Magnet (M1,2,3,4,5,6)
- 1m. Vertical Bending Magnet (M7,8)
- 1m. Pulsed Vertical Bending Magnet (PM)

SEPARATORS

- Electrostatic Separator (ES1,2,3)
- Radiofrequency Separator (RF1,2)

COLLIMATORS

- Horizontal Collimator (C2,3,8,10,11)
- Vertical Collimator (C1,4,5,6,7,9)
- Beam Stopper (BS)

T : Target

NBC : Bubble Chamber

Fig. 7

SCHEMATIC DIAGRAM OF O_2 BEAM LAYOUT

collimators C_7 and C_8 in the horizontal and vertical planes respectively. The angular acceptance was redefined in the vertical plane by C_9 and in the horizontal plane by the gap of the vertical bending magnet M_7. The momentum acceptance was redefined by the production of a dispersed horizontal image at C_{11} by the bending magnets M_5 and M_6 together with the lens doublet Q_{16} and Q_{17}.

Bending magnets M_7 and M_8 steered the beam into the chamber and the doublet Q_{16} and Q_{17} produced a slight divergence.

The number of particles entering the chamber was limited by the action of the pulsed magnet P.M. whose operation could be delayed with respect to the beam arrival time in order to allow sufficient particles to enter the chamber.

Tuning the Beam

All the magnet currents and the electrostatic separators voltages were set to the values determined with the beam analysis program TRAMP. The operation of the beam was monitored by three counters. The first of these was an "Agoritsus" type counter, (A), positioned near the target to give a measure of number of secondary particles produced. The other two were a Cerenkov counter which was positioned near the Beam-stopper, B.S., and a coincidence counter, (C), consisting of two scintillators, one located next to the

Cerenkov counter and the other just before the chamber. The number registered by the Cerenkov counter for each beam pulse was displayed in a binary form on the films of the bubble-chamber and for stable operating conditions this number bears a linear relationship with the number of particles entering the chamber.

The A and C counters were used in both stages of the process of "tuning" the beam which required the pulsed magnet to be switched off. The mass analysis part of the beam was tuned by obtaining the maximum of the peak due to the pions in the distribution of coincidence counts per 1,000 A counts as a function of the current in the magnet of E.S.3. The momentum redefinition was also optimised to correspond with the initial selection by determining the maximum value of the same distribution but this time as a function of the currents in magnets M_5 and M_6.

Running

The beam intensity of the synchrotron, A counts and C counters were monitored continuously in order to detect any large-scale changes in the operating conditions. The fluctuations observed were due mainly to the variations of the beam intensity, A. Some adjustments of the apertures of the collimators and the delay of the pulsed magnet were required to maintain an average number of about 12 beam particles entering

the chamber.

Furthermore, the currents in the bending magnets and the voltages across the electro-static separators were checked at regular intervals. The magnet currents were found to be extremely stable to within ~ 0.1% and required very little resetting. However, some drift was observed on the voltages of the separators. These drifts necessitated frequent retuning of the mass analysis stage which was carried out during convenient delays in the operation of the chamber, such as the periods of film changing.

2.2 The B.N.L.B.C.

The Chamber

The liquid hydrogen chamber of the B.N.L.B.C. consists of a single machined aluminium casting with a large annular clear section of internal dimensions 152 x 50 x 46 cms. This annular section is closed at either side by two 155 mm thick, plane-parallel, glass windows of high optical quality (Welford 1963). Each window is protected by a hydrogen shield, S, as shown in Fig. 3, and the whole system is enclosed in a stainless steel vacuum tank, V, to reduce thermal losses.

Operation

The chamber contains some 500 litres of liquid hydrogen at a temperature of $27^{o}K$ and an absolute pressure of 6.3 Kgs./cm.^{2}. The surface of the liquid hydrogen is in the vertical expansion-pipes going from the top of the chamber to the expansion valves. When the valves are opened the pressure at the surface of the liquid hydrogen falls rapidly to 2.8 Kgs./cm^{2}. causing the liquid to become superheated so that boiling will occur in areas of high charge density within the volume of the liquid caused by the passage of a charged particle.

The chamber is operated repetitively with a cycle time of 2 seconds. In order to achieve synchronous operation with the arrival of the beam particles the expansion of the chamber

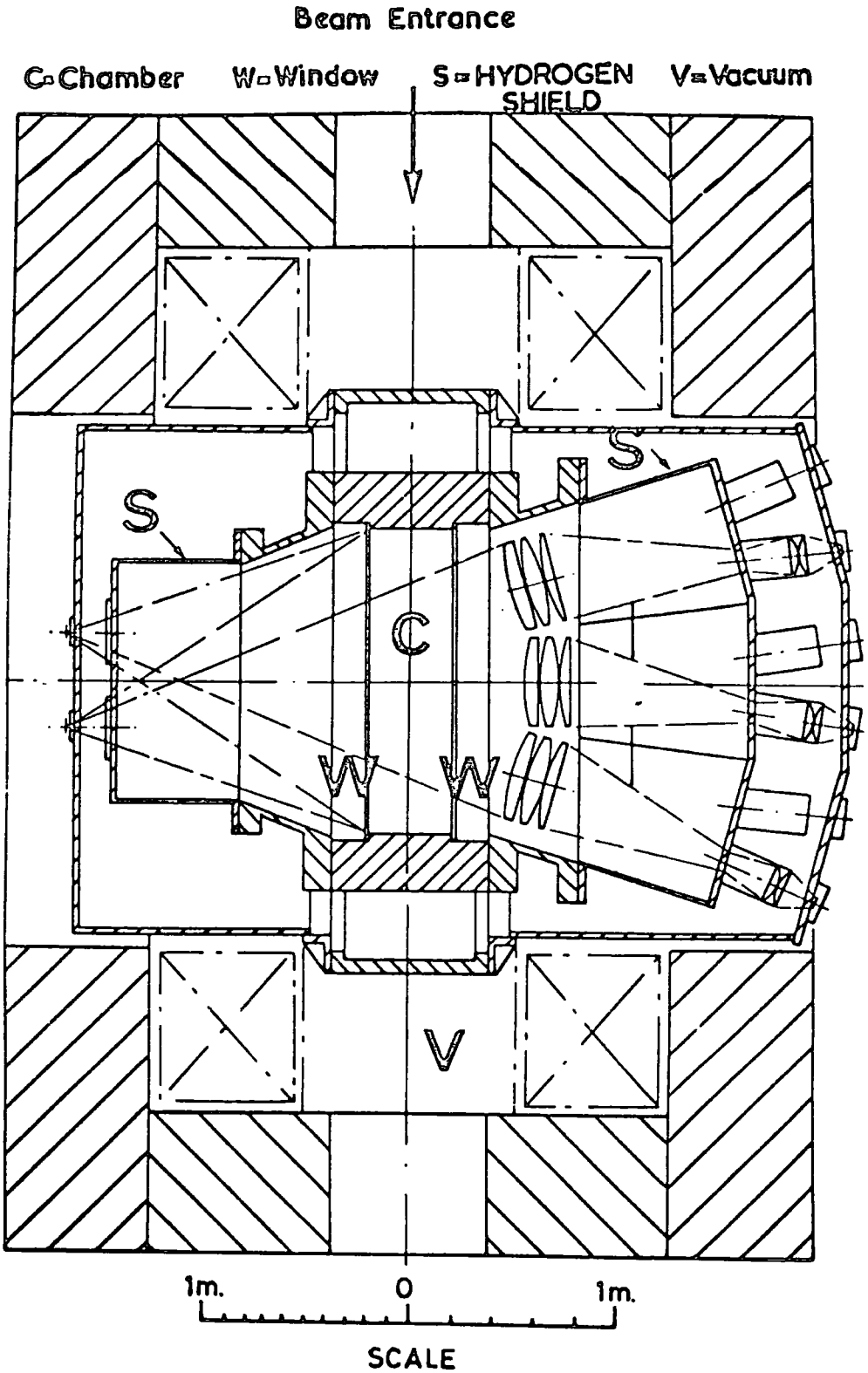

FIG. 8 PLAN VIEW OF B.N.H.B.C. SHOWING OPTICAL SYSTEM AND MAGNET.

is initiated by a signal from the accelerator. Some 30 milliseconds are required for the complete expansion and to attain the superheated conditions which is maintained for 2 milliseconds before recompression starts. Recompression lasts approximately 10 milliseconds but a much longer time interval of about 100 milliseconds is required before the liquid level stabilises and the turbulence within the chamber has subsided.

The Magnetic Field

Surrounding the vacuum tank is a large electro-magnet weighing 30 tons which gives a nearly uniform magnetic field over the volume of the chamber liquid. This field has been mapped (W. Blum 1964) and shows a deviation of 3% over the complete volume. This effect is taken in to account in the reconstruction of the events.

The magnitude of the magnetic field is variable up to 14.8 K.gauss and could be kept constant to within 0.1%.

Photographic System

The B.N.H.B.C. uses the "through-illumination" light system with three condensers each of which are supplied by three circular neon flash tubes. The directions of the convergent light beams of the condensers are such that the cameras only record images due to light scattering centers within the chamber

such as the bubbles within the liquid or fiducial marks etched upon the surfaces of the windows. The geometry of this layout is designed to give a lower limit for the scattering angle of 2^{o} with respect to the median plane of the chamber (Welford 1964).

The objective lenses of the cameras are mounted on to the same baseplate in a triangular array as shown in Fig. 9 and the images recorded by these three cameras are referred to as Views I, II and III.

The flash tubes were triggered by a pulse from the C counter of the beam. Their operation was delayed to the latter part of the 2 millisecond period during which the chamber was sensitive in order to give the bubbles sufficient time to grow. The films were automatically wound on after each expansion.

Picture Layout

In addition to the picture of the chamber there was flashed on to each film an image of the illuminated "data-board" containing numeric data specifying the serial number of the expansion, the date and time when the picture was taken, the magnet current and the Cerenkov counter reading.

Furthermore, images of a set of four fiducial crosses were produced by illuminating etched glass plugs set into the metal surface of the camera gates. These "camera-based

FIG. 9

SCHEMATIC DIAGRAM OF CAMERA LAYOUT

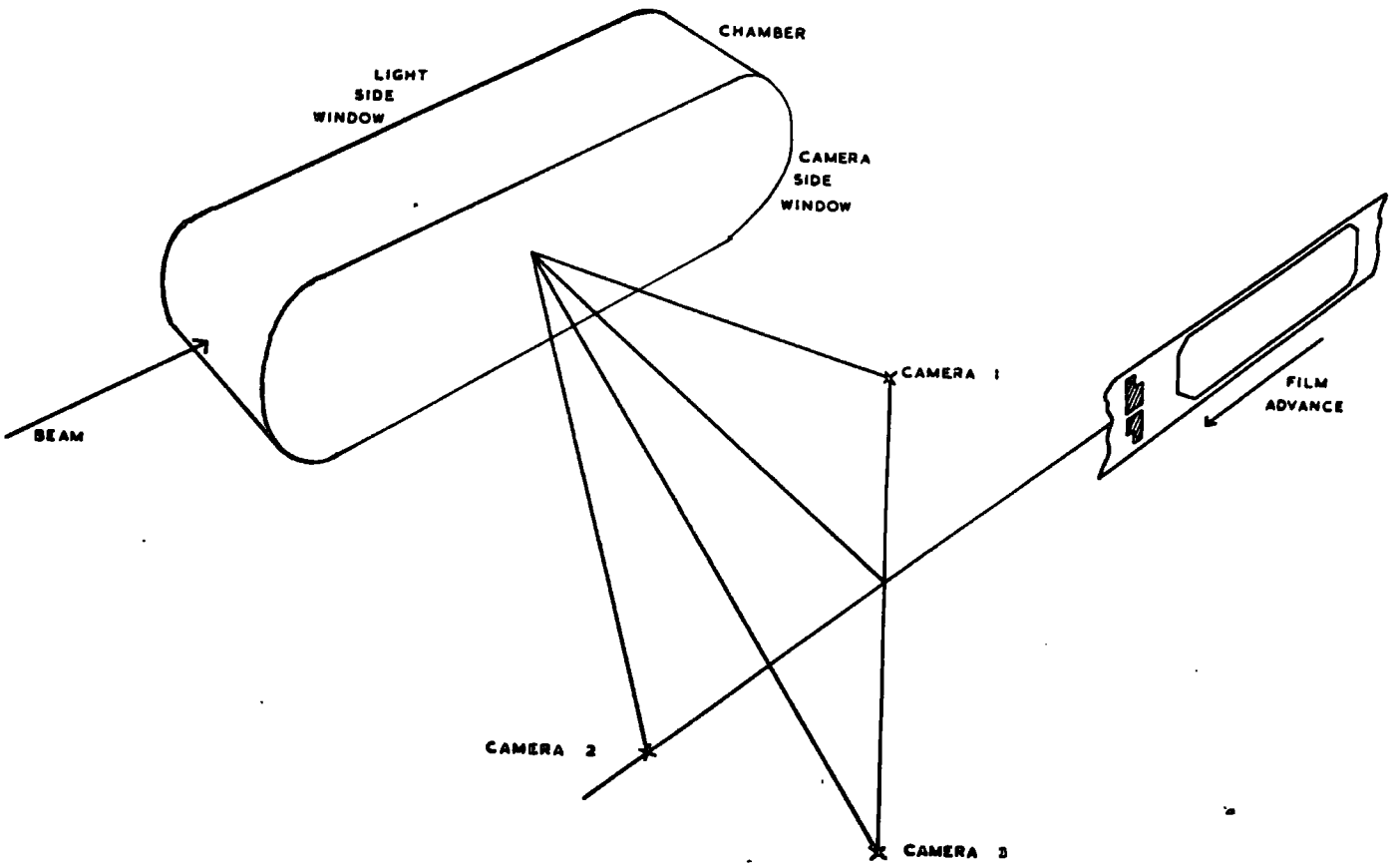

fiducials" were essential for determining the lens distortions of the cameras objectives as they provided the only co-ordinate system on the films that was independent of the lenses.

2.3 Monitoring the Film

General

The cassettes of the cameras could hold 300 m of film which is sufficient for 2,500 pictures. It was necessary to cut this film in the middle to give two separate films of 1250 pictures which could be accommodated on the normal I.E.P. spools. Approximately 20 frames from the end of each film were removed and developed immediately after exposure. These test strips were used to provide a rapid check on the behaviour of the various components so that any faults could be corrected as quickly as possible.

Picture Quality

The three views were required to have good, clear images of the chamber and the data-board, which are correctly spaced so that no images were overlaid.

A lack of contrast in any region of the image of the chamber indicated that the appropriate flash tube was not working. Throughout all the films taken an area of dirt was observed to be accumulating near the bottom of one of the chamber windows but this never spread sufficiently to interfere with the subsequent analysis of the film.

Beam

The behaviour of the beam components was investigated by observations on the beam tracks within the chamber. The

number of tracks in each frame was counted and compared with the number registered by the Cerenkov counter which was displayed on the data-board. If the correlation between the two numbers had changed it indicated that there had been a change in the operating conditions of the beam.

The vertical spread and the depth distribution of the beam were investigated to see if the quadrupole magnets Q_{16} and Q_{17} were shaping the beam correctly and whether it was being steered in to the chamber in a direction parallel with the windows.

Chamber

The bubble density of the beam tracks was investigated by a gap-counting technique using a low-powered microscope. The values of the density obtained were compared with those from a "standard" frame of good quality. Any significant deviations from this standard were corrected by adjusting the 2 milliseconds sensitive period of the chamber with respect to the arrival time of the beam.

The size of the bubbles was also examined to see if the pulsing of the flash tubes had been delayed sufficiently to give the bubbles enough time to grow. Furthermore, slight changes in the operating conditions of temperature and pressure for the chamber were possible to optimise the size and density of the bubbles.

It was found possible to utilise some of the films with tracks that would normally have been considered too faint for measurement, by overdeveloping them.

2.4 Secondary Tests

General

Two further tests were made on the complete films to ensure that there existed no large random errors that would prohibit their use for analysis. In the film taken in October and November of 1964, instabilities in the configuration of the fiducial crosses were detected by P. Fleury (1965), who investigated the distributions of the squares of the ratios of the measured distances between fiducial crosses in different frames. The distributions obtained fell in to two quite distinct groups; many of the values for the frames subsequently considered as normal are contained within a narrow peak whose width was consistent with the measuring error and a large background of widely scattered values of the ratios in any of the anomalous frames were in error the cause of the instabilities could not be attributed to shrinkage of the film and was thought to be due to the film gates.

The film gates operated by sucking the film against a flat metal surface but the suction was applied only around the edges of the film. This could lead to the film assuming a convex form at the centre of the image and consequently these film gates were replaced in January 1965. The new film gates had suction holes all over the metal surface. In order to

test the quality of the film obtained with these new film gates, a statistical analysis was made on the geometrical configuration of the fiducial crosses using an Algol program FIDO written for the Elliott 803 computer in Durham.

FIDO

This program processes the existing co-ordinate measurements of the fiducial crosses and determines from them the values of two ratios of the squares of the lengths between four specific fiducial crosses. The ratios are then checked to ensure that they lie within a pair of closely defined limits corresponding to the correct geomtrical configuration. A statistical analysis is made of the acceptable values within each film.

For each view a single number, X_ℓ, is derived from the two ratios and the mean of a sample of these numbers is determined together with its standard deviation. The sample is subsequently refined by applying a three standard deviation cut-off.

A total of 18 films were investigated and a total of 50 frames in each film was measured. The mean values, $\bar{X}_\ell$, of the refined samples from these measurements on each of the three views of a frame were determined together with the associated standard deviation $\sigma_{\bar{X}_i}$. The distributions of these mean values and their errors are given in Fig. 10. Out of the original

FIG. 10

DISTRIBUTIONS OF THE MEAN VALUES OF CROSS RATIOS IN EACH FILM AND THEIR ERRORS.

(a). VIEW 1

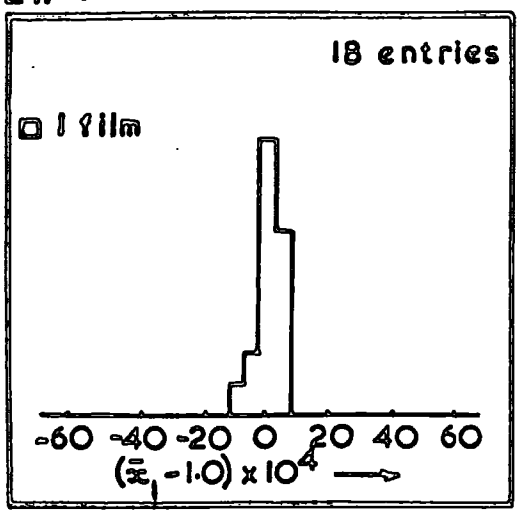

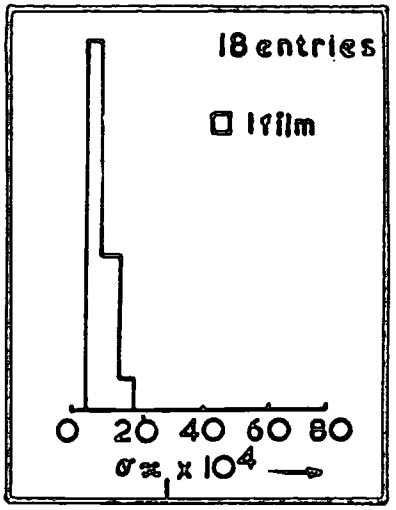

(b). VIEW 2

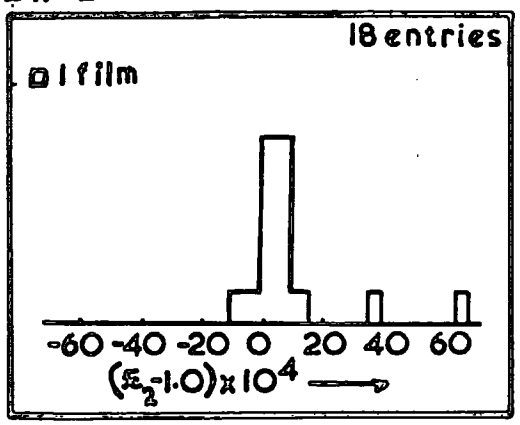

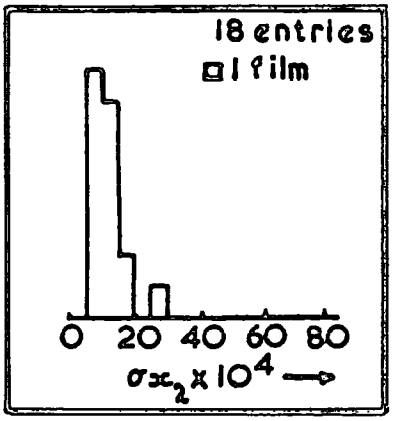

(c) VIEW 3

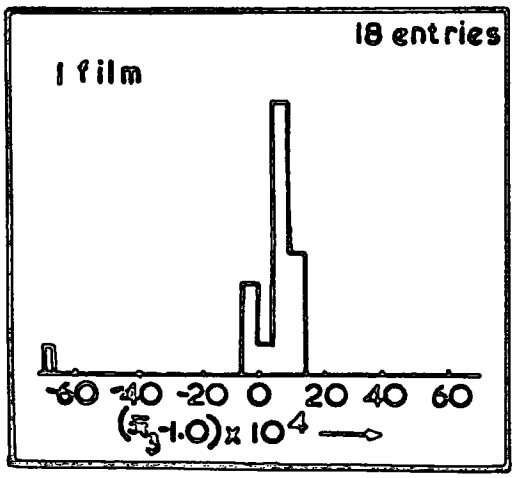

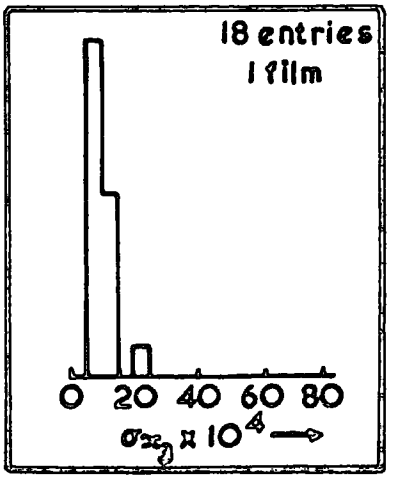

2700 sets of measurements 2352 were accepted for the analysis with 355 of those rejected being definitely identified as wrongly measured and the remaining 93 ambiguous.

Although some of the values of $\bar{X}$ are significantly different from the means of the distributions for views II and III, the corresponding standard deviations are quite comparable with those obtained with the other films. This systematic effect was ascribed to distortion of some films during the development process.

As the mean values of the distributions are constant to within 1% it was considered reasonable to plot the σ_x values for different views on the same graph viz. Fig. 11. Because of the high degree of overlap in the error function for the $\bar{X}$ values in order to compare the characteristics of this distribution with the errors expected from measurement, it was necessary to simulate the analysis by a Monte-Carlo method using the FIDO-SIMULATOR program written for the K.D.F.9 computer.

FIDO SIMULATOR

This program generates the "X" values as used in FIDO by taking co-ordinate positions for the fiducial crosses which have the same geometrical configuration as those on the film. The positions of the crosses are then adjusted by small amounts

FIG. 11

DISTRIBUTION OF ERRORS OF CROSS RATIO FOR ALL VIEWS

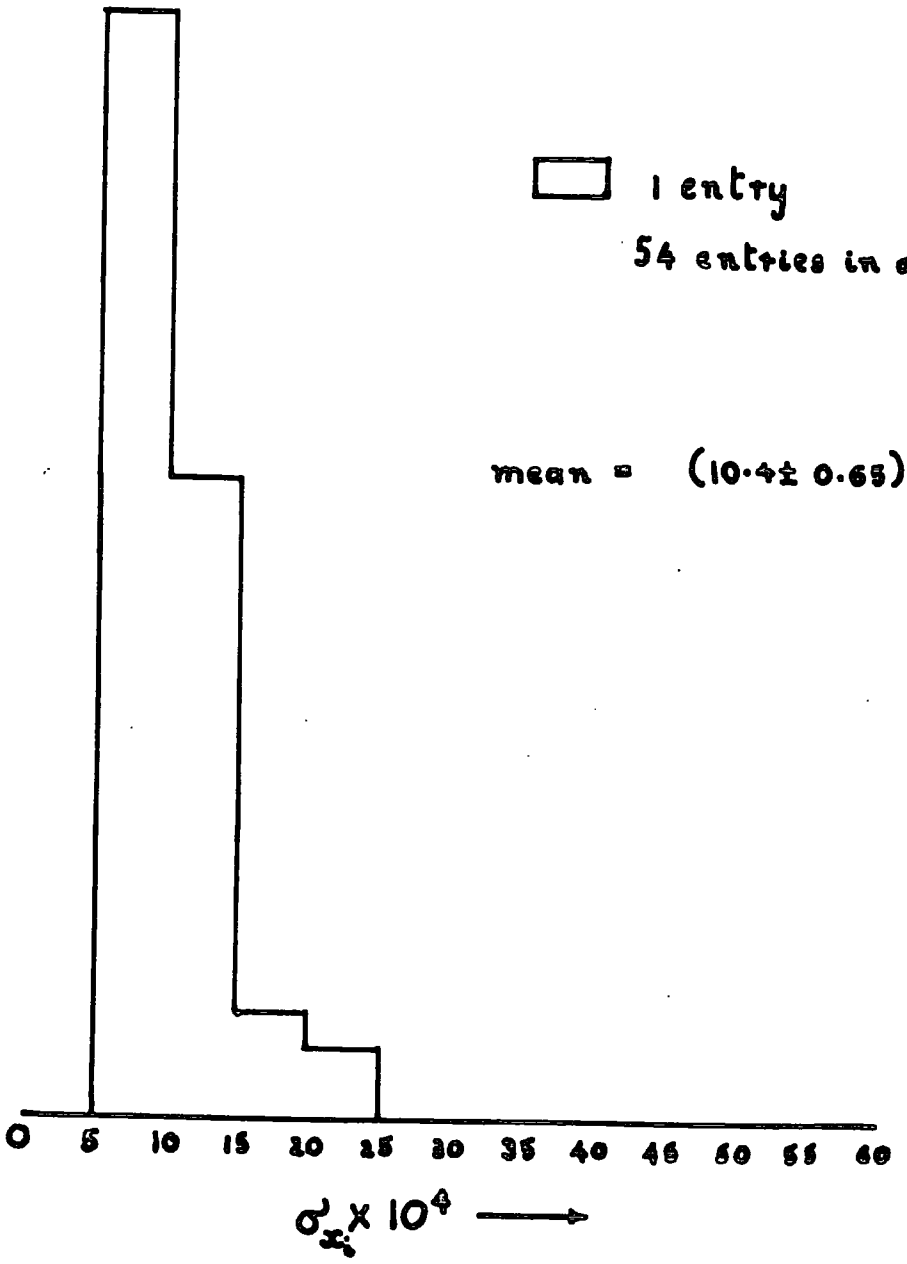

to simulate the measurement errors. The distribution of the adjustments is Gaussian with a full width at half height that may be varied.

The generation of these Gaussian errors is performed by using the properties of a uniform distribution of random numbers within the limits of 0 and 1. As shown by A. Werbrouck (1964) any variable, v say, defined for N such random numbers as

$$v = \sqrt{12.\ N}\left(\sum_{i=1}^{i=N} \frac{n_i}{N} - 1/2 \right)$$

will have a mean value of zero and a standard deviation of unity.

The adjustments were generated by using sets of 12 random numbers so that

$$v = \sum_{i=1}^{12} n_i - 6$$

and subsequently normalised to a given measuring error.

Sets of single numbers specifying the ratio of the lengths between the fiducial crosses were generated for simulated I.E.P. errors of different magnitudes. They were processed in a manner similar to that used in FIDO to determine the mean of each set and the corresponding standard deviation. The distribution of the standard deviation of the X values with the I.E.P. error was parametrized by performing a least squares fit of various polynomials to all the points excluding

the vertex.

The most significant fit was obtained with a second order polynomial:-

$$y = 1.36 + 2.04.x + 0.09.x^2$$

with an error on the interpolated points, σ_y, of $\pm 1.2 \times 10^{-4}$. Solution of the polynomial by substituting for y the mean value of the experimentally determined distribution of σ_x gives a measurement error of 7.0 ± 0.4 μ's. This figure is quite compatible with normal measurement errors and was obtained by rejecting only 4% of the sample as ambiguous measurements. It was therefore concluded that for the film taken with the new field gates less than 4% of the frames exhibited instabilities.

"No-field" Tracks

Errors on the tracks due to chamber turbulence or any other unidentified causes were estimated by measuring beam tracks on the film taken when there was no magnetic field in the chamber. These measurements were performed in view II and in order to reduce the effects of lens distortions only those tracks were used that were within 0.1 cms. of the central axis as defined by the fiducial crosses.

The measurements were performed with a precision microscope and 30 equally spaced points were measured on each track starting from the same position relative to the fiducial marks.

Least squares fits of the parabolic function

$$y = a_0 + a_1 \cdot x + a_2 \cdot x^2$$

were made to the 30 points of each track and to the subsets of 20 points:- the first 20, the middle 20 and the last 20. For the measurements made on one track in each of 95 frames, the distribution of the a_2 coefficients, Fig. 12, shows only a small but significant difference from zero. The mean of this distribution was determined to be $(4.7 \pm 1.2) \times 10^{-5}$ cms. Thus the radius of curvature of the tracks on the film is

$$\rho \simeq 1/2a_2 = 107 \text{ m.}$$

which corresponds to a radius of curvature in the chamber of 1970 m. as the demagnification from the film plane to the centre of the chamber is 18 times.

The corresponding effective magnetic field for 5 GeV/c tracks is 85 ± 21 gauss which is significantly different from the residual magnetic field of 4 ± 2 gauss. This effect was attributed to distortion of the body of the liquid hydrogen during the expansion process.

The distortion, which is equivalent to a maximum detectable momentum of some 800 GeV/c. gives a systematic error of 0.6% in the momentum beam tracks. Its effects were taken into account in the determination of the parameters necessary for the computation of the dynamical quantities of the events.

FIG 12

PLOTS OF a_2 IN LEAST SQUARES FIT OF $y = a_0 + a_1 x + a_2 x^2$ FOR 'NO FIELD' TRACKS

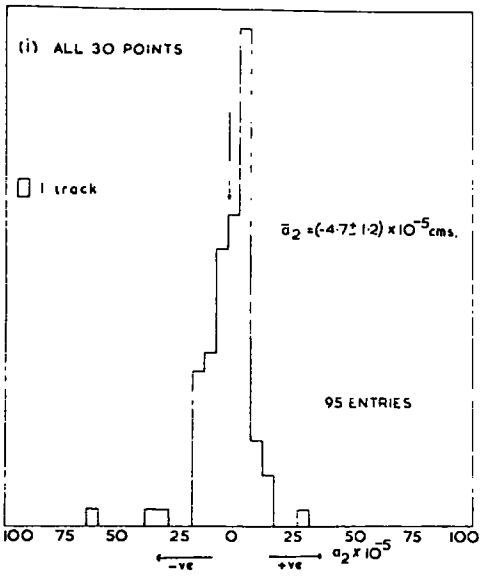

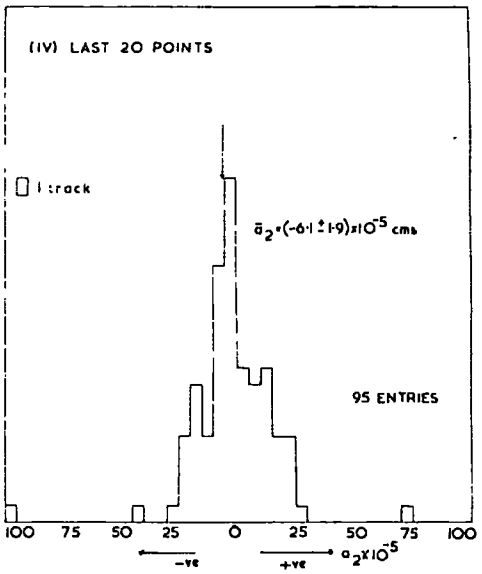

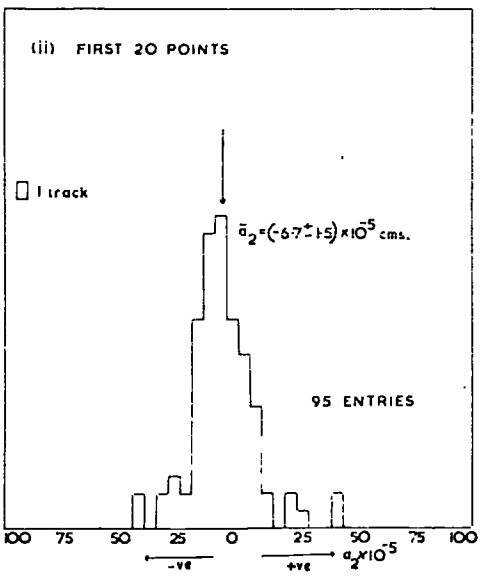

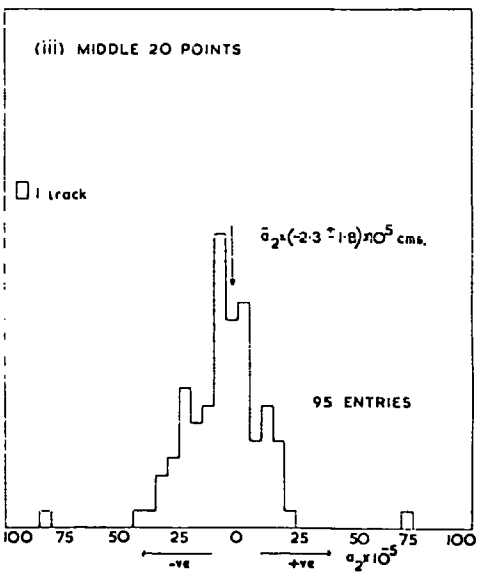

The widths of all the distributions obtained were compatible with the random errors to be expected from measurements and multiple scattering. Furthermore, the mean values of the distributions of the three subsets did not show any significant deviation from the general curvature. Thus it was concluded that no variations of distortion existed within the liquid that could be associated with regions of turbulence.

CHAPTER 3

THE ANALYSIS OF THE EVENTS

3.0 Introduction

In this chapter a description is given of the processes of scanning, labelling, measurement and computation that are necessary to locate and analyse the interactions that have taken place within the bubble-chamber. The class of interactions considered are those with six charged secondary particles; four positive and two negative.

The different stages of the system of analysis are shown in Fig. 13. This system is quite standard throughout all Bubble-chamber Groups and consequently only brief descriptions of each stage are given. Extra emphasis is however placed on those parts which constitute innovations by the group or modifications of the system required by the different conditions pertaining to this experiment.

The film was scanned twice, and each interaction found was fully documented. The measurements were made on the film in accordance with a specific set of instructions, using a I.E.P. constructed in the departmental workshops to the design of the author and his collaborators. The co-ordinate measurements were checked and ordered with the REAP program on the Elliott 803 computer at Durham.

The subsequent computation necessary for each event was

FIG. 13

FLOW DIAGRAM OF THE ANALYSIS OF EVENTS

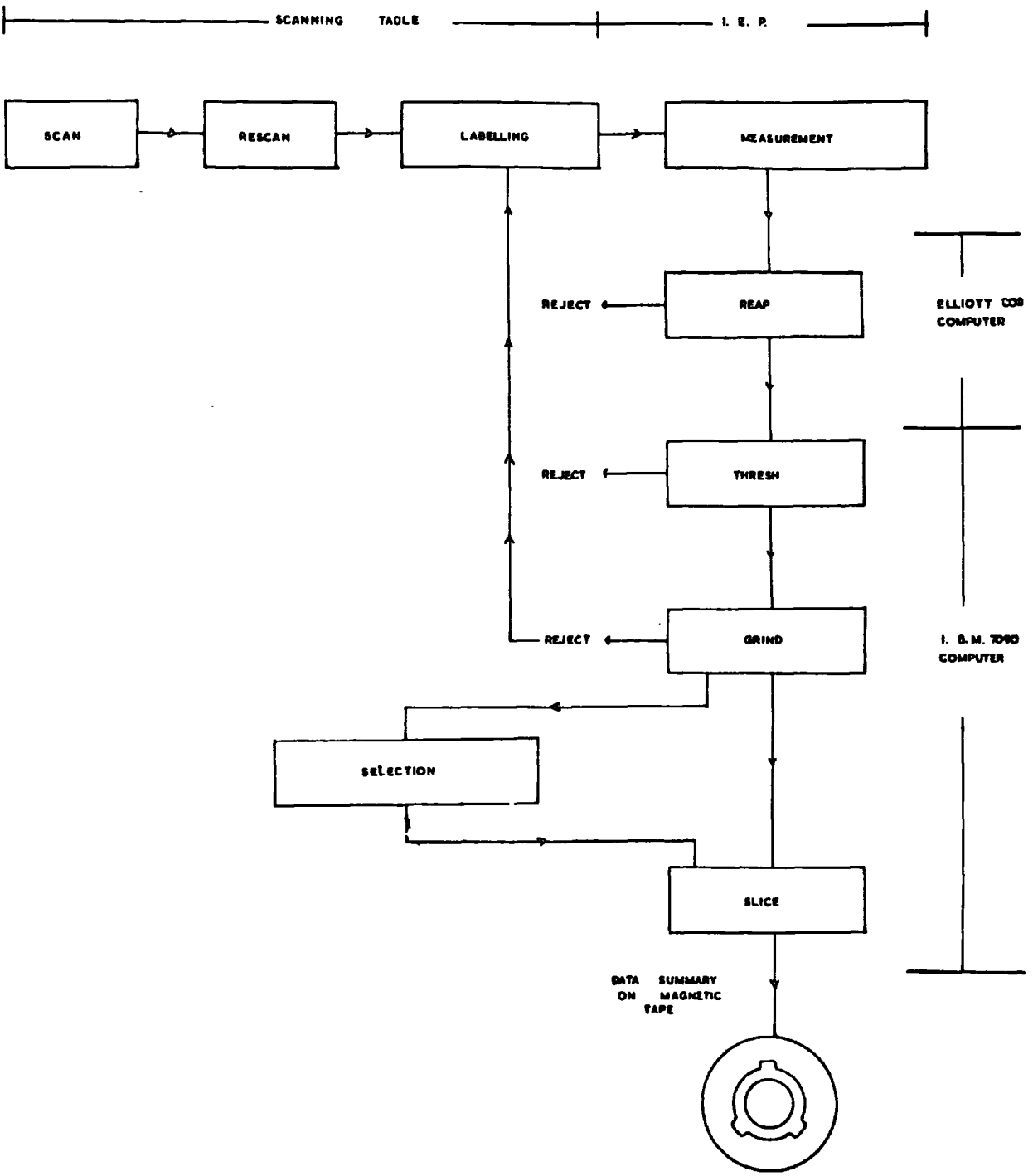

performed with the THRESH-GRIND-SLICE system of programs which required the use of a large, high-speed computer. Reconstruction of the events in 3-dimensional space was performed with the THRESH program and the different possible interpretations of the topology of the events were found by using GRIND. The most probable interpretation of each event was then selected and a full summary of the dynamics for each of the events was prepared with SLICE.

The total cross-section for inelastic interactions of this type was determined using information from the previous stages.

3.1 Scanning

Scanning Tables

The 35 mm. film was scanned on two tables assembled in the departmental workshops. The film transport systems were purchased from Prevost of Milan. The tables were designed to project an image of the chamber on to a horizontal white surface with a magnification of $\simeq$ 14 times. This gave an image about $\frac{3}{4}$ x life-size for the pictures of the B.N.H.B.C.

The image was viewed by observers seated at one end of the table, looking along the direction of the beam tracks. This position was considered the most suitable for the detection of all types of events, especially small angle, elastic interactions.

The surface of the table was big enough to allow the projection of two of the three films at the same time. It was decided that Views I and III should be coincident and View II separate.

The Fiducial Volume

The initial scan was performed by a physicist and a scanner looking for interactions on Views I and II, with View III used for checking. Those events with six charged secondaries were recorded if the vertex of the interaction was within the fiducial volume. This volume was defined on View II with respect to the fiducial crosses in that view. (Fig. 14).

FIG. 14

DIAGRAM OF FIDUCIAL VOLUME

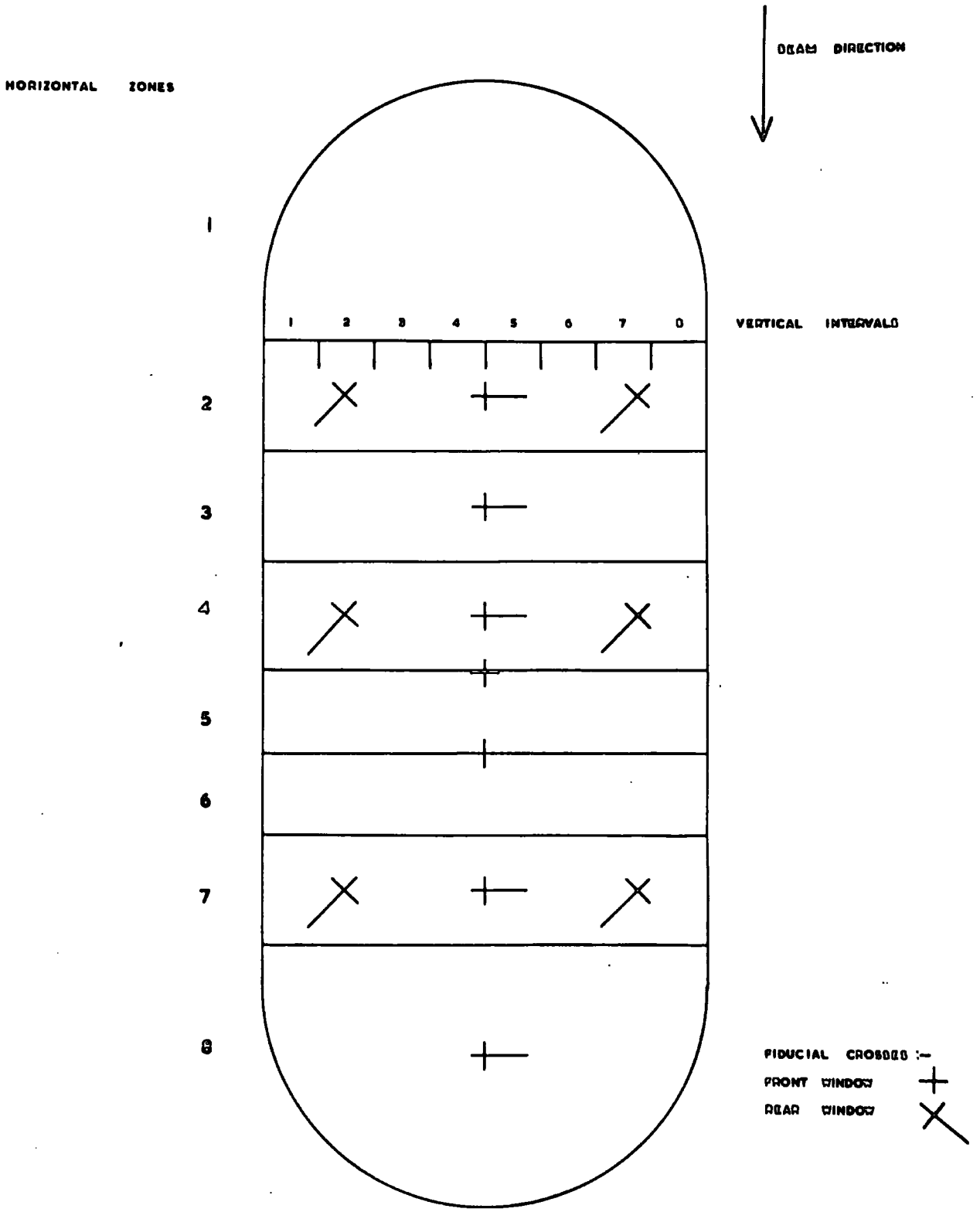

For the six-pronged events the primary track was required to cross in to zone 2 within the vertical intervals 3, 4, 5, and 6 and to have its interaction vertex in the longitudinal zones 2, 3, 4, 5 or 6, and within the bounds of the projection of the vertical intervals along the length of the picture. Although this small fiducial volume contained only ≃ 50% of the useful volume of the chamber, it did ensure that the primary and secondary tracks were of sufficient length to allow accurate determination of their momenta. It was also unnecessary with most tracks to measure as far as the ends of the chamber where the lens distortions were greatest.

A template was constructed with the fiducial crosses, fiducial volume and its sub-divisions, to correspond with the projected image of View II. The position of the vertex was determined by aligning this template with respect to the fiducial crosses.

Characteristics of the Events

Each six-prong found in the fiducial volume was carefully inspected and the following characteristics recorded:-

(i) ... the total number of charged tracks and interaction or decay vertices

(ii) ... charged secondary tracks

(iii) ... identified charged strange particles

(iv) ... V^o particles that connect with the vertex

(v) ... protons identified by inspection of their ionization and curvature

(vi) ... stopping tracks

(vii) ... electron-pairs that connect with the vertex

(viii) ... V^o's that have one track identified as a proton

Additional statistical information on the detection of the event was also retained:

(ix) ... the serial number of the frame

(x) ... the zone within which the interaction occurred

(xi) ... the identification code-numbers of the scanners and the laboratory

Statistics

Of the 25 films available, 1 was taken without the magnetic field and 5 were rejected because of poor picture quality or because they had too many beam tracks. All six-pronged events found in the remaining 19 films were codified according to the so-called GRIND-type classification number which is a five digit number specifying in the following order, the number of

(a) positive, strange secondaries

(b) positive, non-strange secondaries

(c) negative, strange secondaries

(d) negative, non-strange secondaries

(e) neutral, strange secondaries

The events with no identified strange particles, i.e. those with a classification number of 04020, were investigated further.

A total of 704 events of this type were found in the first scan. All the films were scanned a second time by two scanners. The additional 37 events found in this scan were added to the sample to give a total of 741 events. From a knowledge of the number of events found in the second scan and not the first, and the number found in the first but not the second, 24, the efficiency of detection of the events with the two scans was determined to be 99.8 $\pm$ 1%. It was assumed that the probability of observing all types of 6 pronged events remained constant, which is quite reasonable for these highly visible events.

3.2 Labelling

With the large number of secondary tracks in six-prong events there is a high probability of changes in the cyclic order of tracks in different views. To reduce the time wasted by the measurer trying to identify corresponding tracks in the different views, this work was done on the scanning table by a physicist who consulted all views simultaneously.

Sheets were prepared for each event that specified by a fixed format title, "library information" on the experiment number, frame number and GRIND-type classification for the event. Appropriate spaces were left for the measurers to insert their own identification code-number and the number of the machine. These sheets also contained lists of the labels of the points and tracks to be used by the checking program REAP starting with the primary. The order of the labels in the lists was the correct sequence for anti-clockwise, track-by-track measurement in each view.

The opportunity was taken to use "special labels" to specify the nature of any identified tracks. These restrict the number of hypotheses used by GRIND and mistakes in their usage could cause failures in that part of the analyses. Moreover, incorrect interpretations of the sequence of the tracks in any view can cause failures in THRESH. Therefore, with the events

that had to be remeasured, the relabelling was done without recourse to the first measurement sheets and this time no special labels were used.

3.3 Measurement

General

All the six-pronged events were measured on the Durham I.E.P. 1. This instrument which was designed for two dimensional co-ordinate measurements on the film plane of either 35 and 50 m.m. unperforated film. In contrast with many other measuring machines that have their moving stages mounted one on top of the other, this design has its two substages, X and Y, mounted on the top and bottom of the fixed surface, A, as illustrated in Fig. 15. The X-substage carries the films and the Y-substage supports the optical system. Apparent movement of the film was obtained by moving the film in the X direction and the optical system in the Y direction.

This arrangement allowed the overall size of the machine to be reduced and consequently it was possible to use commercially available components, which lowered the cost appreciably. It also has the additional advantage that the heavy driving motors, the film transport system and the film spools may be mounted on the rigid structure supporting the central section. Provision was made to keep constant the length of unwound film between the stationary film spools and the part of the film clamped on the moving X-substage.

The movements of the X and Y substages were digitized with two Moiré fringe systems and the facility provided for punching

FIG. 15

SCHEMATIC DIAGRAM OF I.E.P. 1.

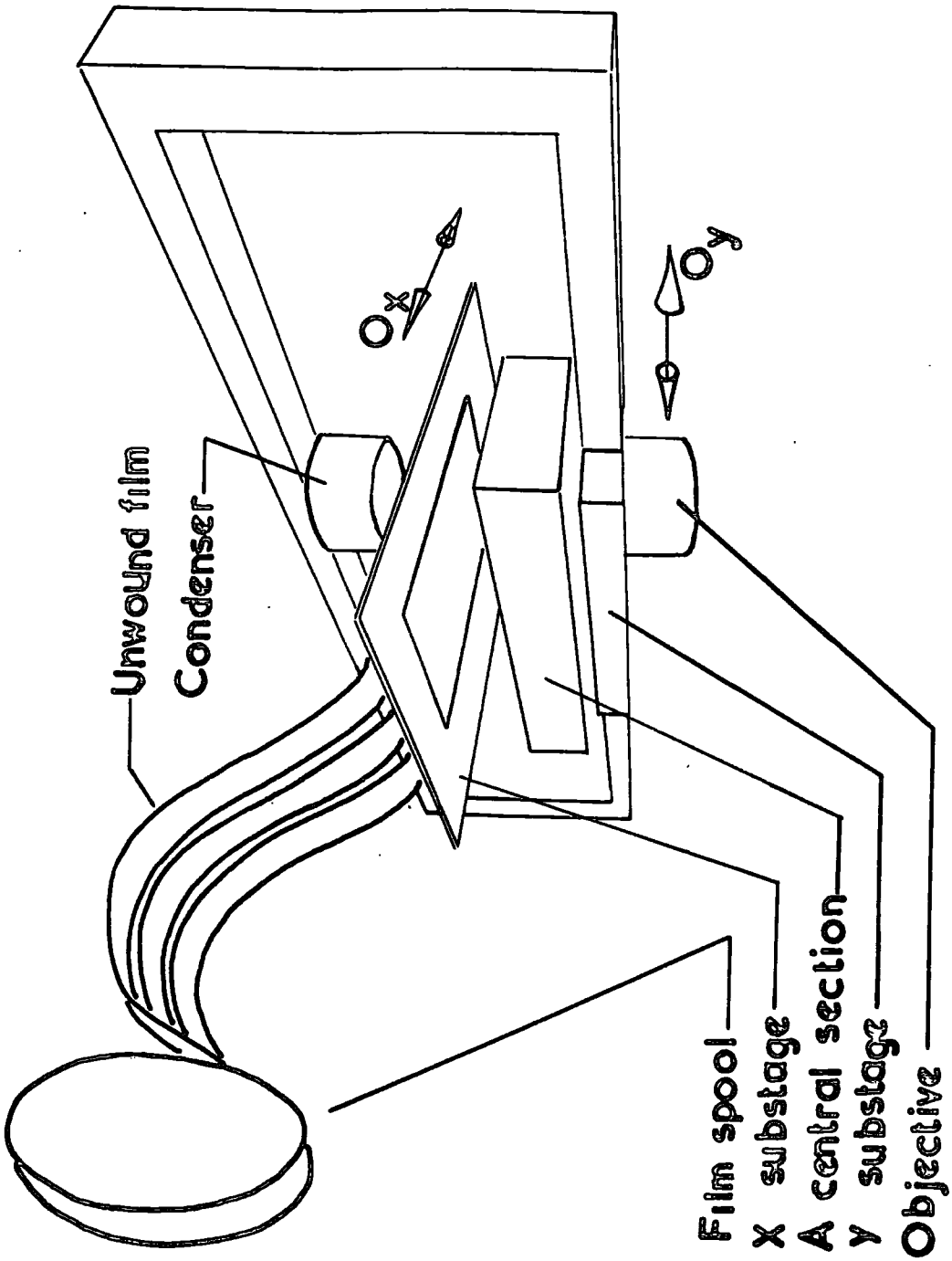

out co-ordinate measurements on to 5-hole paper tape.

The Moving Stages

The central section and the Y-substage of the machine comprised a Schneeberger linear reciprocating table with a stroke of 160 mms. This was suitably converted to accommodate the convergent light cone of the projection system. The objective lens (Schneider Componon) was fitted on to the Y-substage with an adjustable mounting.

On top of the table, mounted perpendicularly to the other direction of motion are two Schneeberger linear bearings. The conjugate slides to these are mounted on the X-substage - a machined aluminium plate. All the bearing surfaces were accurately aligned to have the correct relative attitudes, bolted down, and fixed permanently in these positions with "Araldite".

Each direction of motion has one coarse and one fine control motor. The fine control motors have tachometer generators which supply a feedback system to obtain smoother operation.

The 50 c.p.s. coarse control motors have dural pulleys mounted on to the output pinions of their 500:1 reduction gearheads. These pulleys are coupled to similar pulleys mounted on to idler spindles by a thin phosphor-bronze tape, which is tension loaded to remove backlash.

The fine control is provided by 400 c.p.s. servomotors which are size 11 with 1,000:1 reduction gearheads. They drive small precision leadscrews through a fine flexible coupling. The fine motors and the leadscrews are mounted on the X and Y substages. The cursors of these leadscrews are rigidly clamped to the phosphor-bronze tape.

The motors are controlled by a joystick which has two axes of rotation. The two rotating shafts of the joystick are coupled to the armatures of two precision potentiometers which supply the input signal to the servomotor amplifiers. The change-over from coarse to fine operation or vice-versa is effected by switching these potentiometers from one circuit to the other.

A complete limit system is provided for each direction of motion. When a limit has been exceeded the motors are automatically switched off and the condition is indicated on the appropriate lamp in an array surrounding the joystick.

The Film Transport System

The three films are held firmly in position on a $\frac{1}{4}$" glass plate set into the X-substage, by a spring loaded clamping device. They are pressed flat by three smaller glass plates and clamped by three rubber tipped plungers placed beyond the ends of these plates. The clamping device is lifted by powerful solenoids to allow movement of the films.

The unwound film between the spools and the film clamp is threaded through a system of rollers. Each roller consists of three independent pulleys mounted on a common shaft. This allows any one of the three films to be moved without disturbing the others.

There are three sets of rollers on either side of the X-substage. One is mounted on the moving stage and another on the structure supporting the central section. The middle rollers are supported by a system of spring-loaded pylons which ensures that the length of film threaded through the rollers is constant whatever the position of the stage.

The film spools are driven by a single a.c. reversible motor. This is coupled to the splined shafts supporting the spools through electrical clutches and mechanical slip-clutches. An electrical brake is provided for each splined shaft. The control circuit for the electrical components is designed to actuate the solenoids of the film-clamp and move any one or all three of the films at a time.

Digitization

The movements of the stages in the two orthogonal directions of motion are digitized with a Moiré fringe system. For each direction of motion there are two linear diffraction gratings of 8 μm pitch, one as long as the traverse of the stage and the other a small circular index grating: their surfaces being separated by only 75 μm. They are illuminated by a condenser

FIG. 16

BLOCK DIAGRAM OF DIGITIZATION

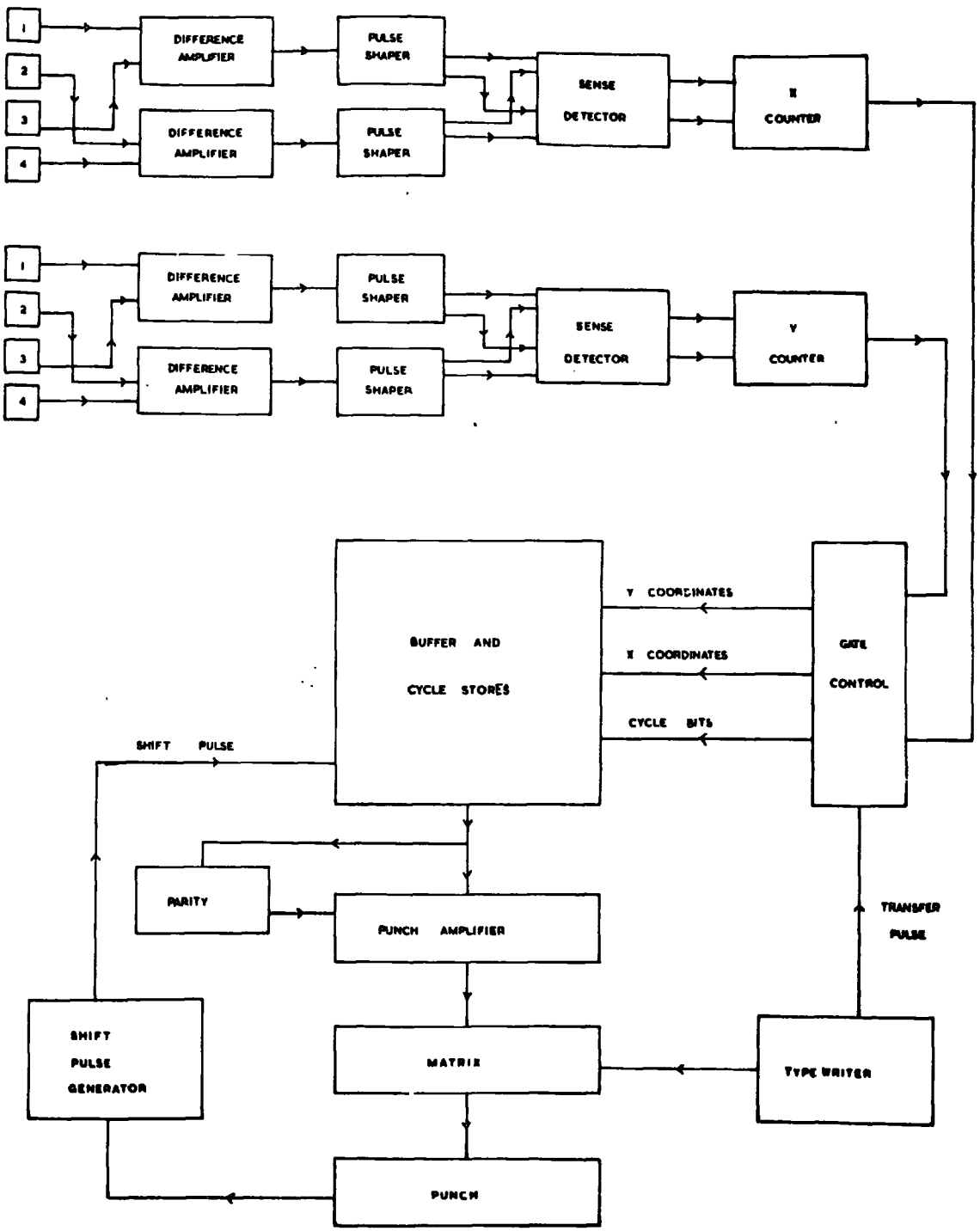

and the fringe pattern produced is subdivided by a special 'Ferranti four-splitter lens', which projects four different parts of the fringe on to four photocells. The separation and the relative attitude of the two gratings are adjustable so that the photocells give signals of nearly equal intensity that are in quadrature.

The output signals of the photocells are taken in pairs that are in anti-phase and supply two difference amplifiers. The outputs of the difference amplifiers are shaped to give two square waves 90° out of phase and their anti-phase waves regenerated. These four signals supply a sense-detector which is coupled to a bi-directional binary counter. Depending upon the direction of motion of the stage, numbers are added to or subtracted from the contents of the 17-bit binary registers of the counters. For each fringe the counter receives four pulses, giving a measurement accuracy of two microns.

The contents of the two binary registers are transferred on to paper tape in a format that can be decoded by a sub-routine of REAP. The co-ordinates are transferred by a parallel read system in to a buffer store consisting of shift registers interconnected to give 6 words of a fixed length of 6 bits. Extra "1's" are added in to the corresponding locations of the cycle store.

FIG. 17

SCHEMATIC DIAGRAM OF CO-ORDINATE PUNCHING

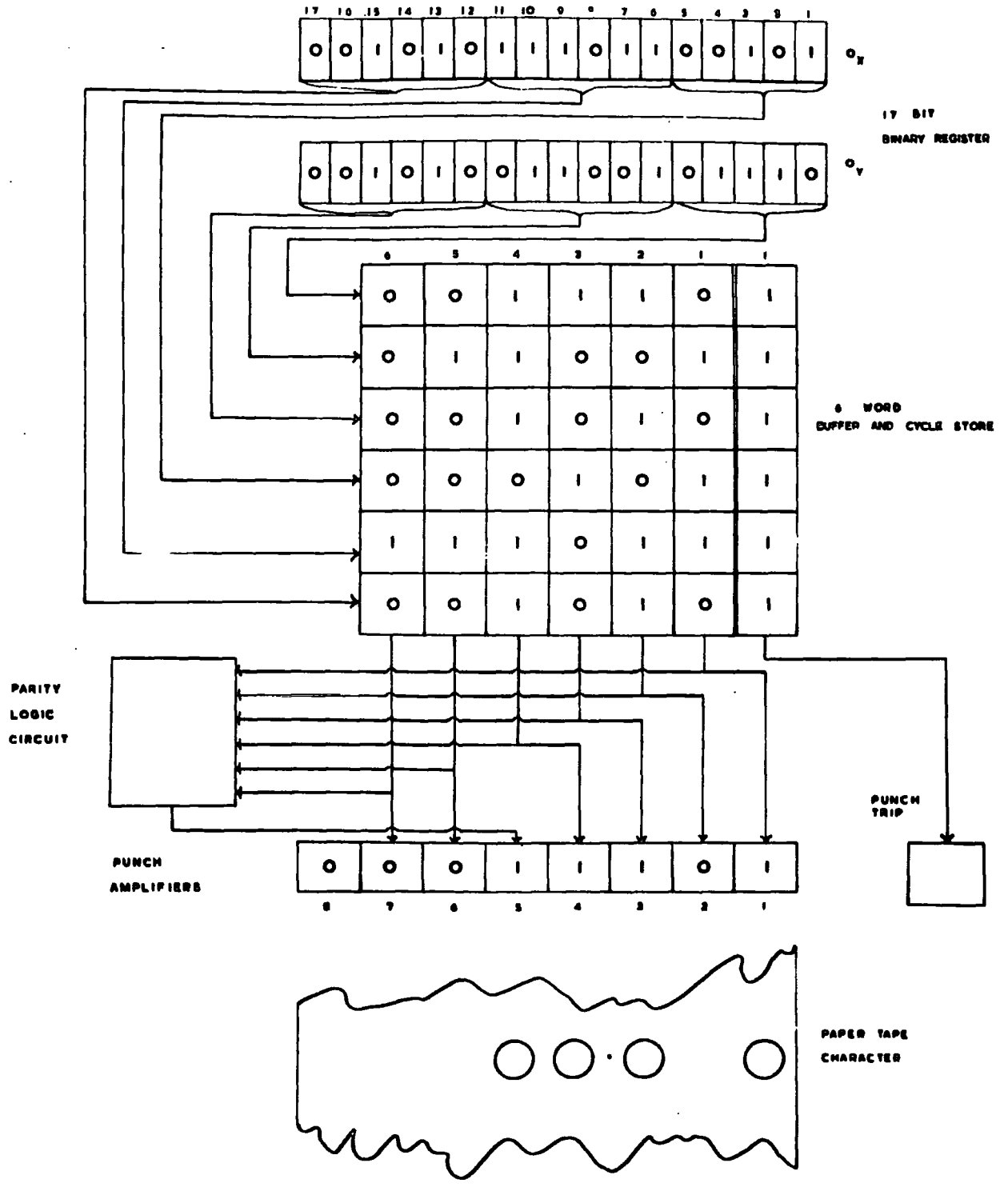

The first location of the cycle store is scanned for non-zero contents. A positive condition causes the contents of the first location of the buffer store to be punched together with an extra digit supplied by an even parity logic circuit.

The punch provides a shift pulse at the end of its punching operation which causes the numbers in both stores to be advanced by one location and clears the last one. This cycle is repeated until a zero number reaches the first location of the cycle store.

The punching out sequence is initiated by a signal from the typewriter which prints the character "->" on the measurement sheet to indicate that a pair of co-ordinates have been punched. It is always preceeded by the character "/" which calls the decoding subroutine in REAP.

Optical System

The film is projected on to a flat screen comprised of a sheet of 'ethulon' compressed between two pieces of plate-glass. This material has a very fine grain and produces a high quality picture. Co-ordinate measurements on the film are performed with respect to co-incidences of the appropriate part of the image and a reference point consisting of a small "dot" set in the middle of the screen. The dot is of the same order of size as the projected image of a bubble of a

minimum ionizing track.

The magnification of the optical system is 15.1 times. The light falls on to a mirror underneath the table which reflects it on to the screen. Movements of the top stage in the O_x direction give a nominally direct measure of distance in this direction but all values in the O_y direction are subject to a constant demagnification because the optical system moves. Further constant demagnifications in the readings for both directions of motion may be introduced by an incorrect attitude of the axes of the mirror. All such constant demagnifications are dealt with in the geometry program THRESH.

Operation

The operator measured the events in accordance with the instructions given on the labelling sheet. In each view the binary registers were reset at 2^{16} when some easily recognisable part of the picture, e.g. the vertex or a fiducial mark, was set on the reference point. Four fiducial points, the interaction vertex and six or seven points per track were measured. As the version of THRESH used in the reconstruction made no allowance for energy loss, care was taken to bias the measured points towards the vertex for those tracks with an appreciable curvature.

FIG. 18

SCHEMATIC DIAGRAM PROJECTION SYSTEM

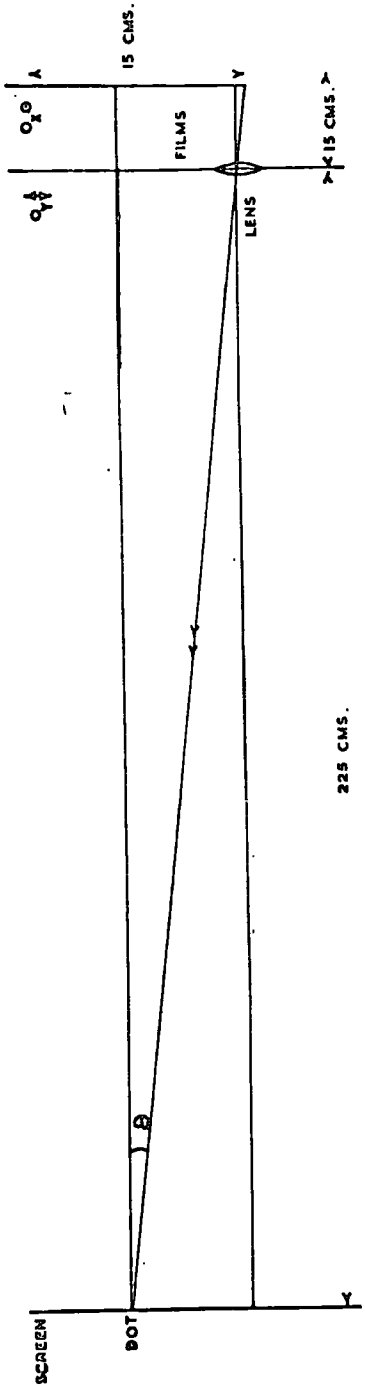

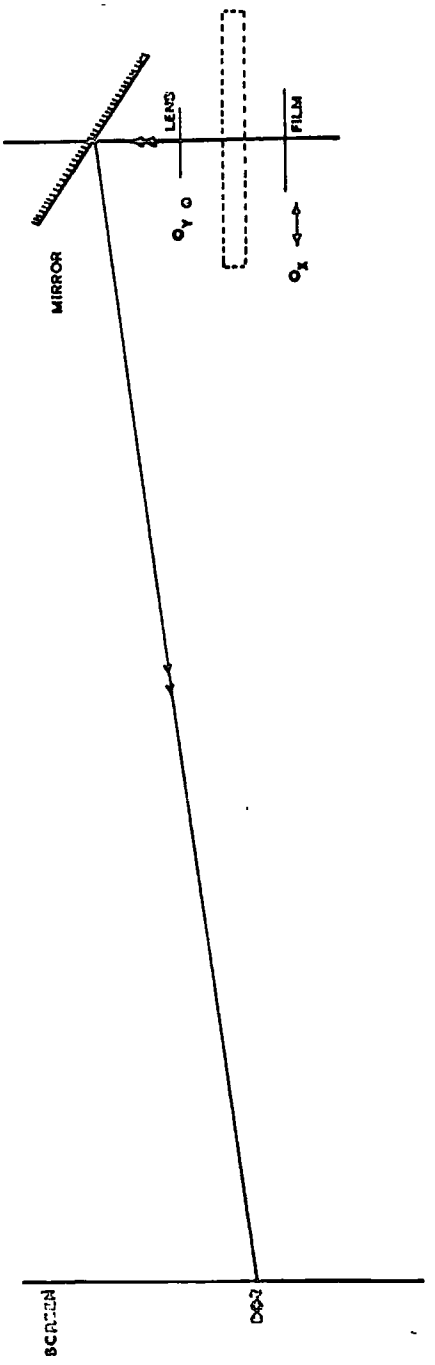

A visual display of the contents of the two binary registers is provided on the front of the console of the machine so that the operator could chec' that no deviation had occurred with respect to the original setting. These checks were usually carried out both during and after completion of the measurements in a view. If some shift was found on realignment with the zero position the counters were reset and the whole view or part of it was remeasured.

With constant development the performance and reliability of the machine has improved progressively over the period of about one year that it has been in operation. In this time some 5,000 events have been measured with a rate of measurement of between 3 to 5 events per hour, depending on the topology of the events.

3.4 REAP

General

The measurements of the six-pronged events were checked and rearranged in the special format required by the next program THRESH. This was done with the REAP program written for the Elliott 803 computer by H. Halliwell. The program processes the data-tapes from the I.E.P.s and gives two output tapes; one is a summary of the checking and the other is the event data in the new format.

The summary contains the title of the event and the results of the checks on the fiducial and track measurements made in each of the three views.

Tests

Specific ratios of the squares of the lengths between the fiducial crosses were evaluated in a manner similar to that used in FIDO (c.f. Section 2.4). For each view these numbers are constant to within 0.2% and are a good, quick test that the right fiducial crosses have been measured.

The number of points measured on each track was checked and if this number was less than three the track was considered to be unmeasured and correspondingly designated with an "0".

Two methods were employed to test the measurements made on the tracks. If the track failed the first simple test

then it was examined with a more accurate one.

The first test consisted of a check on the constancy of curvature of different sections of the measured track. The simple algebraic conditions involved which are derived in Appendix I, allowed a more efficient use of the limited computer time available.

If the conditions imposed by this test on the measured points failed at any time the computation was immediately transferred to the second test. This was a least squares fit of the parabolic function

$$y = ax^2 + bx + c$$

in an orthogonal system with the x-axis along the line joining the first and last points of the track. The fitted values of y, viz. y_i' were then compared with the measured values, y_i, in the condition

$$40 \geq (y_i' - y_i) \qquad \ldots . (1)$$

$$i = 1, \ldots, n$$

If the measurements of the track fulfilled either of the two conditions then it was designated with an asterisk "*" if neither it was designated with a question mark "?".

Any wrongly measured fiducial cross or an unmeasured track were considered sufficient cause for remeasurement. Error conditions on the fitting of the tracks were interpreted more liberally as they were often indicative of such tracks as stopping pions.

3.5 THRESH

General

THRESH is the mass-independent geometry program of the T.C. program library of C.E.R.N. Its function is to reconstruct the tracks and points of the interaction in the co-ordinate system of the chamber using the two-dimensional measurements made on three films. In doing this, it assumes that the magnetic field is uniform and consequently the tracks may be described by helices.

Distortions

The FORTRAN II version of THRESH was used on the I.B.M. 7090 computer at Bonn University. This program contained the necessary modifications, viz. subroutine CORREC, to allow for the distortions known to exist in the cameras of the B.N.H.B.C. The system used was devised by G. Kellner (1965) who fitted the distortions with a general polynomial of the form

$$\begin{pmatrix} x' \\ y' \end{pmatrix} = \begin{pmatrix} x \\ y \end{pmatrix} \quad (1 + a_1 x/f + a_2 y/f + a_3 (xy)/f^2 + a_4 x^2/f^2 + a_5 y^2/f^2 + a_6 (x^2 + y^2)^2/f^4)$$

where x', y' represent co-ordinate values on the "ideal film plane" that would have been expected if the lens acted like a simple pin-hole camera. The variables x, y are the co-ordinates on the "physical film plane" - the actual image

on the film when the effect of film shrinkage has been removed.

The polynomial contains terms to account for the distortions caused by the following:-

(i) tilt of the film plane .... $a_1 x/f + a_2 y/f$

(ii) spherical lens distortion .... $a_4 x^2/f^2 + a_5 y^2/f^2$ and $a_6(x^2 + y^2)^2/f^4$

(iii) other non-identified causes ... $a_3(xy)/f^2$

Program

The values of the "reference fiducial marks" which are located on the back of the front glass (c.f. Fig. 19) and the fitted values of the coefficients of the polynomial for each camera determined by Kellner and checked by members of the collaboration were used in THRESH. The positions of the reference fiducial marks are necessary in order to perform the linear transformation

$$X_i = \alpha_1 + \alpha_2 x_i + \alpha_3 y_i$$
$$Y_i = \alpha_4 + \alpha_5 x_i + \alpha_6 y_i$$

which transforms the coordinate measurements into the physical film plane system. This transformation removes possible effects of film shrinkage, changes in magnifications and non-orthonormality of the F.I.F. axes (c.f. Section 3.3).

The distortions are removed by using the polynomial transformation which transforms from the "physical film plane"

FIG. 19

SCHEMATIC DIAGRAM OF CHAMBER OPTICS

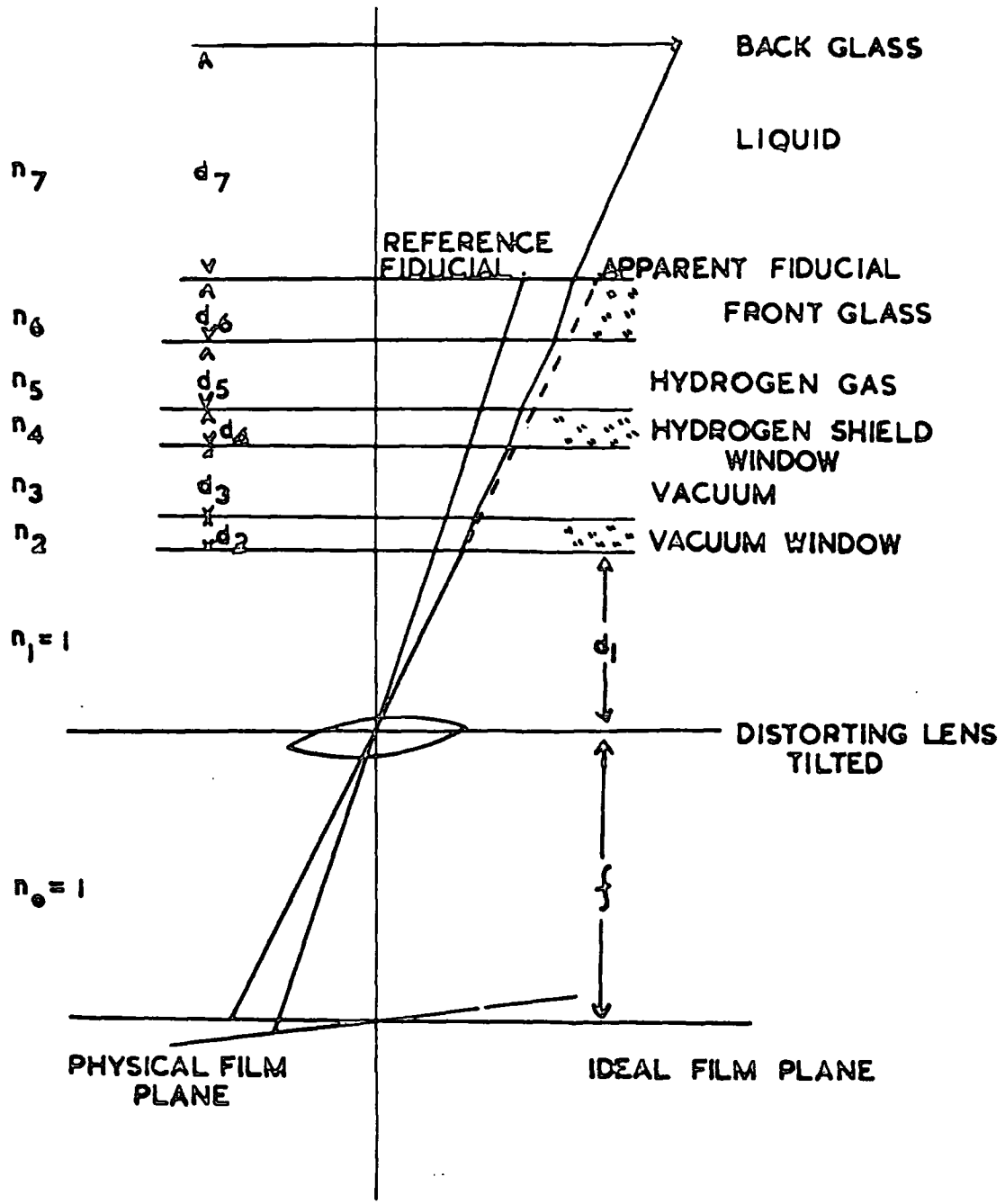

into the "ideal film plane". The "reconstruction tapes" are obtained from the exact positions of the crosses and the known data on the geometry of the chamber and the refractive indices of all intervening media. As has already been pointed out it is assumed that the lenses act like pin-hole cameras with the hole at the front nodal point of the objective.

The subsequent calculations in THRESH were the standard procedures of reconstruction of the tracks by the method of "corresponding points" and the χ^2 fitting of helices to these tracks. The binary output tape contained the required data in the correct format for GRIND.

Event Rejection

An additional output summary of each event was generated which contained data on the vertex co-ordinates, curvature of the tracks and errors of the fitting process. This summary was used to choose which events needed remeasuring.

Events were rejected if any of the tracks had not been reconstructed or the process of fitting a helix to a track did not converge.

3.6 GRIND

General

The GRIND program of the T.C. library was used to test the dynamics of the various hypotheses applicable for the six-pronged events. The Fortran II version was used at Bonn with the data for each event provided on the output tape of HYDRA.

The parameters of the program are given by a set of titles which are used for each event. These titles specify information on the system of analysis and the experimental variables.

GRIND Titles

The "range-momentum" relations for the tracks that stop within the chamber are given in a mass-independent form and are a function of the chamber liquid only.

The magnetic field and its spatial variation within the chamber are specified. The average value of the magnetic field was determined by M. Blum as 13.54 $\pm$ 0.01 K.gauss. It was subsequently modified by members of the collaboration who obtained a value of 13.46 $\pm$ 0.04 K.gauss by fitting K^0 and Λ^0 decays in GRIND using the magnetic field as a variable parameter. The lower magnetic field value was preferred as it constituted a direct measurement made under the appropriate

operating conditions.

The topologies available for each GRIND-type classification were also included. For the six-pronged events, with a classification number of 04020, these are given in Table 1 below:

Table 1

Topologies available for events of GRIND type 04020

No. of constraints	Topology	Hypothesis no.
4	$\pi^+\pi^+\pi^+ p \; \pi^-\pi^-$	1
	$\pi^+\pi^+ p \; \pi^+\pi^-\pi^-$	2
	$\pi^+ p \; \pi^+\pi^+\pi^-\pi^-$	3
	$p \; \pi^+\pi^+\pi^+\pi^-\pi^-$	4
1	$\pi^+\pi^+\pi^+\pi^- p \; \pi^-\pi^-\pi^0$	21
	$\pi^+\pi^+ p \; \pi^+\pi^-\pi^-\pi^0$	22
	$\pi^+ p \; \pi^+\pi^+\pi^-\pi^-\pi^0$	23
	$p \; \pi^+\pi^+\pi^+\pi^-\pi^-\pi^0$	24
1	$\pi^+\pi^+\pi^+\pi^+\pi^-\pi^- n$	25

It was necessary also to specify the identification labels used in measurement (c.f. 3.2 Labelling) and the energies and masses of the beam and target particles and the magnitudes of

the track errors expected within the chamber. Because the fractional error due to liquid distortion is smaller for the tracks of lower momentum, the beam momentum was evaluated from the distribution of the fitted momentum of a pure sample of 4c events. The mean of this distribution was 4.996 ± 0.006 GeV/c.

The sources of random error considered were those arising from measurement, multiple scattering and turbulence of the chamber liquid. The measurement error was set at 75 μm; about 1/5 of the diameter of a bubble within the chamber. The multiple scattering constant was derived according to the formula quoted by R. Bradner (1960), using a value of 0.0605 gm/cm^3 for the density of liquid hydrogen at 27°K and 70 p.s.i. The random error due to liquid turbulence was neglected on the evidence of the measurements of the "no-field" tracks.

Program

The classification of the events is performed in the program using the labelling scheme given in the titles. Tests are made on the quality of the measurements on each track by comparing the internal errors calculated by the program with the external ones derived from the specified error estimates.

The magnetic field matrix is used to convert the curvatures

of the tracks in to momenta which are then corrected to the vertex. The values obtained are used as the initial values in the iterative fitting procedure to obtain a least squares fit to the four constraint equations of energy and momentum. Such fits are attempted for all the topologies specified for that particular GRIND-type classification.

Three types of output were generated by GRIND:-

(i) ... the summary of the event with information on those hypotheses that were fitted.

(ii) ... the "GRIND data banks" which contain a complete list of all the dynamic quantities of the unfitted event and the fitted hypotheses.

(iii) ... the "SLICE cards" which are used in the next program to select required quantities from the GRIND data banks.

3.7 Classification of the Events

Results of the analysis

The numbers of events passing each stage of the system of analysis are given below in Table 2.

Table 2

Data on the analysis of events

Scan and Rescan	Measure 1	GRIND 1	Measure 2	GRIND 2	Total
741	696	459	187	131	590

Initially, 45 of the total of 741 events were not measured because of the poor visibility of the event or the nature of their secondary tracks. During remeasurement, an additional 50 events were discarded as they had a low probability of being reconstructed. In all, some 80% of the 741 events were reconstructed satisfactorily.

Hypothesis selection

The 'GOOD FIT' hypotheses were selected from the 590 reconstructed events. A hypothesis was accepted as a possible interpretation of that event under the following conditions on the χ^2 of the fit, the missing mass squared, MM^2, and the error on the missing mass squared $\Delta(MM^2)$:

As fit $\chi^2 \leq 24.5$ and $MM^2 - 2\Delta(MM^2) \leq 0.0 \leq MM^2 + 2\Delta(MM^2)$

1c(π^0) fit $\chi^2 \leq 6.0$ and $MM^2 - 2\Delta(MM^2) \leq 0.02 \leq M^2 + 2\Delta(MM^2)$

1c(n) fit $\chi^2 \leq 6.0$ and $MM^2 - 2\Delta(MM^2) \leq 0.9 \leq M^2 + 2\Delta(MM^2)$

These criteria were chosen to correspond with those found to be useful in the analysis of six-pronged events in π^+p interactions at 4 GeV/c (ABBHM collaboration 1966). They are based upon a probability of < 0.1% of 'NO-FIT' events being interpreted as fitted events in the respective channels.

The bubble densities of the tracks as seen on the scanning table were compared with the expected bubble densities for the tracks as given on the summary of GRIND in a form which is corrected for the dip of the track on the central view. It was found possible to identify protons of energies up to about 1.5 GeV/c so that in many cases it was possible to eliminate some of the incorrect hypotheses. However, if there remained 'GOOD-FITS' to both the 4c and 1c hypotheses then the 4c hypothesis was preferred.

If no such selection by ionization was possible then the 4c hypothesis with the lowest χ^2 was taken. In the cases where there were no 4c fits then the 1c fit with the lowest χ^2 was chosen.

The events that could not be assigned to any of the above categories were classified as 'NO-FIT' events.

Statistics

The distributions of χ^2 and MM^2 for events accepted in each of the different channels are shown in Figs. 20 and 21. For the 4c events the distribution of the unfitted MM^2 shows a small but significant shift of 0.0025 GeV^2 from zero. This deviation was attributed to the systematic error due to liquid distortion which tends to reduce the curvature of positive tracks. As a consequence of this the initial values of momentum for the χ^2 fitting procedure of GRIND were subject to a systematic error and the corresponding χ^2 distribution for the fitted events was biased to the higher values because of this underestimate in the error. This effect required a more liberal interpretation of the χ^2 condition for fits in this channel and careful reexamination was necessary to ensure that no true 4c events had been misclassified.

For events with an extra neutral particle e.g. the $1c(\pi^o)$ and $1c(n)$ channels, the average momenta of the secondaries was less with a corresponding reduction in the fractional error on the curvature due to this systematic effect. If was found that the mean values of the MM^2 distributions were not significantly shifted from the π^o and neutron masses.

The numbers of the events within the different channels is given below:

Fig. 20

Histograms of X^2 for Different Channels (Durham Data)

(a) 4c events

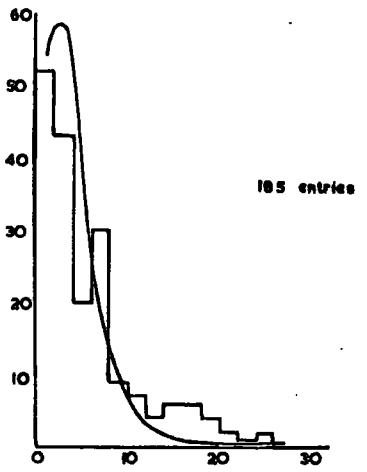

(b) 1c (π^0) events

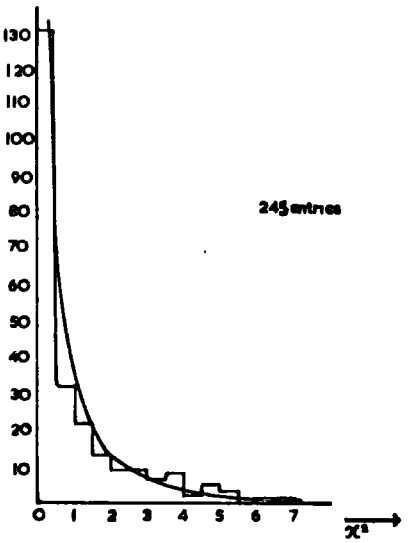

(c) 1c (η) events

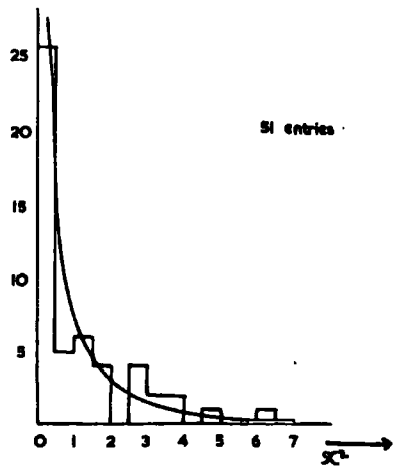

Fig. 21

Histograms of Missing Mass Squared for Different Channels.

(Durham Data)

(a) 4c Events.

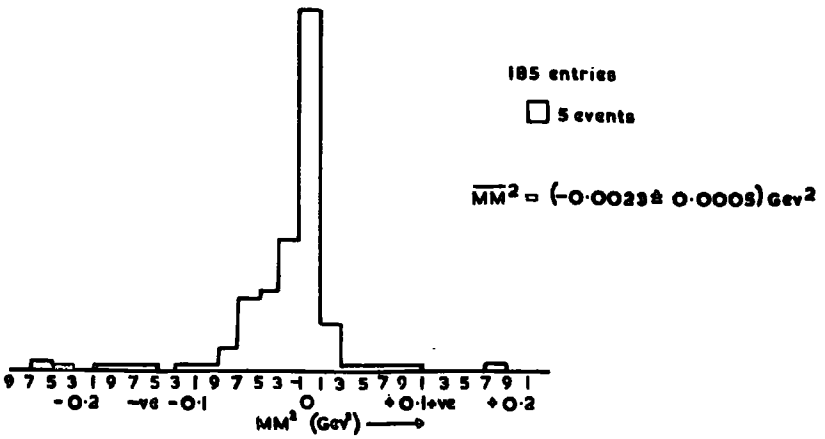

(b) 1c(π^0) Events.

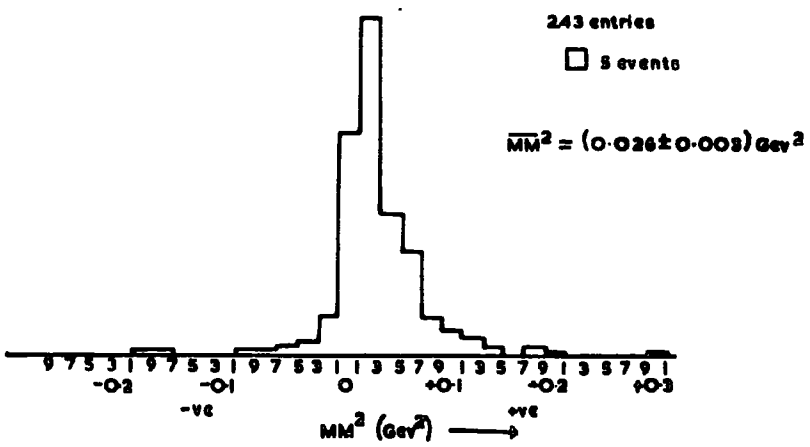

(c) 1c(n) Events.

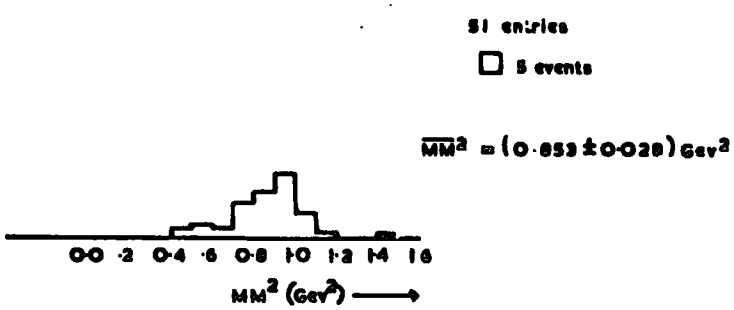

Table 3

Distribution of events within channels

4c	1c(π^0)	1c(n)	NO-FIT
185	243	51	111

Cross-sections

An estimate of the total cross-section, σ_T, was made for six-pronged events using the Durham data only as given in Table 3. The cross-section per event, σ_e, with respect to the fiducial volume was computed from a knowledge of the distribution of beam tracks per frame, the total number of frames scanned and the geometry of the fiducial volume. Corrections were made for the estimated muon contamination, the dip and curvature of the beam tracks and for particle interactions. The cross-section per event was determined to be

$$\sigma_e = 1.86 \pm 0.02 \ \mu b.$$

giving a total cross-section for the corrected total of 743 six-pronged events of

$$\sigma_T = 1.38 \pm 0.06 \ mb$$

No correction for scanning loss was made because of the high efficiency for detecting events of this high multiplicity. (c.f. section 3.1).

The Data Summary

Complete summaries of the dynamical quantities of the selected hypotheses were prepared for the four different channels. As a consequence of the lower statistics for these high multiplicity events the summaries could be made extremely comprehensive and contained over 2,000 items of information for each event. Information on the fitting process was retained together with data on the geometry, energies and momenta of the individual particles and all the possible particle combinations, both in the laboratory and centre of mass systems.

The summaries were prepared with the SLICE computer program of the T.C. library. The program, acting on the information furnished by the appropriate SLICE card for the selected hypothesis, read the relevant quantities for that magnetic tape containing the GRIND data banks. These quantities were processed to give the appropriate data summary which was written on to another magnetic tape, the "Data Summary Tape" (D.S.T.).

CHAPTER 4

THE ANALYSIS OF THE RESULTS

4.0 Introduction

In this chapter the methods used to analyse the results are described and information is presented on the physical effects deduced for the interactions in the two most populous channels of the six-pronged events; the 4c channel and the $1c(\pi^0)$ channel. This work was undertaken with the combined sample of data from the five collaborating laboratories using the statistical analysis program SUMX of the T.C. program library. The experimental distributions obtained were compared with the theoretical phase space curves calculated with the Monte-Carlo program FOWL. The many deviations between these two distributions were investigated further in order to determine the underlying physical phenomena present in these types of interaction.

Data Consistency

Before the analysis of the combined data could proceed it was necessary to undertake preliminary tests to ensure compatability between the different subsets presented by the individual groups. In preference to the widespread custom of all groups analysing the same small sample of film in order

to examine the biases due to differing techniques of analysis, it was decided to investigate the effect of any possible biases on physical phenomena.

The distribution of events within the four channels was compared with that of the total sample and no significant deviation was found for any subset. Nor were there found any differences between the different momentum distributions of the individual particles. Furthermore, the position and width of the peak in the $\pi^+\pi^-\pi^o$ effective mass spectrum due to the ω^o resonance which is strongly produced in the $1c(\pi^o)$ channel was investigated. The contribution and position of this peak as seen in the various subsets were compared with that of the combined sample. All the sets of data were found to be consistent.

Statistics

The disposition of the total sample of 3467 reconstructed six-pronged events within the four channels was

4c	$\pi^+ p$	$\rightarrow$ $\pi^+ p \pi^+\pi^+\pi^-\pi^-$	1052	events
$1c(\pi^o)$		$\rightarrow$ $\pi^+ p \pi^+\pi^+\pi^-\pi^-\pi^o$	1595	events
$1c(n)$		$\rightarrow$ $\pi^+ n \pi^+\pi^+\pi^+\pi^-\pi^-$	279	events
NO-FIT		$\rightarrow$ $\pi^+ p \pi^+\pi^+\pi^-\pi^-$ m.π^o	541	events
		$\pi^+ n \pi^+\pi^+\pi^+\pi^-\pi^-$ n.π^o		
		where $m \geq 2$ and $n \geq 1$		

The total cross-section for the six-pronged events is

$$\sigma_T = (1.32 \pm 0.04)\text{mb.}$$

and the partial cross-sections for the different channels are given in Table 4 below:

Table 4

Partial Cross-sections of Different Channels

Channel	Partial cross-section(μb.)
4c	400 ± 20
1c(π^0)	600 ± 20
1c(n)	110 ± 10
NO-FIT	210 ± 10

The χ^2 and MM^2 distributions for the events in the first two of these channels are illustrated in Figs. 22 and 23. The distributions of χ^2 and MM^2 exhibit the same feature of shifting of the centre of the peak of the 4c MM^2 distribution and high values of χ^2 for the fits, that were found with the subset of the Durham data. These effects were not considered significant for the reasons mentioned previously.

FIG. 22

HISTOGRAM OF χ^2 FOR DIFFERENT CHANNELS
(COMBINED DATA)

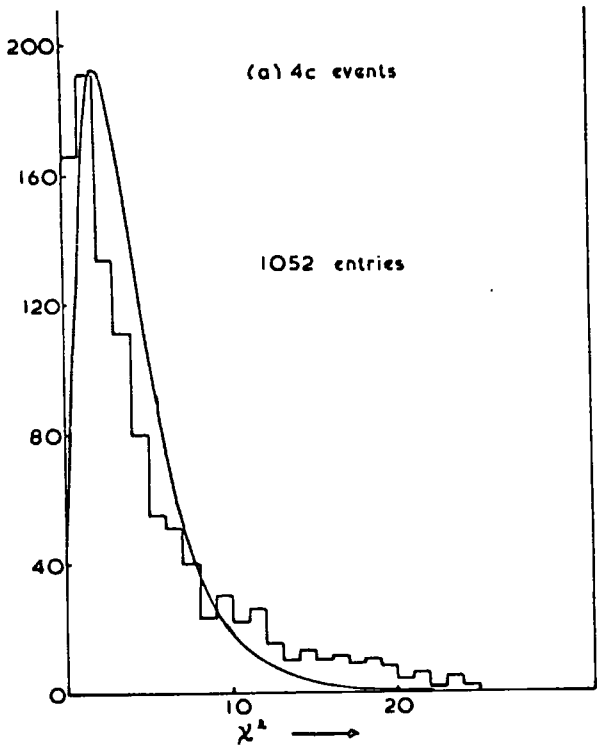

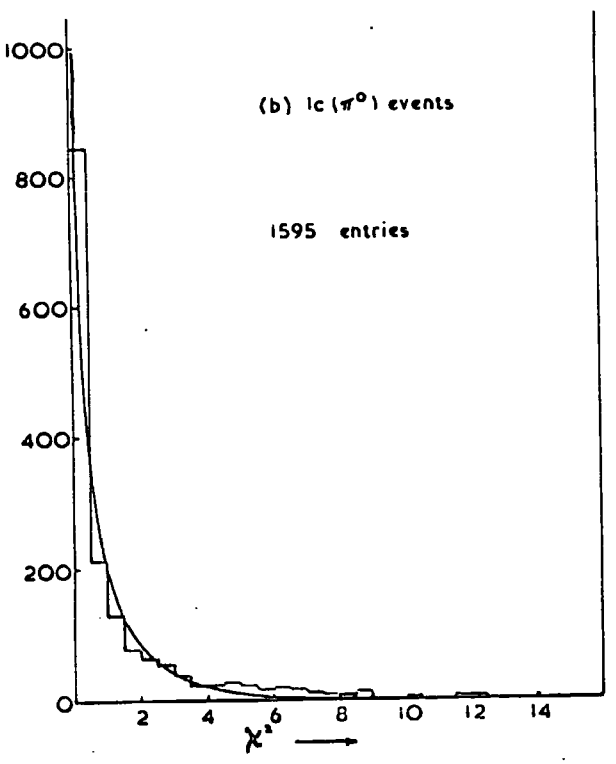

FIG. 23.

HISTOGRAM OF MM^2 FOR DIFFERENT CHANNELS
(COMBINED DATA)

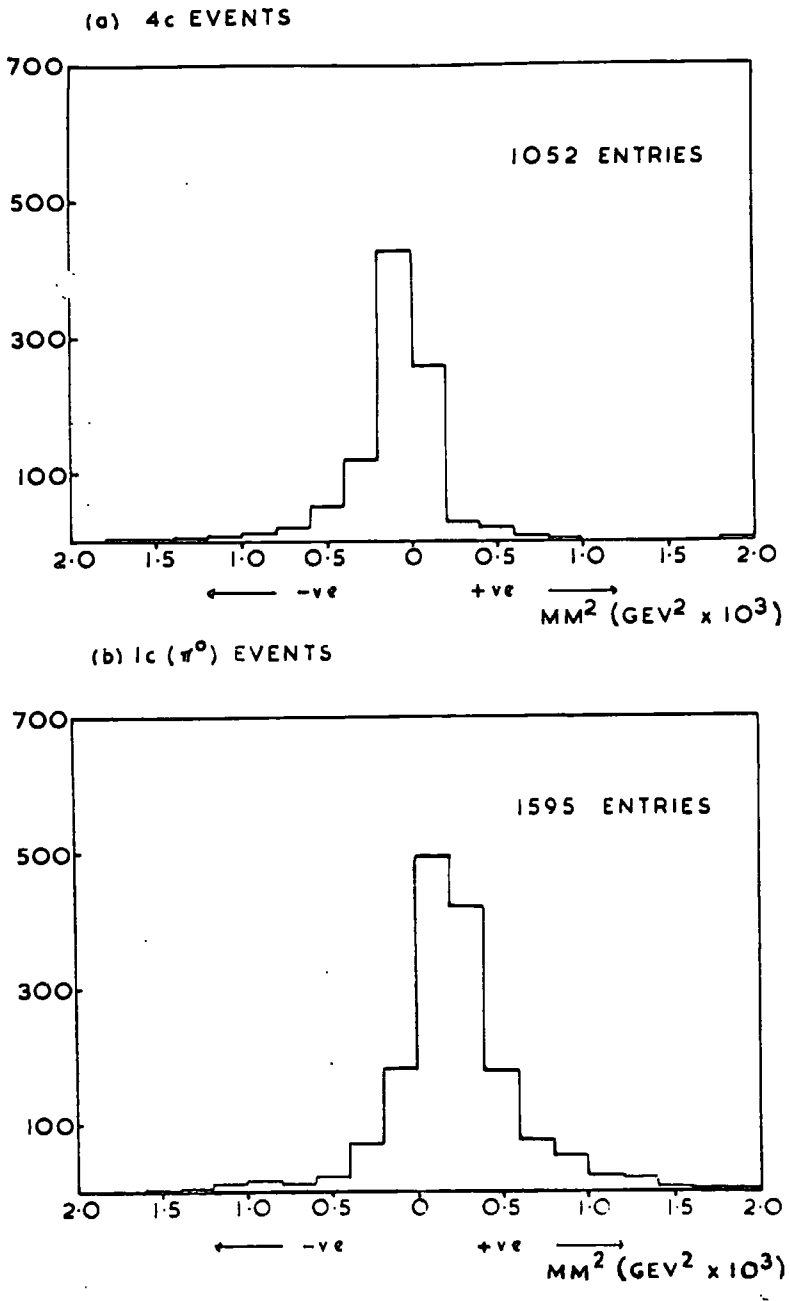

4.1 The Methods of Analysis

SUMX

The new version of CERN-SUMX was used in Paris and Bonn to produce the histograms, scatter plots, Peyrou plots, Dalitz plots and ordered lists of effective masses, angles etc. required for analysis. The program reads the D.S.T. event by event and abstracts from each record the desired quantities for compilation according to the instructions specified on the control cards. By the use of additional tests on the data it is possible to compile lists of conditional data which are extremely useful for improving the signal to noise ratio for investigating small scale effects. At the end of each physical run the abstracted data is printed out in the form of annotated diagrams.

The new version of this program has also the additional feature, through its CHARM subroutines, of allowing the computation and subsequent compilation of extra parameters from the variables specified for each event on the D.S.T. This facility has been used in the calculation of the velocity distributions and also the radial density function for the population of the Dalitz plot which was used in the estimation of the contribution of the ω^{o} resonance in the $1c(\pi^{o})$ channel.

FOWL

FOWL is a numerical integration program which uses the

Monte-Carlo method to calculate the phase space distributions of the dynamical quantities according to the statistical model. It contains the basic subroutine GENEV which generates the required number of random events by using the invariant masses of combinations of the particles in the final state. Each event is subsequently weighted according to the distribution of of Lorentz-invariant phase space viz.

$$R_n(E,\bar{p}_1,..,\bar{p}_n) = \int\prod_1^n \frac{d^3\bar{p}_i}{2E_i} \cdot \delta^3\left(\sum_1^n \bar{p}_i - \bar{P}\right)\delta\left(\sum_1^n E_i - E\right) \quad \ldots (1)$$

where

E = Total energy of the system

$\bar{P}$ = Total momentum of the system

E_i and p_i = Energy and momentum of the i'th of the n particles.

The individual particles are then spatially re-oriented to give a symmetric distribution for the total production spectrum in the centre of mass system.

The dynamical parameters whose phase space distributions are required e.g. effective masses, momenta, momentum transfers production angles etc., are specified in a separate subroutine. After the generation of the specified number of events, these distributions are printed out as normalised, annotated histograms; the accuracy of the distributions being dependent upon the

the total number of events generated.

The weight with which each event is plotted on the histograms may be modified by any function of the interaction variables to simulate a specific interaction mechanism such as the production of intermediate resonant states and peripheral interactions.

The original program was suitably modified by the author to accommodate the higher number of particle combinations obtained for events with six and seven particles in the final state. Further development was also required to allow the inclusion of arbitrary cut-offs with respect to the dynamical parameters to allow a full simulation of the techniques available in SUMX.

Fitting Techniques

The contribution of resonances in the different reaction channels was estimated by fitting the appropriate effective mass spectra with theoretical distributions containing different proportions of resonance and determining the minimum χ^2 of the fit. Mapping techniques were employed in order to avoid any false minima and also to determine the goodness of the fit in each case.

When generating a resonance of r particles in the theoretical distributions prepared with FOWL, care was taken to

use the appropriate (n - r) body phase space. This is especially important in the case of the N^{*} (1236) which has such a low Q-value of 160 MeV that the value of the momenta of the two secondary particles in their own centre of mass has a large variation of some 40% within the mass region of the resonance between 1180 and 1300 MeV.

In order to be able to estimate the contribution of the combined production of two resonances simultaneous fits were made to the two effective mass distributions to determine the minimum of the product of the two individual χ^2. The theoretical distributions used were a linear addition of the individual phase space distributions for single production of the first resonance, $\phi(R_1)$, single production of the second resonance, $\phi(R_2)$, and combined production of these two resonances, $\phi(R_1+R_2)$, together with pure phase space $\phi(s)$.

If the decay schemes of R_1 and R_2 produce r_1 and r_2 individual particles then for an apparently 'n' body final state the resulting distribution will be a sum of the n, $n-r_1$, $n-r_2$ and $n-(r_1+r_2)$ body phase spaces. The best fit solution is obtained for that linear combination of the phase space curves that give a minimum of the function

$$F = \chi_1^2 \cdot \chi_2^2$$

where

$$\chi^2_1 = \sum \left[E'_i - \left\{ \alpha_1 \phi'_i(R_1) + \alpha_2 \phi'_i(R_2) + \alpha_3 \phi'_i(R_1+R_2) + (1-\alpha_1-\alpha_2-\alpha_3)\phi'_i(s) \right\} \right] \quad \ldots (2)$$

and similarly for the other mass distribution.

When these parameters have been determined it is possible to produce the appropriate theoretical curves to simulate the backgrounds of the effective mass distributions of other particle combinations and so estimate the small enhancements of weakly produced resonances.

4.2 Resonance Production in the 4c Channel

A complete survey was made of the effective mass spectra of all possible combinations of particles as well as the distributions for the dynamic parameters Δ^2, β^* and cos θ for all the individual particles and the particle combinations. From the mass spectra the presence of quite large amounts of the well known resonances Δ^{*++} and ρ^0 were detected. There was not found, however, evidence for the presence of higher mesonic or baryonic resonances and consequently there is no quasi two-body production.

The production mechanism of the resonances was investigated and the results obtained strongly favoured a non-statistical mode of production. Attempts were made to simulate this mechanism by applying a peripheral method for their production using the well established "one pion exchange model" that has achieved a large measure of success in low multiplicity interactions.

The π^+p and π^-p Effective Mass Spectra

The distributions of the effective masses of all the π^+p and π^-p combinations of particles are illustrated in Figs. 24 and 25. There is a large enhancement in the π^+p spectrum within the mass region of the Δ^{*} (1236) resonance which is absent from the π^-p spectrum. The position of this resonance is shifted downwards by some 20 MeV, from the generally accepted

FIG. 24

4C EVENTS: HISTOGRAM OF EFFECTIVE MASSES OF $\pi^+ p$ COMBINATIONS.

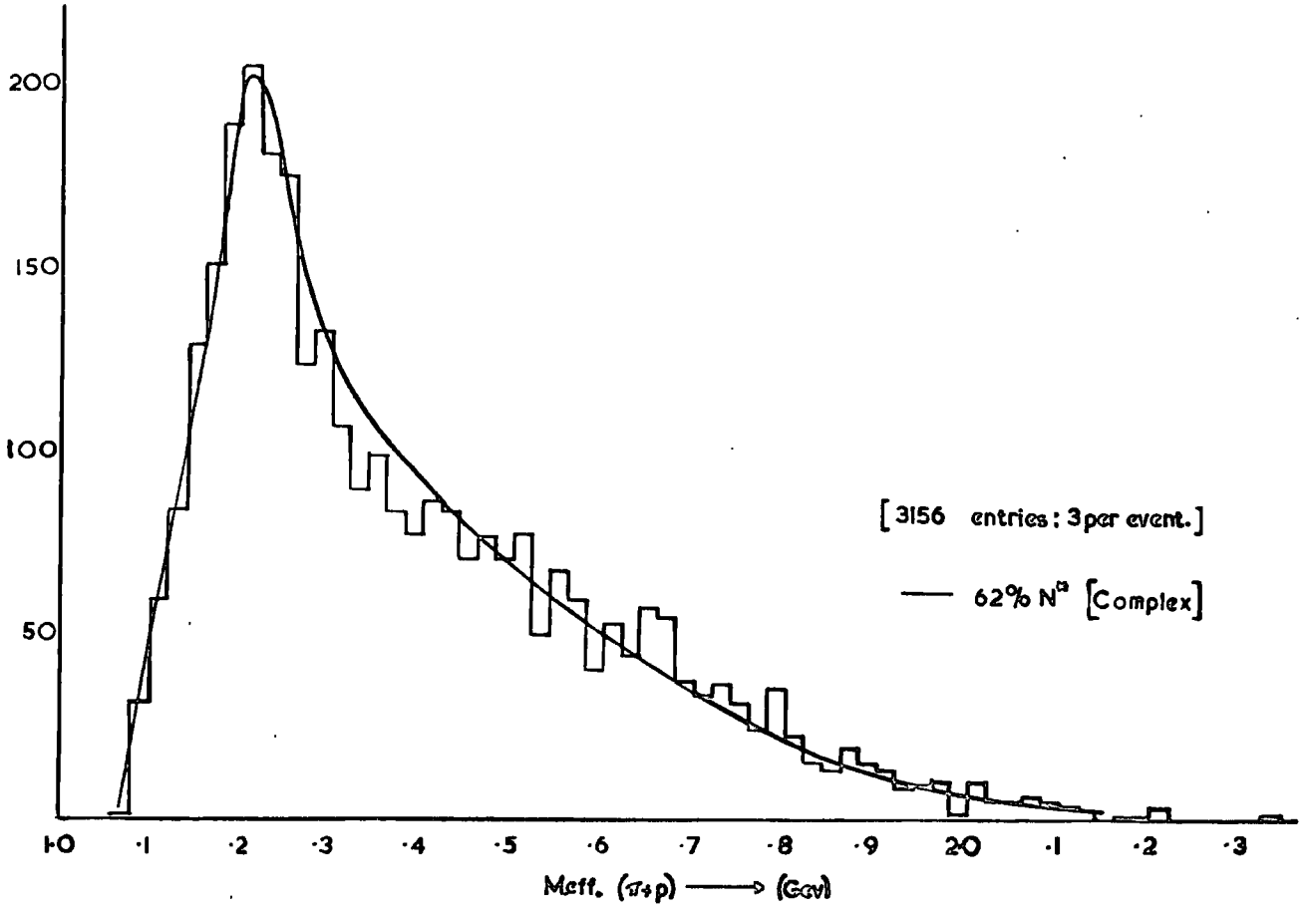

Fig 25

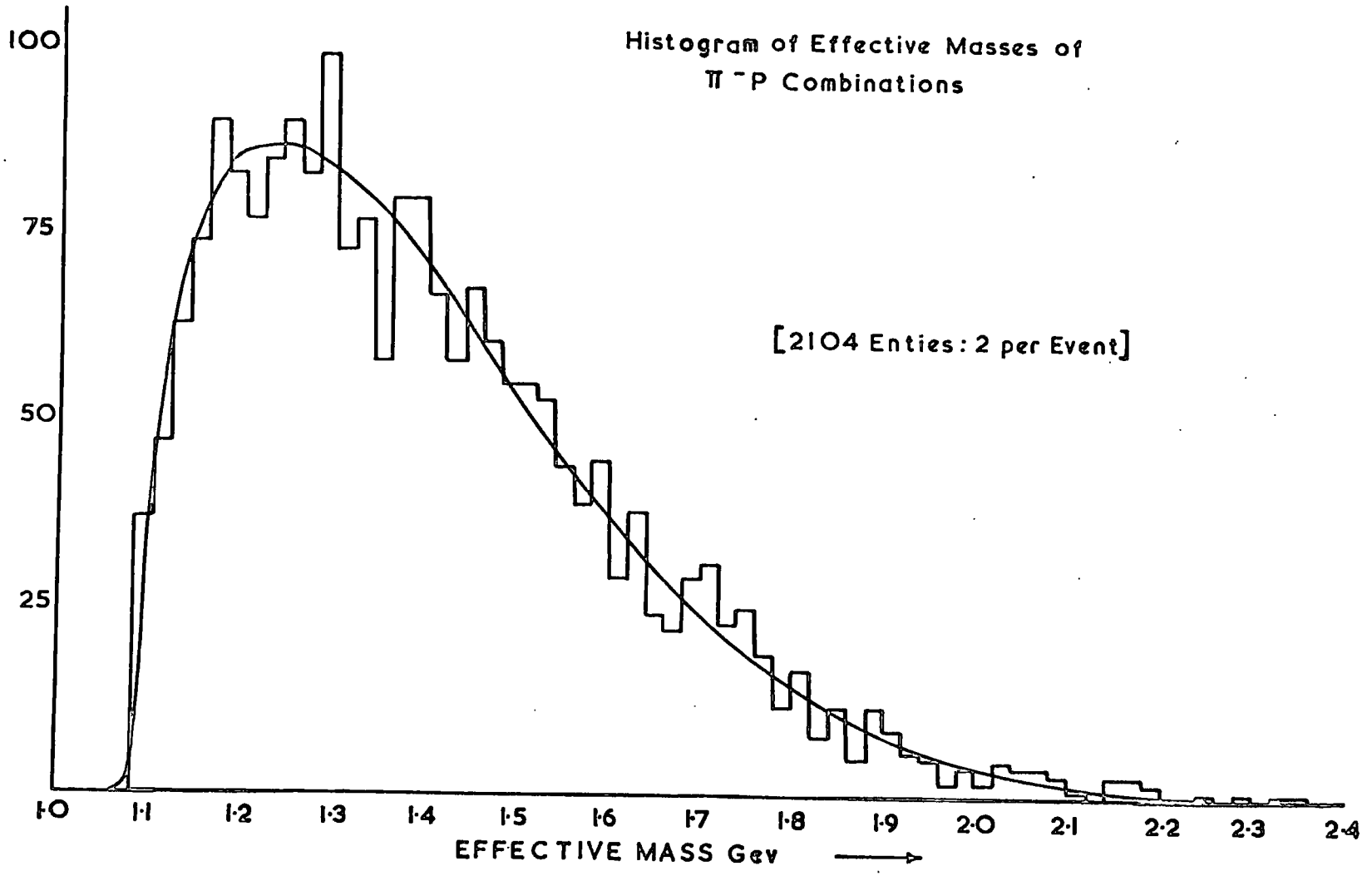
4c Events
Histogram of Effective Masses of
π⁻P Combinations
[2104 Entries: 2 per Event]
100
75
50
25
1·0
1·1
1·2
1·3
1·4
1·5
1·6
1·7
1·8
1·9
2·0
2·1
2·2
2·3
2·4
EFFECTIVE MASS Gev

central mass value of the resonance is also quite obvious narrowing of this peak. The apparent shift and reduction of the width are indicative of an angular momentum barrier affecting the decay of the resonance. The shift is of the same order as that expected from the decay of a P state which, as shown by Jackson (1964), the displacement δ is given in terms of the width Γ_o and the masses m_1 and m_2 of the two decay particles as

$$\delta = M_o - M_{peak} \simeq \Gamma_o \frac{(2l+1)}{3} \frac{\Gamma_o}{M_o} \frac{(M_o^4 - (m_1^2 - m_2^2)^2)}{(M_o^4 - 2(m_1^2+m_2^2)M_o^2 + (m_1^2 - m_2^2)^2} \quad \ldots (3)$$

For l=1 the value of M_{peak} for the $N^{*}(1236)$ is 1213 MeV.

The best fit to the experimental distribution was obtained with a complex Breit-Wigner shape given by

$$\frac{\Gamma_{(M)}}{\frac{(M^2 - M_o^2)^2}{M_o^2} + \Gamma^2_{(M)}} \quad \ldots (4)$$

with the width given by

$$\Gamma = \Gamma_o (p/p_o)^{2l+1} \cdot \rho(M)/\rho(M_o) \quad \ldots (5)$$

where p is the momentum of the decay particles in the rest system of the resonance. The parameters used were $\Gamma_o = 125$ and $M_o = 1236$ together with the empirical expression $\rho(M) = (0.0436 + p^2)^{-1}$ as suggested by Anderson (1956). The best fit to the whole experimental distribution was obtained for an

dominance of the final state distributions

viz. $p^{+} p \pi^{+} \pi^{-} \pi^{-}$

and $p^{+} p \pi^{+} \pi^{0} \pi^{-}$

which corresponds to $59 \pm 5\%$ of N^{*}, whilst fitting in the N^{*} mass region alone revealed a contribution of some $62 \pm 6\%$.

There remained however some significant broad enhancement for the higher mass region of the $\pi^{+} p$ spectrum which is not visible in the $\pi^{-} p$ distribution. This enhancement cannot be attributed to the production of a small amount of any known resonance and has been interpreted as a reflection of some dynamical mechanism of resonance production.

The $\pi^{+} \pi^{-}$ Effective Mass Spectrum

The neutral di-pion effective mass spectrum for all possible combinations is illustrated in Fig. 26. A large, narrow enhancement is visible within the mass region of the neutral ρ^{0} meson but shifted by some 30 MeV. from the generally accepted central mass value of 765 ± 4 MeV. Although, this shift is larger than expected for the decay of a P state, the discrepancy may be explained by the effect of the multiplication of the Breit-Wigner function by the appropriate 5-body phase space which falls rapidly within this region.

A fit was made to the experimental distribution with six body pure phase space and five body phase space containing the

FIG. 26

4c EVENTS : HISTOGRAM OF EFFECTIVE MASSES OF ($\pi^+ \pi^-$) COMBINATIONS

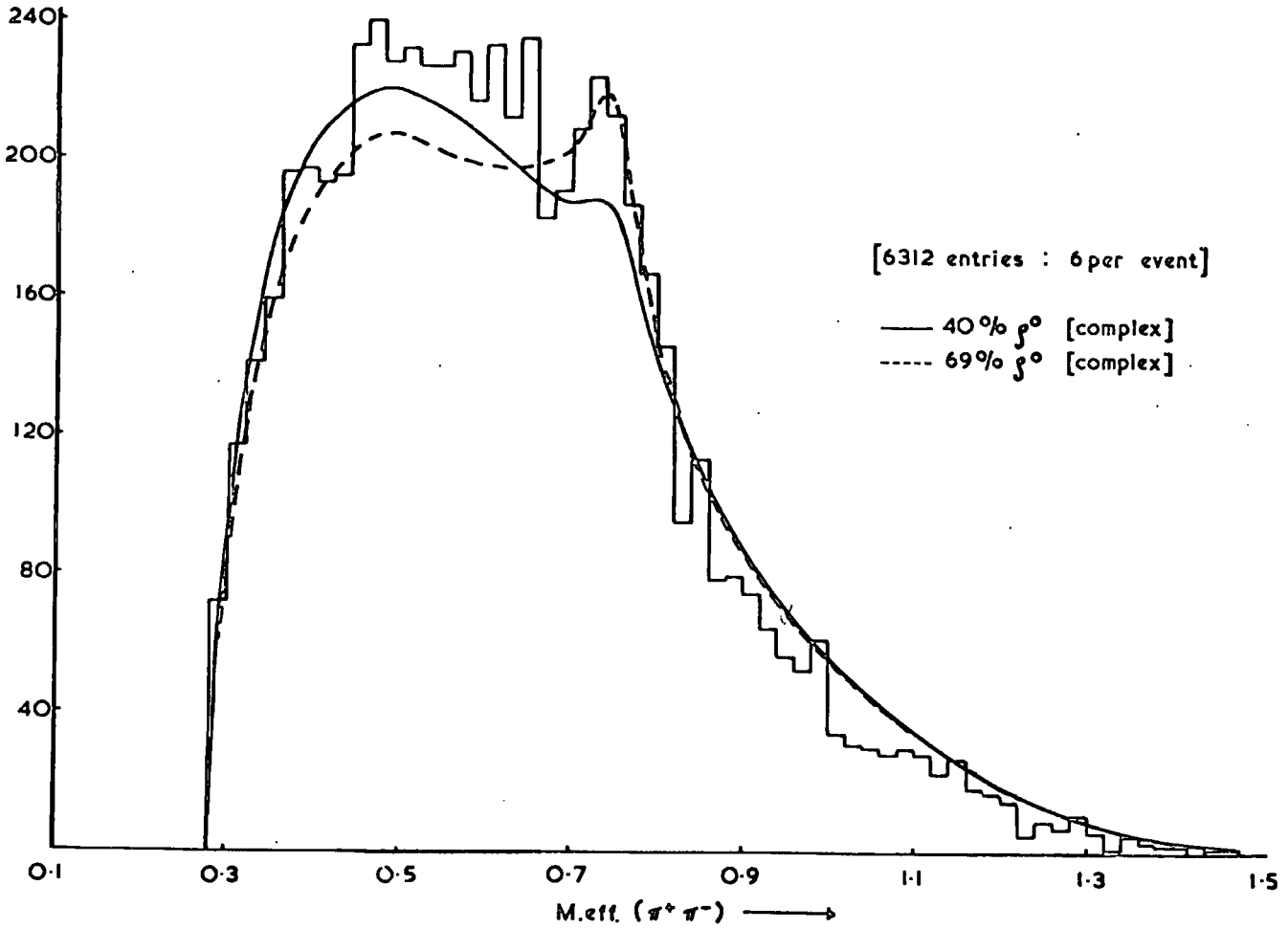

ρ° whole mass distribution varied according to the complex Breit-Wigner functions given in equations (3),(4) and (5) of this section with $\rho(m)$ described by the empirical function

$$\rho(m) = (p_o^2 + p^2)^{-1}$$

The fit to the whole mass region gave an estimate of only $42 \pm 5\%$. The best fit obtained of the ρ mass region corresponded however to a much increased contribution of ρ° mesons in 69 ± 6 of the interactions. The appropriate curves are illustrated on the experimental distribution.

The curve corresponding to 69% ρ° production gives a reasonable fit in the mass region of the resonance although quite appreciable disagreements are observed for both the higher and lower mass regions.

No evidence was found for the production of the $\epsilon^{\circ}(720)$ which has been observed in a similar distribution in the experiment at 4 GeV carried out by the ABBHF collaboration.

The Multi-pion Effective Mass Spectra

The $\pi^+\pi^+\pi^-$ and $\pi^+\pi^-\pi^-$ effective mass distributions, Figs. 27 and 28, have been examined for evidence of the A_1 and A_2 mesons, both of which now appear to be firmly established resonances.

The effective mass plots show no significant enhancements in either distribution although there is a marked disagreement of the background with the phase space curves. This effect

FIG. 27

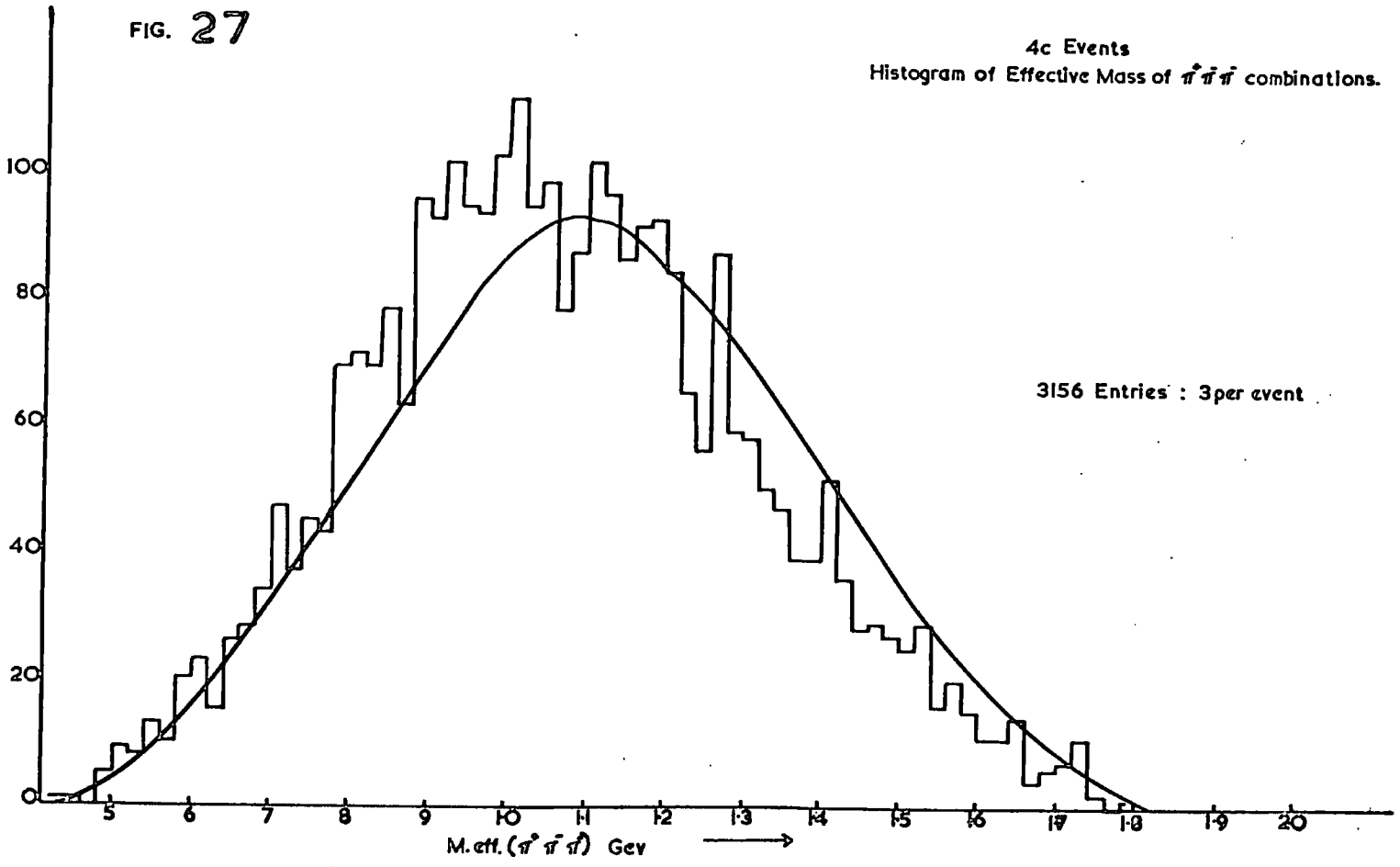
4c Events
Histogram of Effective Mass of $\pi^+\pi^-\pi^-$ combinations.
3156 Entries : 3per event
100
80
60
40
20
0
5
6
7
8
9
10
11
12
13
14
15
16
17
18
19
20
M. eff. ($\pi^+\pi^-\pi^-$) Gev

Fig. 28

4c EVENTS : HISTOGRAM OF EFFECTIVE MASSES OF ($\pi^+\pi^+\pi^-$) COMBINATIONS

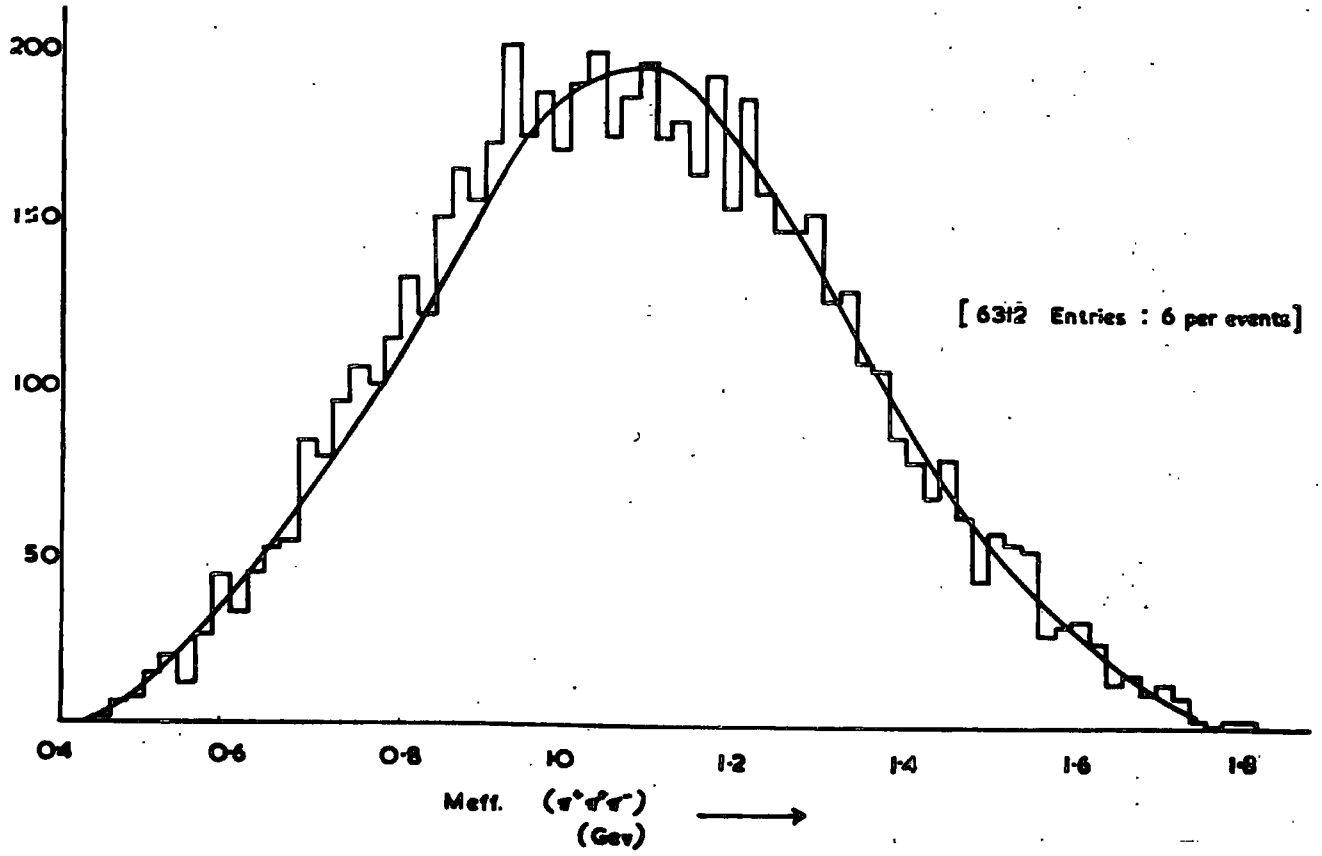

has been attributed to the large production of N^{*} and ρ^{o} and also to the dynamics of the production of these resonances.

Further investigations were made into the $\pi^{+}\pi^{+}\pi^{-}$ combinations by imposing the conditions that the three pion combination should contain at least 1 di-pion combination which lies within the mass region of the ρ, $(670 \leq M_{\pi^{+}\pi^{-}} \leq 850)$ and also that the effective mass of the remaining positive pion and the proton should be in the N^{*} region, $(1120 \leq M_{\pi^{+}p} \leq 1320)$. The distribution obtained, Fig. 29, shows a 3 standard deviation enhancement in the A_2 region but only a non-significant, broad excess in the region of the A_1. The A_2 peak corresponds to at most some 3 ± 1 of these particles in this channel. Thus the large proportion of ρ^{o} mesons observed cannot be attributed to the decay of the known $\pi\rho$ resonances which are not copiously produced in this channel.

The 4-pion Effective Mass Spectrum

The effective mass distribution of the $\pi^{+}\pi^{+}\pi^{-}\pi^{-}$ particle combinations is illustrated in Fig. 30. Although the agreement of the background with the phase space curves for the reasons explained previously, there is no obvious narrow enhancement in the mass regions of either the $f^{o}(1250)$, the $f^{o}{}'$ (1500) or in the wide mass region of the recently reported $g(1670)$ (Goldberg et al. 1965) which has since been resolved into three

Fig. 29

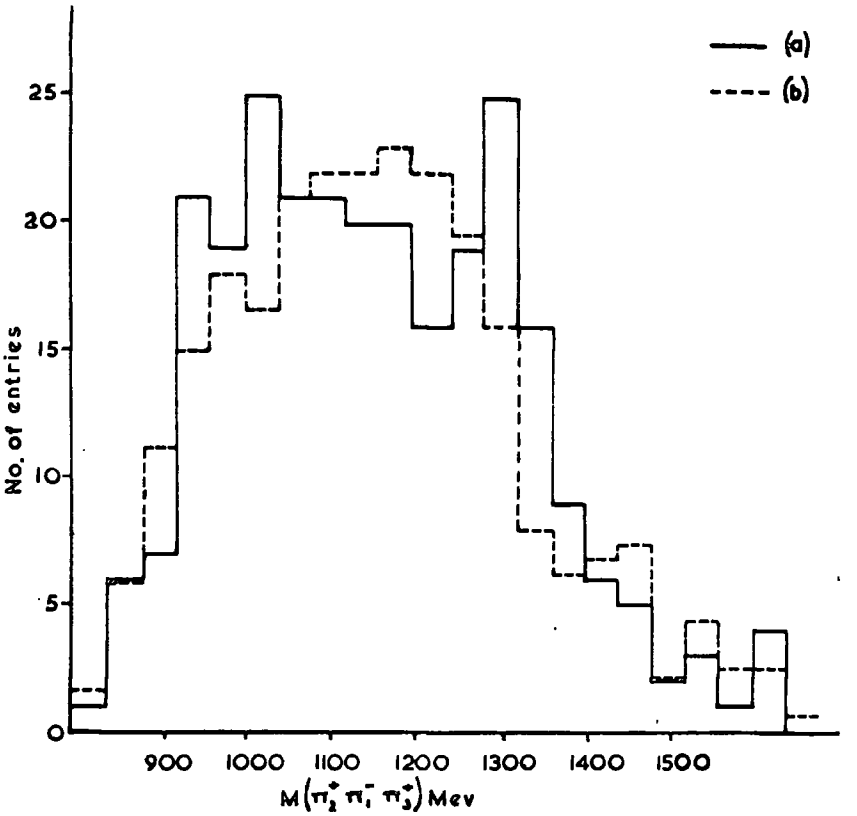

EFFECTIVE MASS of $\pi_2^+ \pi_1^- \pi_3^+$ FOR
$1120 < M(p\pi_1^+) < 1320$ Mev.
$670 < M(\pi_2^+ \pi_1^-) < 850$ Mev.
and
(a) $-1 < \cos \Theta\ p\pi_1^+ < -0.75$.
(b) $-0.75 < \cos \Theta\ p\pi_1^+ < 0$.

FIG. 30

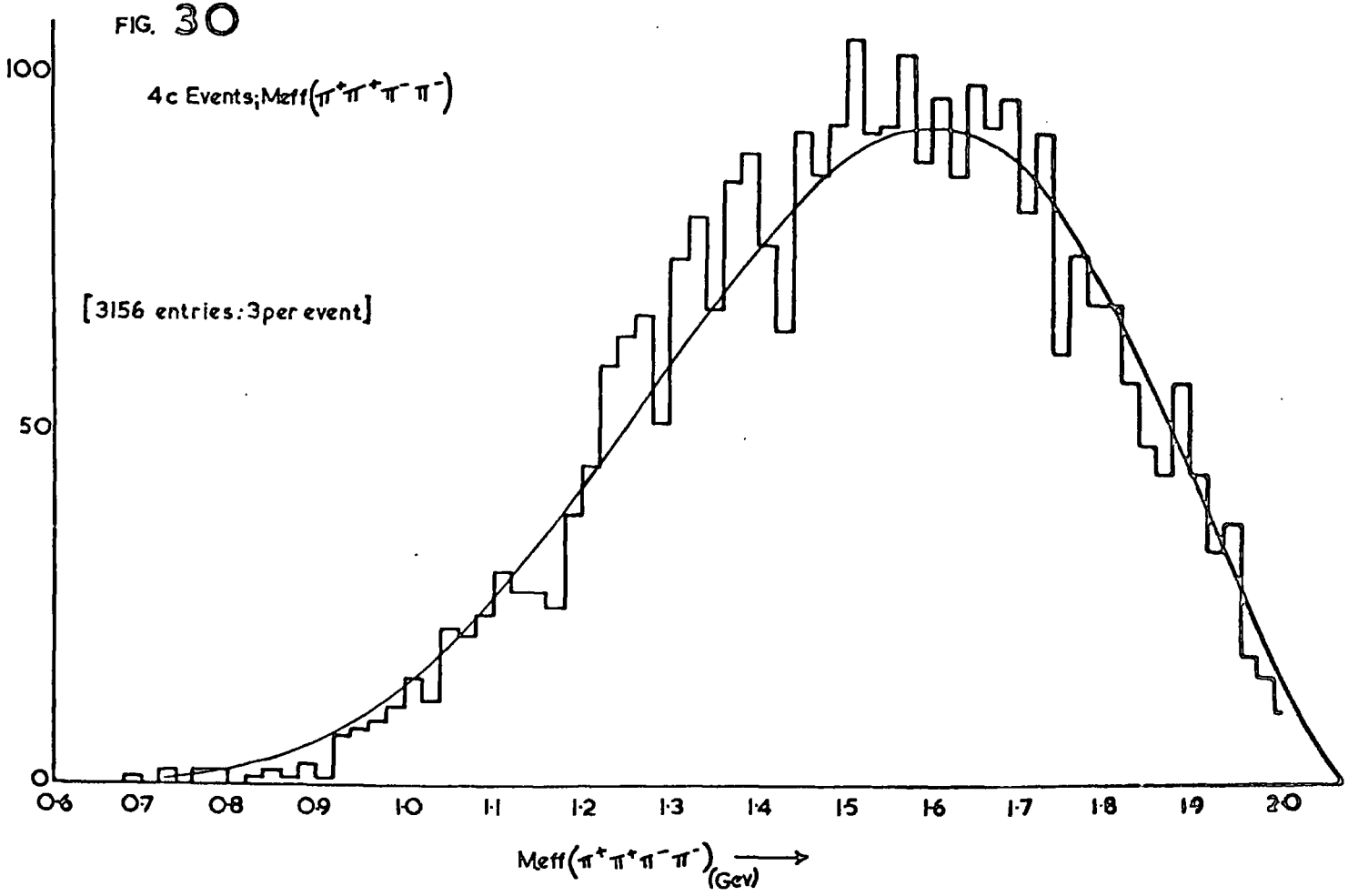
4c Events; Meff($\pi^+\pi^+\pi^-\pi^-$)
[3156 entries: 3 per event]
100
50
0
0·6
0·7
0·8
0·9
1·0
1·1
1·2
1·3
1·4
1·5
1·6
1·7
1·8
1·9
2·0
Meff($\pi^+\pi^+\pi^-\pi^-$) (Gev) ⟶

separate peaks (Maglic et al. 1966).

Thus it would appear that there is no strong production of a four pion resonance to give, together with the N^{*} an appreciable proportion of quasi-two body interactions in a manner similar to that observed in the lower multiplicity interactions.

In order to confirm this investigations were made into the effective mass spectra of those combinations of secondary particles that contain a proton. A search was made for copious production of a higher baryon resonance which could decay in to an N^{*} and two pions.

Higher Baryon Resonances

The agreement of the effective mass spectrum of combinations of $p\pi^{+}\pi^{-}$, Fig. 31, with the phase space curve is quite close excepting for a slight broad enhancement in the region of low effective masses. There is no indication of isobar production in this distribution. In the case of the corresponding distribution for $p\pi^{+}\pi^{+}$ combinations, Fig. 32, a narrow enhancement is observed in the region of 1580 MeV which corresponds to a similar peak observed by Goldhaber et al. (1965) for $\pi^{+}p$ interactions at 3.65 GeV/c.

To estimate the number of events in this peak the $\pi^{+}\pi^{-}p$ spectrum was used as background and fitted to the $\pi^{+}\pi^{+}p$ distribution in the higher mass region away from the enhancement. The

Fig. 31

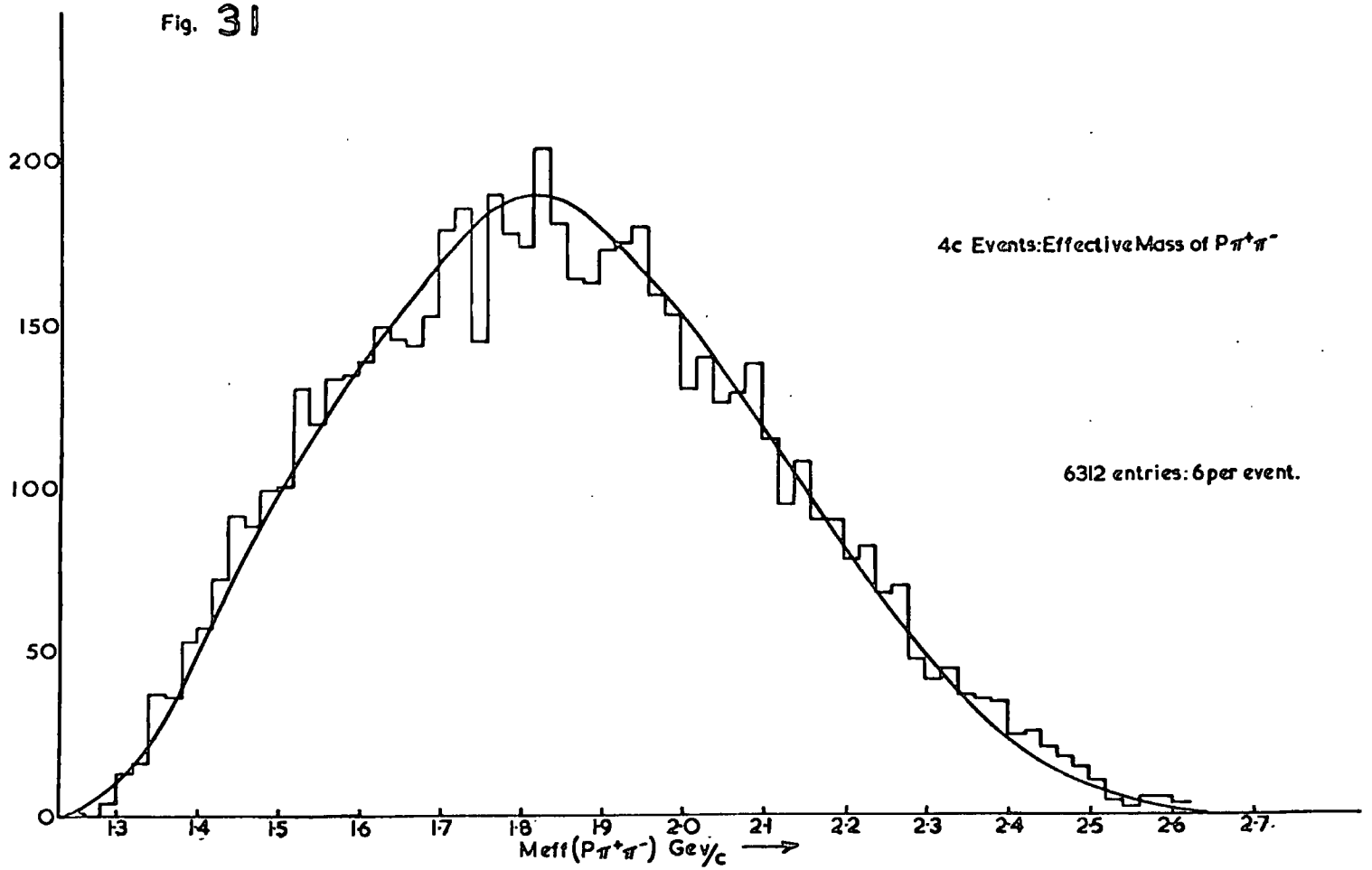
200
150
100
50
0
1·3
1·4
1·5
1·6
1·7
1·8
1·9
2·0
2·1
2·2
2·3
2·4
2·5
2·6
2·7
Meff (Pπ⁺π⁻) Gev/c
4c Events: Effective Mass of Pπ⁺π⁻
6312 entries: 6 per event.

FIG. 32

4c EVENTS : HISTOGRAM OF EFFECTIVE MASSES OF $\sigma^+\sigma^+p$ COMBINATIONS

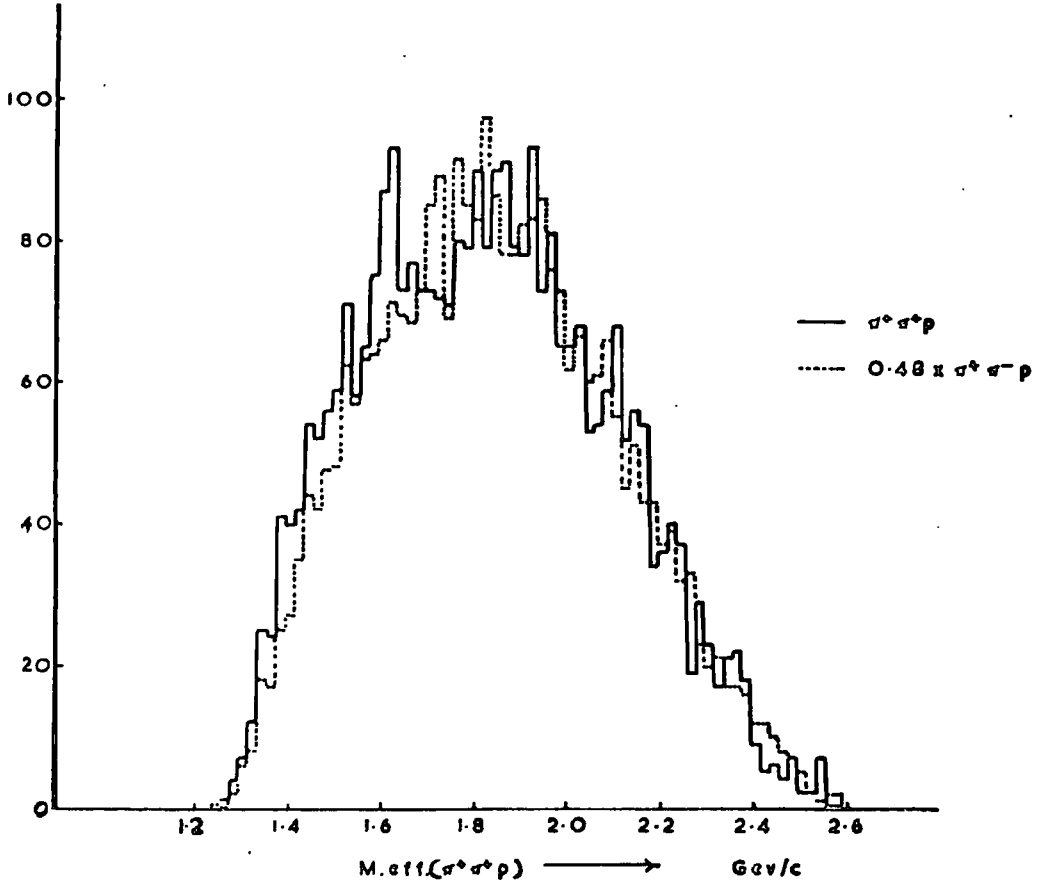

best fit obtained revealed a broad excess of $\pi^+\pi^-p$ combinations over the background in the low mass region. This effect has been interpreted as a dilution of the signal of N^{*} reflection in the $\pi^+\pi^-$ combinations as only true N^{*} enters twice in the three possible $\pi^+\pi^-p$ combinations for each event, whereas for $\pi^+\pi^-$ it is only twice in the possible combinations. Thus it was not possible to obtain a background that was in good agreement with the $\pi^+\pi^-$ experimental distribution. Moreover, the enhancement lies in the broad reflection and is less than three standard deviations above the fitted background. This peak therefore cannot be considered as significant proof of the existence of a $T = 5/2$ isobar and is most probably a consequence of the production of the N^{*} 3/2 isobar.

Combined Production of Resonances

An attempt was made to estimate the degree of simultaneous production for the only two resonances that have been observed to be strongly produced in the sample of 4c events, viz. the N^{*} and the ρ^{0}. The fitting of single Breit-Wigner functions to the enhancements in the individual mass spectra has been shown to give overall phase space curves that are not in good agreement with either of the experimental backgrounds of the two histograms. Consequently a simultaneous multi-resonance fit to both of the histograms was made in the manner described in section 4.4.

No true minimum was found, however, for the resultant three-dimensional surface; the lowest point registered corresponding to the condition of minimal combined production. This effect was interpreted as an inability of the small reflexions of the statistically produced resonances to simulate fully the large distortions of the experimental histograms, especially those of the di-pion combinations. It was therefore concluded that there existed some additional, non-statistical mechanism which was accentuating the distortion for the background for these combinations of particles not in a resonance.

It was found possible to obtain a somewhat inaccurate estimate of the degree of correlation from the triangle plot of the effective masses of the $\pi^+\pi^-$ and π^-p combinations. A fit was made to the density of points in the wide, overlapping bands of the $\pi^+\pi^-$ and π^+p combinations for the ρ and N^* mass regions respectively. The best fit obtained by different proportions of the four possible phase space configurations corresponded to resonance contributions of:

$$N^* = 19 \pm 4\%$$

$$N^* \rho^0 = 50 \pm 11\%$$

$$\rho^0 = 8 \pm 4\%$$

which are in agreement within the rather large statistical errors with the previous estimate of resonance production. Furthermore, the fit obtained is not significantly different from the normal statistical estimate of 36% for correlated production,

therefore it is not possible to imply any mechanism of combined production of the N^{*} and the ρ^{o}.

Investigations were also carried out to determine whether any double production of ρ^{o} mesons occurred. The correlations for resonance production in the overlapping bands of the appropriate triangle plot were found to be quite consistent with single ρ^{o} production.

4.3 Properties of the Channel

One Particle Distributions

The angular distributions for the emission of the three different particles the π^+, π^- and the proton in the centre of mass system are illustrated in Fig. 33(a), (b) and (c). The statistical model prediction of uniform phase space distribution is strongly violated with large forward-backward asymmetries in the cases of the proton and the negative pion. The observed asymmetry is much smaller in the case of the positive pion. The asymmetry parameters for each of these particles are given in Table 5 below:

Table 5

4c Events:

Asymmetry Parameters, A, for the Individual Particles

Particles	$A = (F-B)/(F+B)$
p	-0.34 ± 0.03
π^+	0.05 ± 0.02
π^-	0.11 ± 0.02

The asymmetries in the centre of mass system are also evident in the distributions for the momentum components, $p_{||}$ and $p_\perp$, of the individual particles as illustrated in Figs. 34, 35 and 36. The $p_{||}$ distributions for the protons

FIG. 33

4c EVENTS : ANGULAR DISTRIBUTIONS OF THE INDIVIDUAL PARTICLES IN THE CENTRE OF MASS SYSTEM

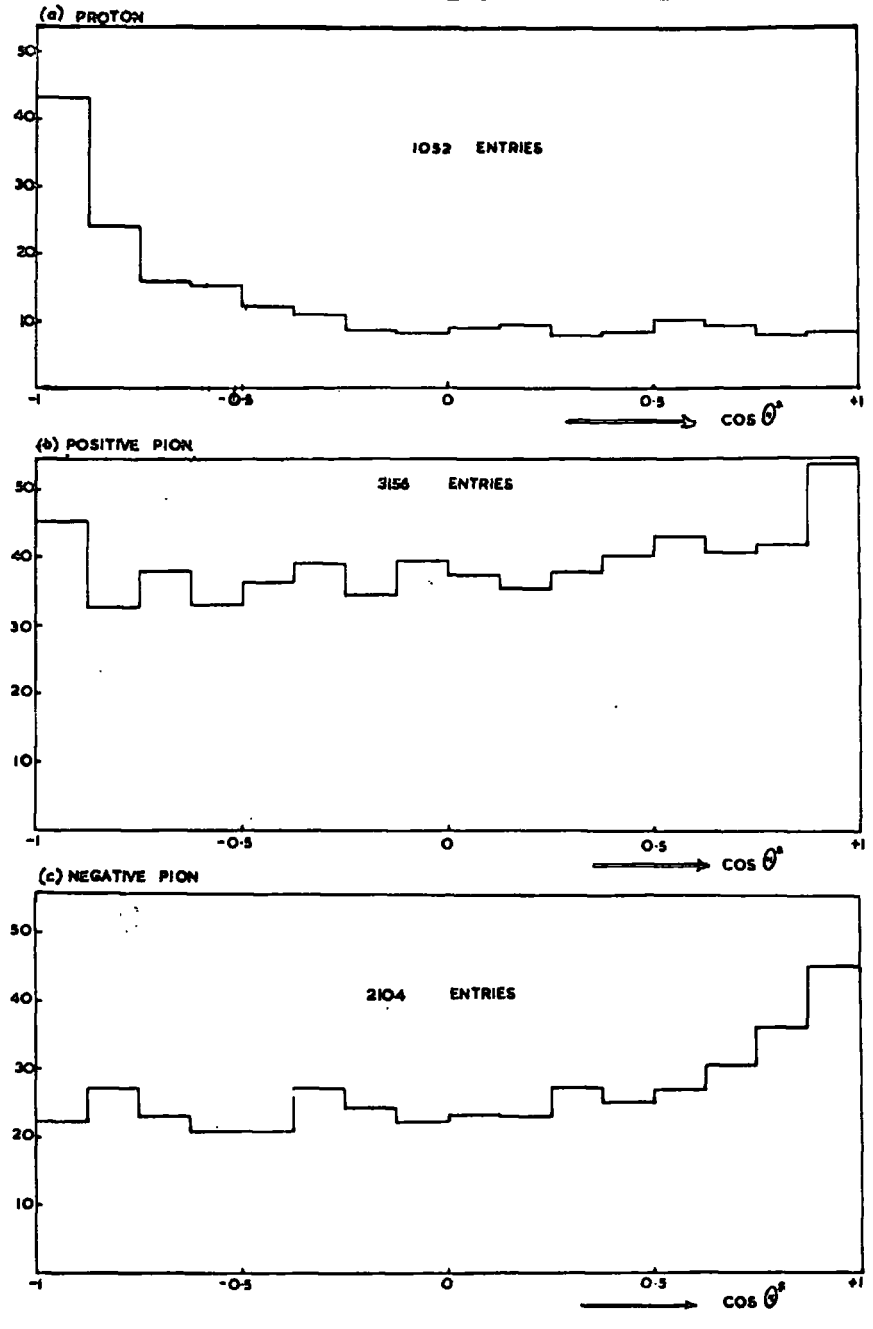

FIG. 34

4c EVENTS : HISTOGRAM OF MOMENTUM COMPONENTS OF PROTONS

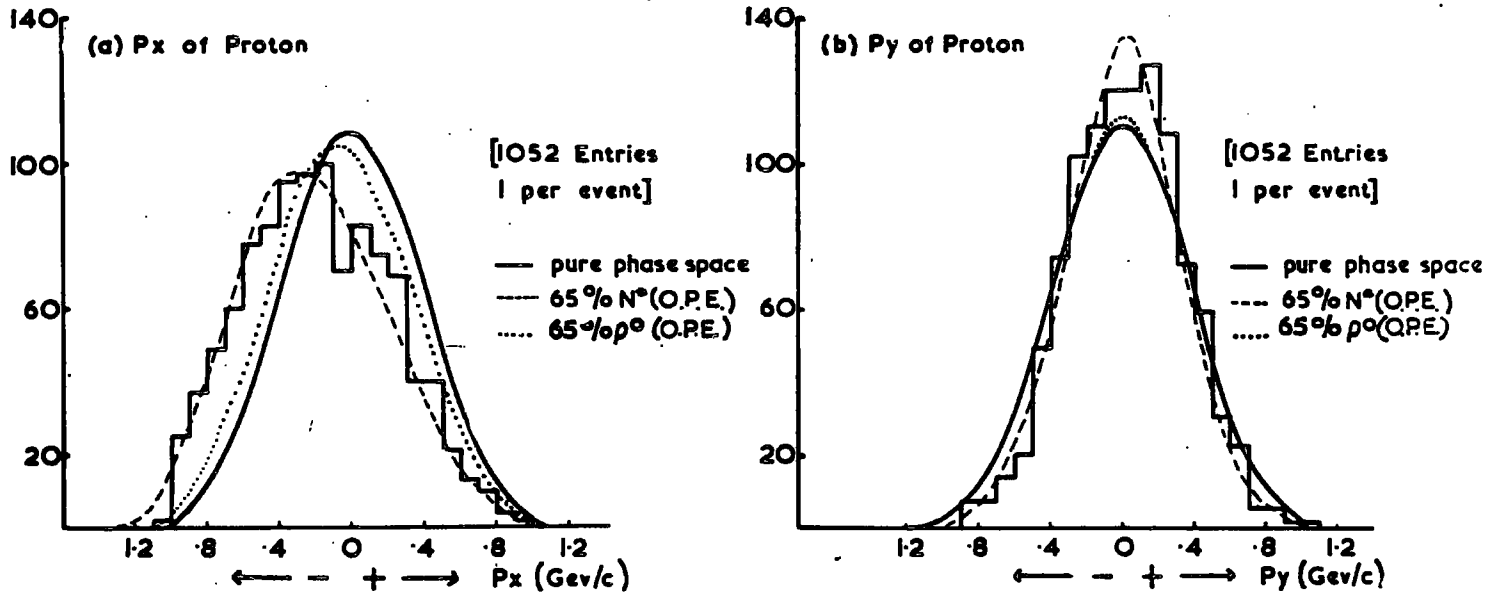

Fig. 35

4c EVENTS : HISTOGRAM OF MOMENTUM COMPONENTS OF POSITIVE PIONS

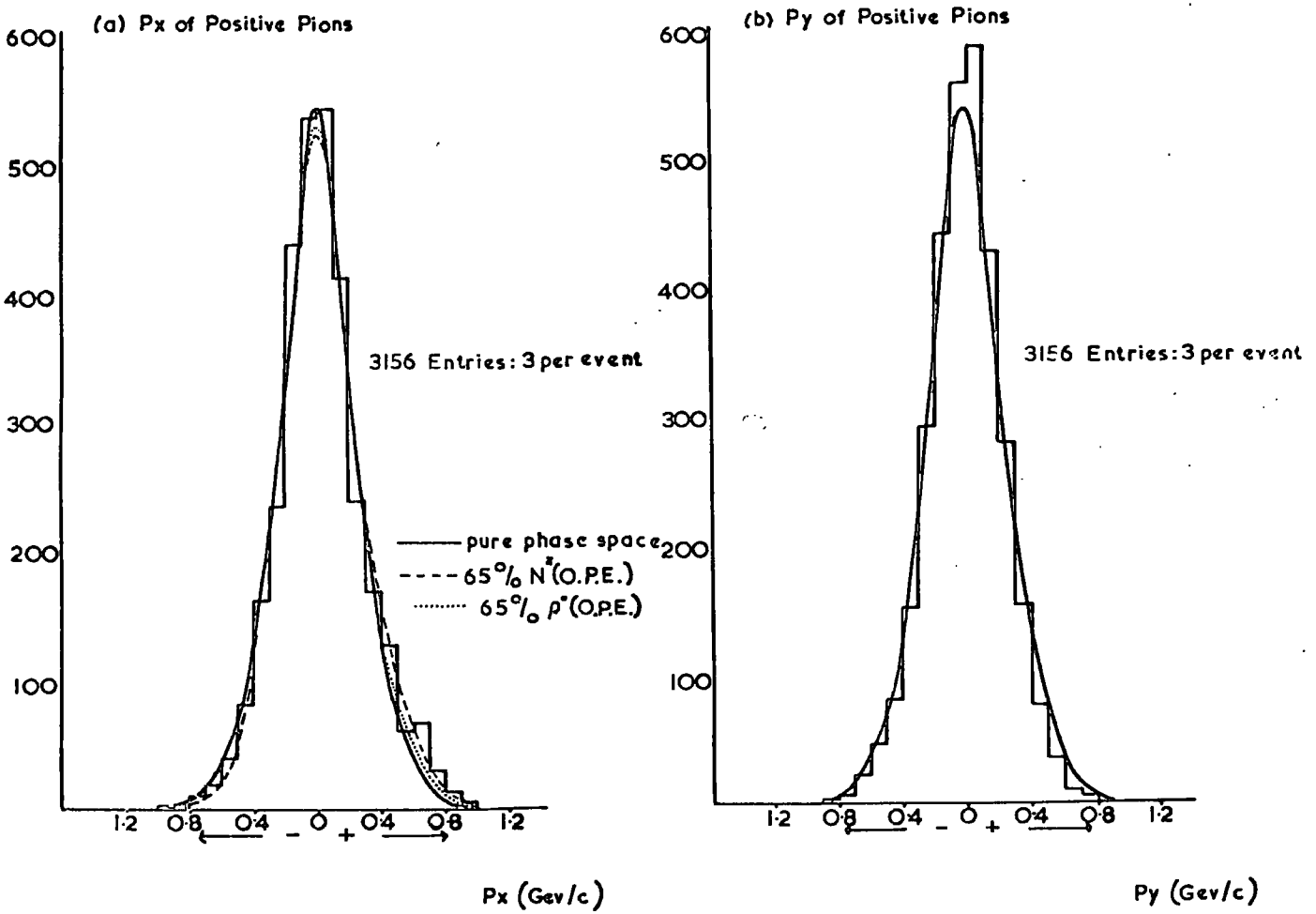

FIG. 36

4c EVENTS : HISTOGRAM OF MOMENTUM COMPONENTS OF NEGATIVE PIONS

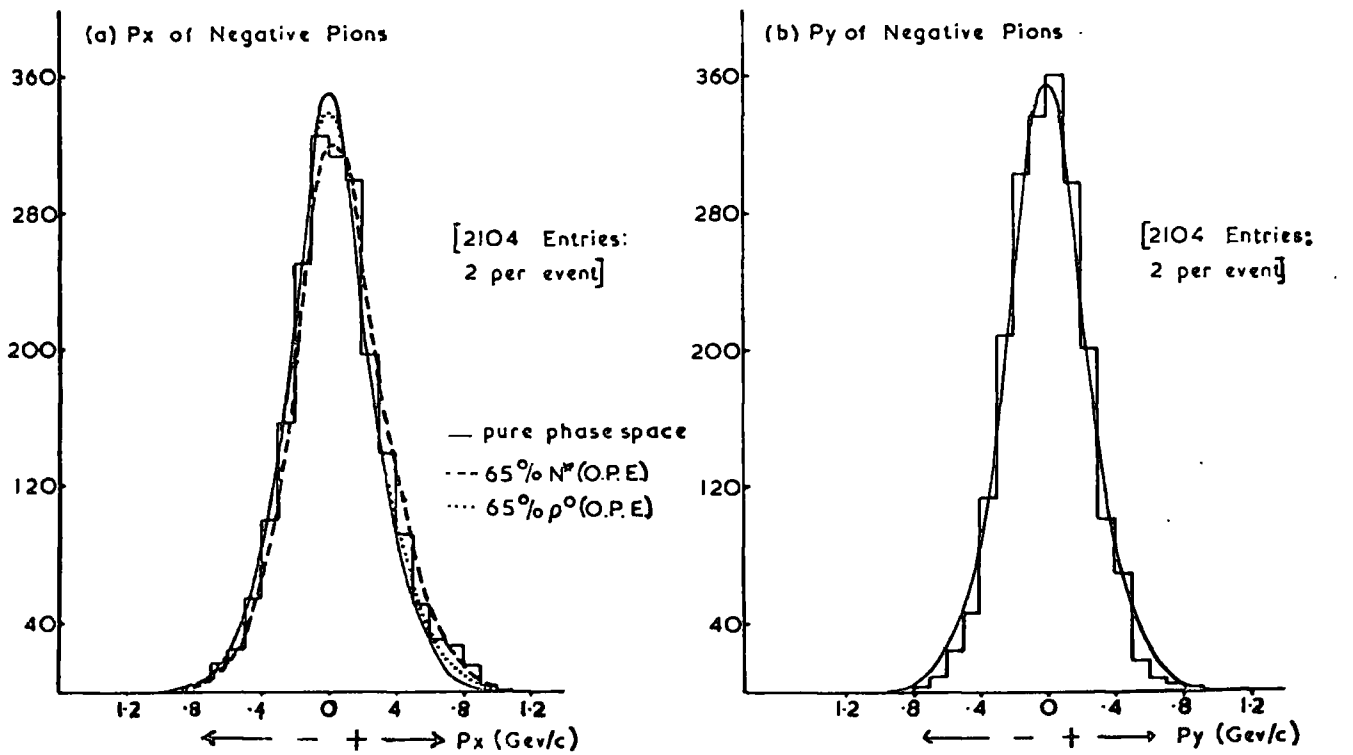

exhibit a large backward shift and appreciable broadening whereas the p_y distribution shows a slight narrowing only.

Similar effects are to be seen in the distributions of the negative pions but the effect is not so marked in the corresponding distributions for the positive pions.

These effects have been summarised in terms of "elongation" parameters α_x and α_y for the two orthogonal directions in the centre of mass system, α_x is defined by

$$\alpha_x = \sigma_{T_x} / \sigma_{stat.}$$

where

$$\sigma_{T_x} = \langle p_x^2 \rangle - \langle p_x \rangle^2$$

is the observed standard distribution of p_x about its mean value and σ_{stat} is the standard width of the distribution expected from the statistical model. α_y is defined in a corresponding manner.

The values of these parameters for the individual particles are given in Table 6 below:

Table 6

4c Events:

Elongation Parameters, α, for the Individual Particles

Particle	α_x	α_y
p	1.10 ± 0.045	0.87 ± 0.03
π^+	1.09 ± 0.02	0.94 ± 0.02
π^-	1.14 ± 0.02	0.94 ± 0.02

The statistically significant distortions of the momentum distributions as shown by the elongation parameters confirm the impression given by the previous angular distributions that there does exist some collimation of the secondary particles along the x-axis, the axis of the colliding primaries in the overall centre of mass system.

Correlation Effects

The correlation effects between the transverse momenta of pairs of particles were investigated in the manner suggested by Bertocchi and Zalewski (1966). For each event the particles were arranged in order of the magnitude of their longitudinal momentum and then distributions of the angle φ_{ik} between the transverse momenta P_{Ti} of the particles were plotted with φ_{ik} defined by

$$\cos \varphi_{ik} = \frac{(P_{Ti} \cdot P_{Tk})}{P_{Ti} \cdot P_{Tk}}$$

Of the fifteen distributions obtained the largest differences from pure phase space prediction were found in the distributions of φ_{16} and φ_{25} which are illustrated in Fig. 37(a) and (b). The differences, however, do not appear to be statistically significant.

Significant deviations from the statistical model were found, however, in the distributions of the centre of mass angles between pairs of pions. This phenomenon corresponds to

Fig 37

4c. EVENTS : HISTOGRAM OF DISTRIBUTIONS OF ϕ · ANGLES

(a) HISTOGRAM OF ϕ 16.

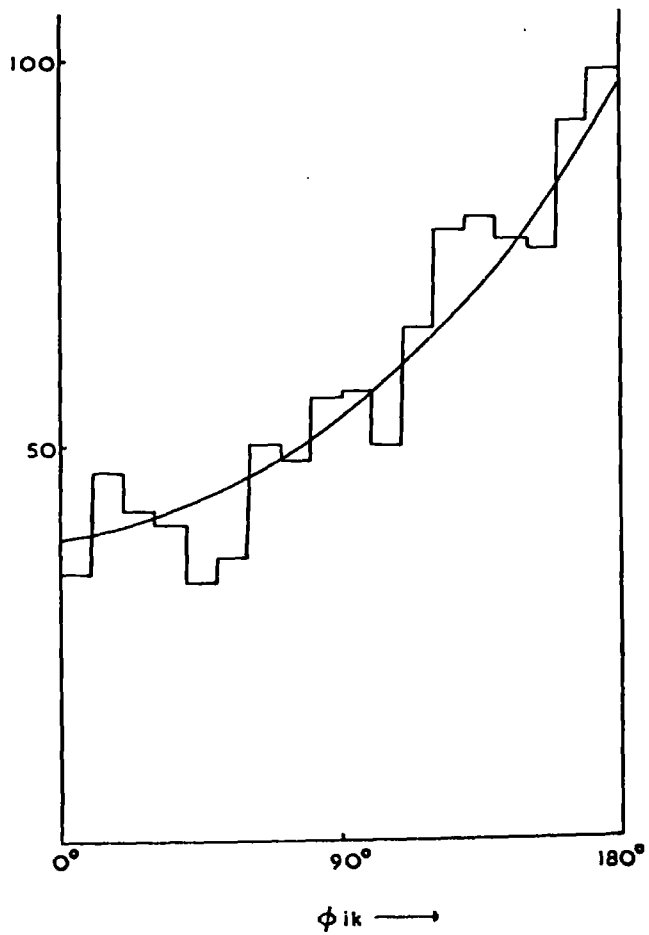

(b) HISTOGRAM OF ϕ 25.

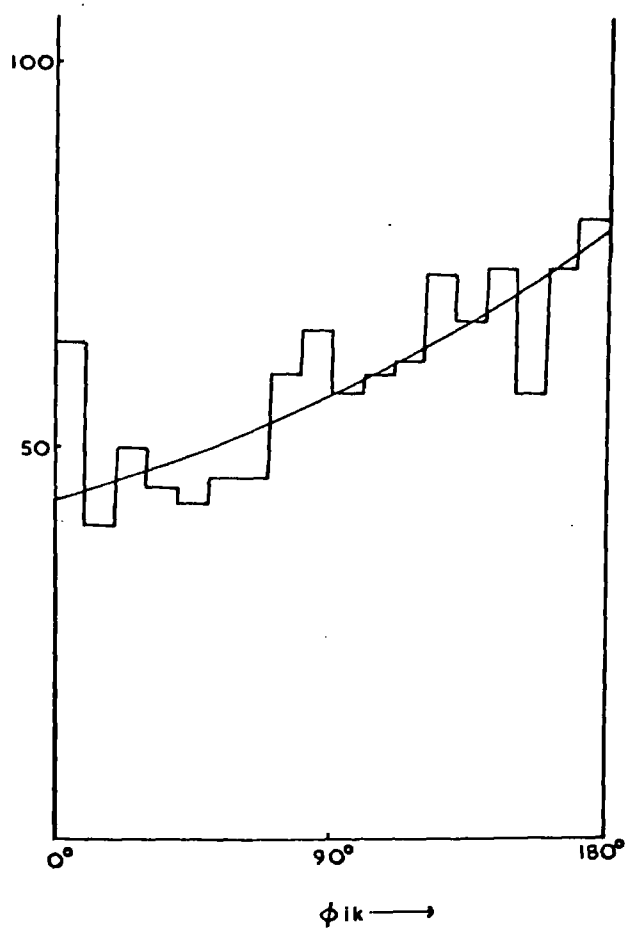

similar effects observed for high multiplicity interactions by Goldhaber et al. (1960) in $\bar{p}p$ annihilations and Bartke et al. (1966) in 8 GeV/c $\pi^+ p$ interactions.

It was found that the distributions of, cos θ the cosines of the angles between pairs of pions $(\pi^+\pi^+)(\pi^-\pi^-)$ and $(\pi^+\pi^-)$ as illustrated in Fig. 38 (a), (b) and (c), show large deviations from the statistical model curve. The values of the forward-backward ratio γ for these distributions are given in Table 7 below.

Table 7

Ac Events:

Forward-Backward Ratio, γ , for Di-pion Combinations

Particle combination	γ = B/F
$\pi^+\pi^+$	1.19 ± 0.02
$\pi^+\pi^-$	1.71 ± 0.01
$\pi^-\pi^-$	0.99 ± 0.02

When these values are compared with the value of $\gamma = 1.40$ for pure statistical production it may be seen that although the assymetry is more pronounced for pairs of particles with opposite charges, significant effects are still observed for pairs of pions of like charge.

Further investigations were made in to the distributions for the particle combinations to discover whether these

Fig. 38

4C EVENTS: DISTRIBUTION OF COSINE OF ANGLE BETWEEN PION PAIRS

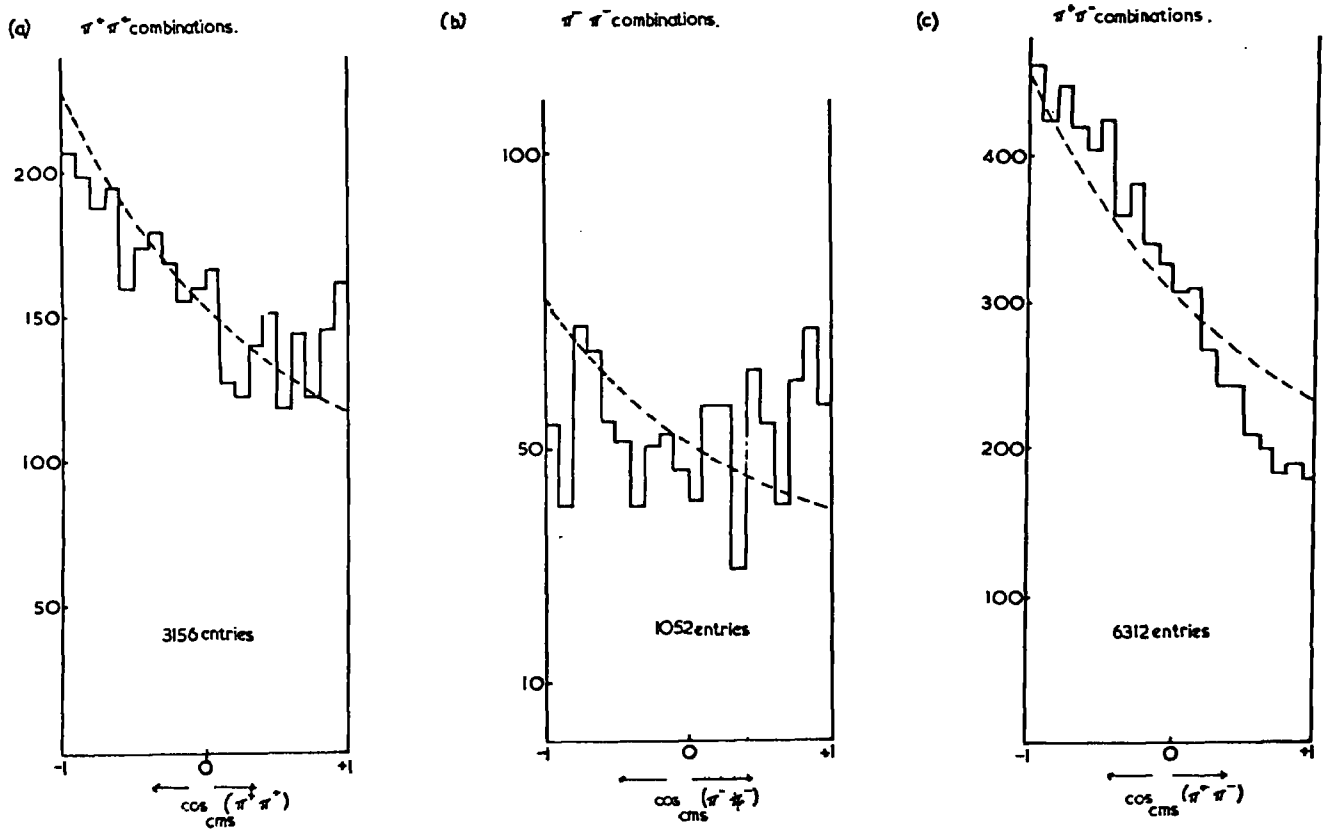

observed assymetries are a natural consequence of some production mechanism for the resonances found in this channel.

Dynamics of Resonance Production

The angular distribution of neutral di-pions in the centre of mass system, illustrated in Fig. 39, shows a marked assymetry which becomes more apparent for these particle combinations lying within the ρ mass region; ($0.67 \leq M_{\pi^+\pi^-} \leq 0.85$) shown in Fig. 40(a). Similar control distributions were plotted for $\pi^+\pi^+$ and $\pi^-\pi^-$ combinations. Fig.40(b) and (c) and the assymetry parameters are summarised in Table 8 below:

Table 8

4c Events:

Assymetry parameters, R, for di-pions in ρ mass region

Particle combination	R = (F - B)/(F + B)
$\pi^+\pi^-$	0.19 ± 0.03
$\pi^-\pi^-$	0.18 ± 0.07
$\pi^+\pi^+$	0.17 ± 0.04

There is no significant difference between the values obtained for the three different combinations and the only distinguishing feature is that the peaking at the higher values of $\cos \theta^*$ is more pronounced in the case of the neutral di-pions.

FIG 39

4c EVENTS : ANGULAR DISTRIBUTION OF NEUTRAL DI-PION COMBINATIONS

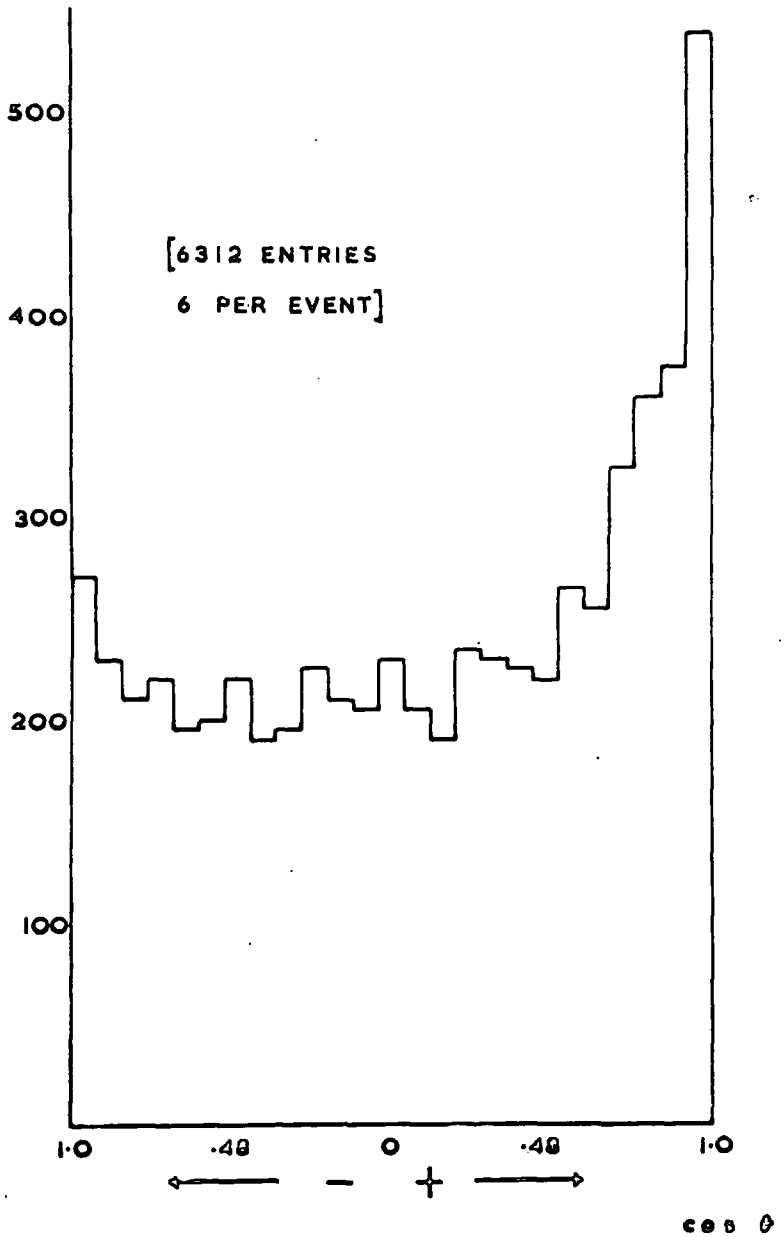

Fig. 40

Angular Distribution of Di-Pion Combinations in ρ^0 Mass Region.

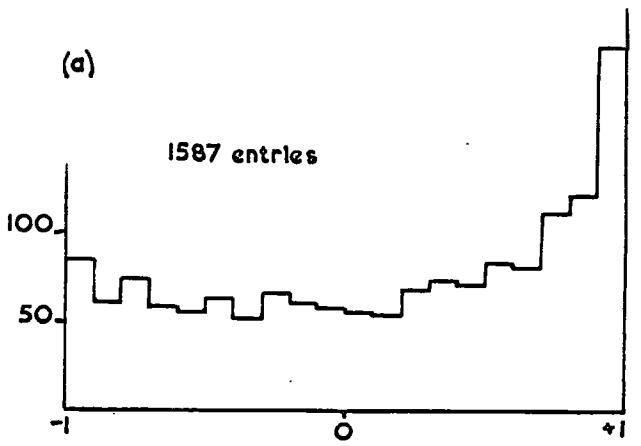

cos cms $(\pi^+\pi^-)$
if $M(\pi^+\pi^-)$ between
0.67 and 0.85 Gev.

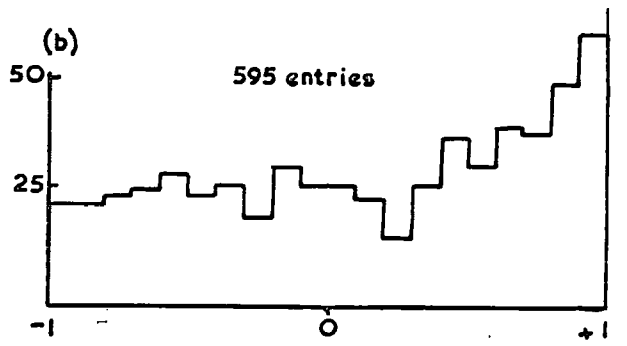

cos cms $(\pi^+\pi^+)$
if $M(\pi^+\pi^+)$ between
0.67 and 0.85 Gev.

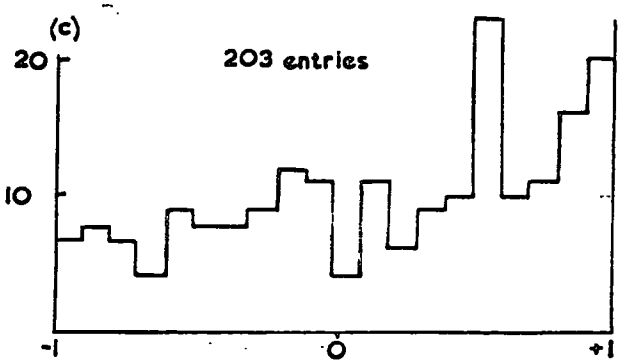

cos cms $(\pi^-\pi^-)$
if $M(\pi^-\pi^-)$ between
0.67 and 0.85 Gev.

The corresponding distributions for the combinations of a proton and one pion, Fig. 41, exhibit a similar effect with very little difference between the two assymetry parameters given in Table 9 below:

Table 9

4c Events:

Assymetry parameter, R, for the combinations of the proton and a pion

Particle Combination	$R = (F - B)/(F + B)$
$\pi^+ p$	-0.37 ± 0.03
$\pi^- p$	-0.32 ± 0.03

These values are of the same order as the assymetry parameter of the proton (Table 5) although the same feature observed with the di-pion distributions is present here viz. that the backward peaking for the resonance combination is more pronounced.

The longitudinal velocity of the backward-going protons has been shown to be larger than that expected from statistical production. That this effect may be attributed to an enhanced velocity for the N^* resonance is seen in Fig. 42 where the normalized velocity, β^*, of the $\pi^+ p$ combinations is plotted. There is a broad excess in the region of high β^*.

Fig 41

Angular Distribution of combinations of a Proton and a Pion in $N^{\circ}_{3/2}$ Mass Region.

(a) $\cos \theta^{a}$ $(P\pi^{+})$

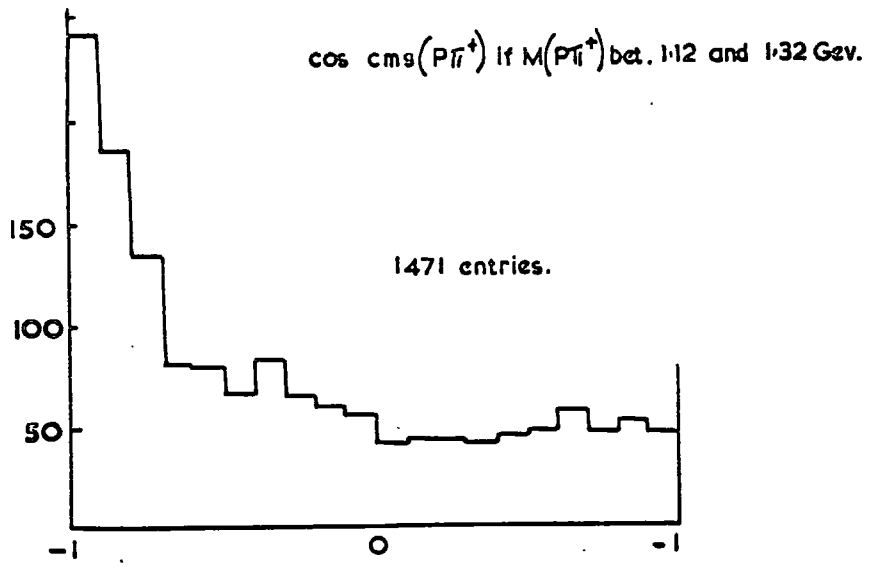

(b) $\cos \theta^{*}(P\pi^{-})$

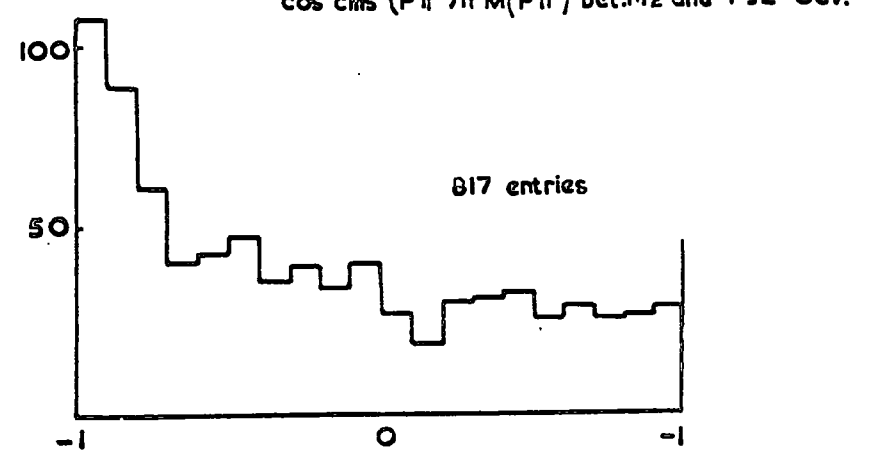

Fig. 42

4c EVENTS : HISTOGRAM OF $\beta^*(\pi + P)$

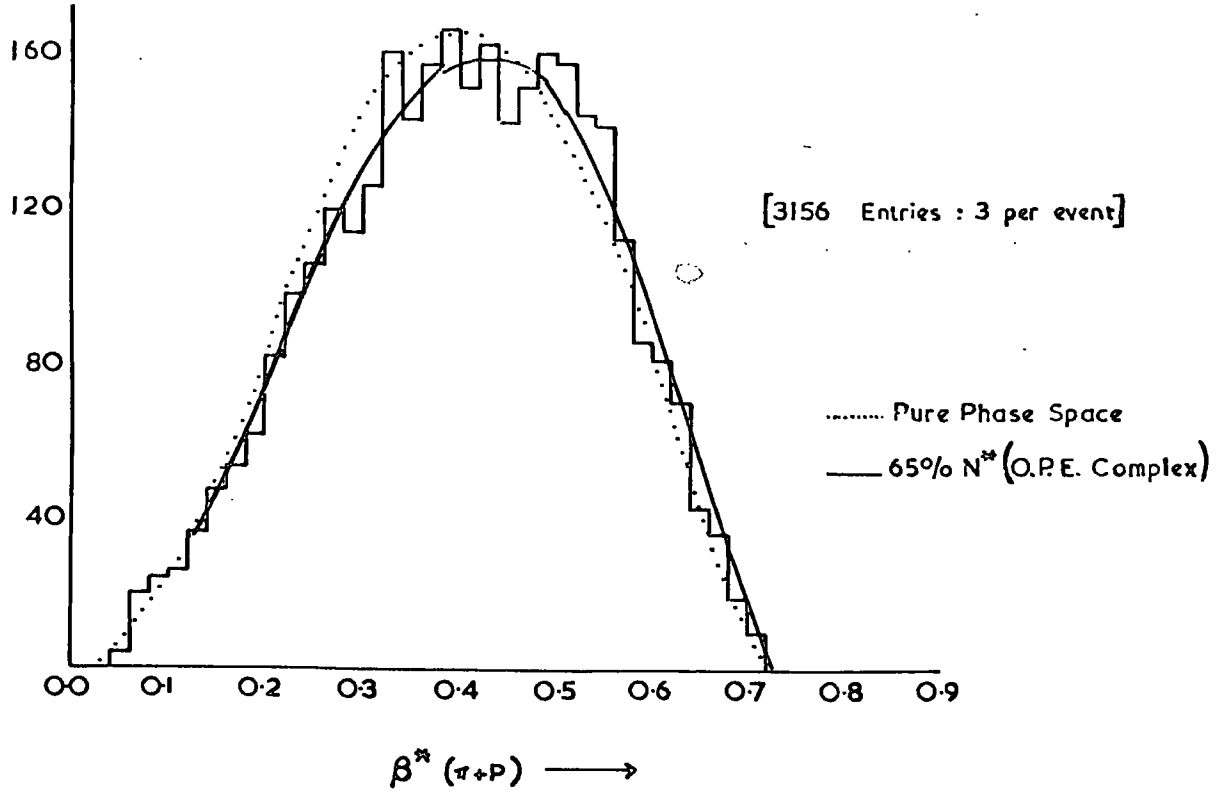

Although the apparent paucity of the isobars with high velocity may be interpreted in terms of secondary collisions and scatterings within the interaction volume the directional properties of backward-going N^{*} and forward-going ρ must be dependent upon some non-statistical mechanism dominating the production of the resonances. The required mechanism has similar effects to the peripheral production of resonances in low multiplicity interactions and consequently investigations were carried out in to the four momentum transfers to the $\pi^{+}p$ and $\pi^{+}\pi^{-}$ combinations from the primary particles.

Peripheral Production Model

The overall distributions of Δ^2, the four-momentum transfer from the incident proton to the $\pi^{+}p$ combination and the Δ^2 from the primary pion to the neutral di-pion combinations are shown in Figs. 43 and 44. In both histograms there are large deviations from the pure phase space curves with large enchancements in the regions of low Δ^2.

To test the hypothesis of peripheral production, Monte-Carlo calculations were made to simulate the N^{*} and ρ^{o} production using a one pion exchange mechanism as described in Chapter 1. To obtain a correspondence with production distributions that had been successful with quasi two-body interactions a form factor (Goldhaber 1964) was used viz.

$$F(t) = (a^2 + m_p^2)/(a^2 + t)$$

Fig. 43

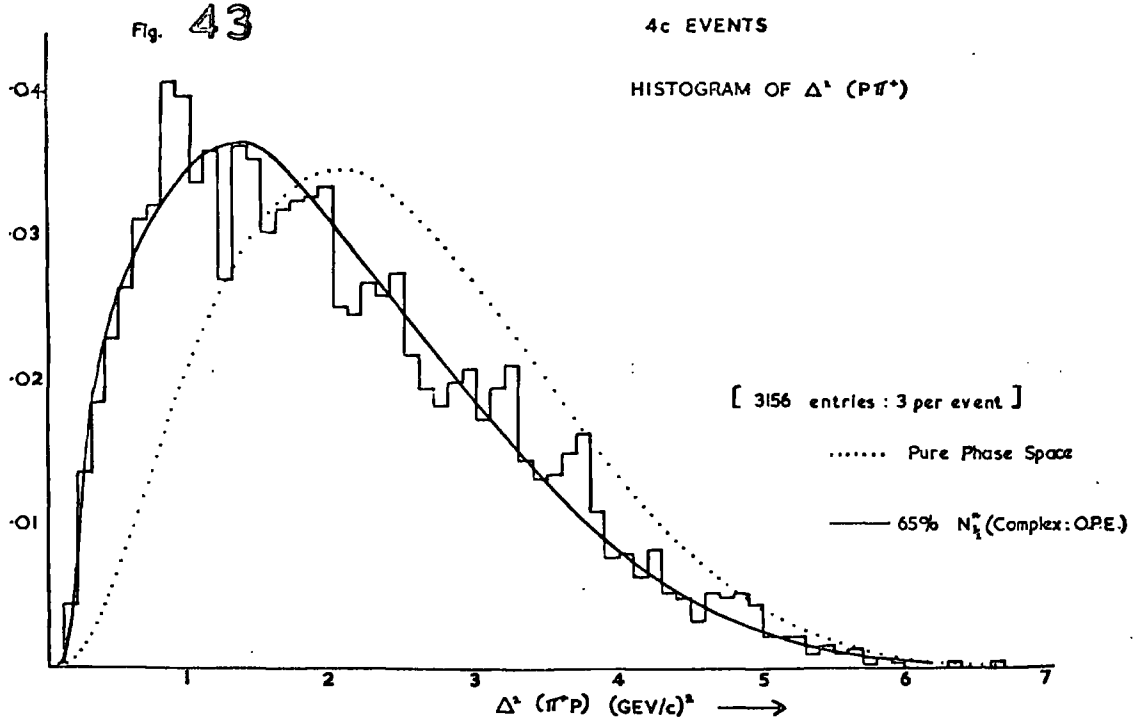
4c EVENTS
HISTOGRAM OF Δ² (Pπ⁺)
·04
·03
·02
·01
1
2
3
4
5
6
7
Δ² (π⁺P) (GEV/c)² ⟶
[3156 entries : 3 per event]
····· Pure Phase Space
—— 65% N*₁₁₃₅ (Complex : O.P.E.)

Fig. 44

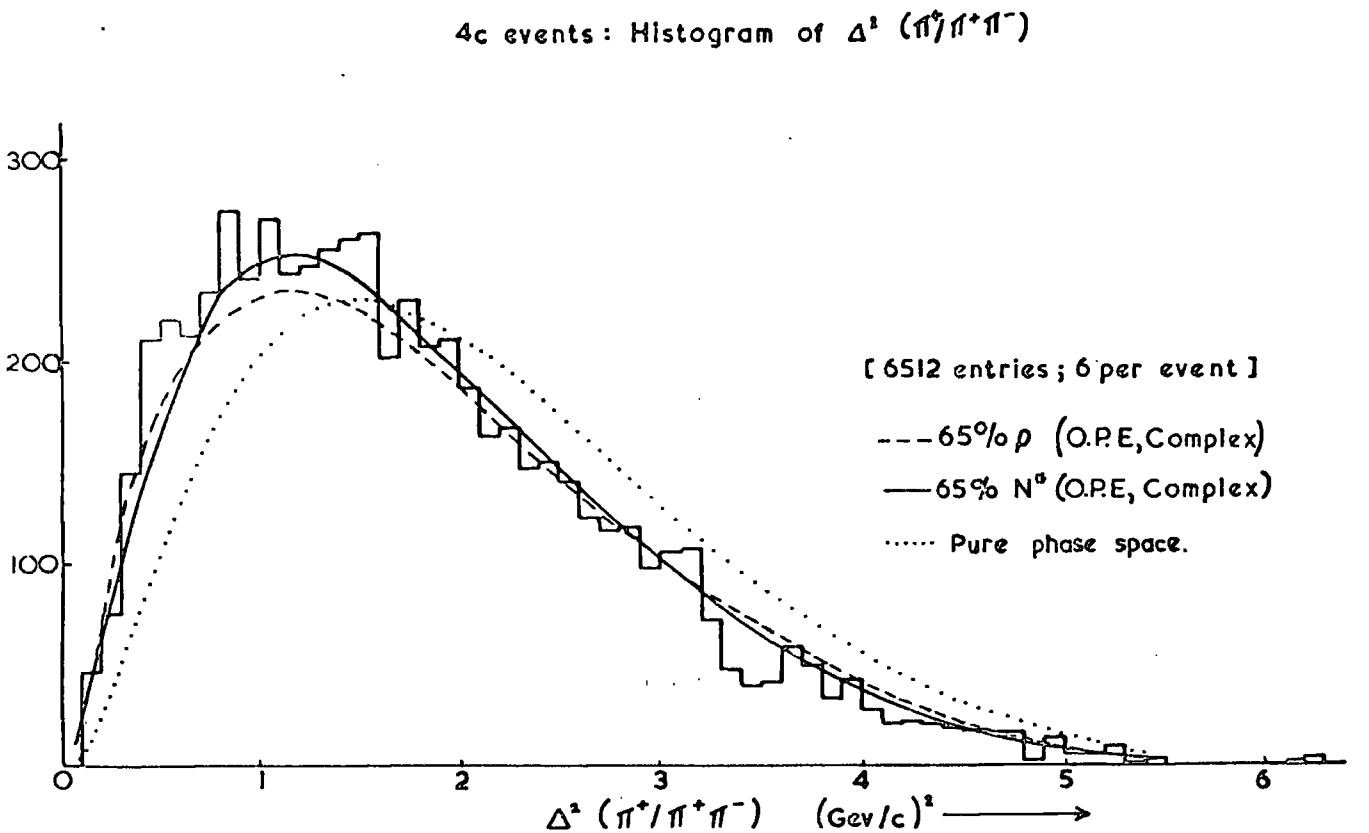
4c events : Histogram of Δ^2 $(\pi^+/\pi^+\pi^-)$
300
200
100
0
1
2
3
4
5
6
[6512 entries ; 6 per event]
---65% ρ (O.P.E, Complex)
——65% N* (O.P.E, Complex)
····· Pure phase space.
Δ^2 $(\pi^+/\pi^+\pi^-)$ $(Gev/c)^2$ ⟶

where

$$a^2 = 0.132 \text{ GeV}^2/c^2$$

The interactions were envisaged as being of a multi-peripheral type and the baryonic and mesonic vertices were considered separately. The production of a resonance at one vertex was accompanied by a "c" particle at the other with the c particle considered as a statistical state with no internal dynamics except that of having the appropriate quantum numbers for the exchange of a pion.

With a six particle final state, therefore, the normal Δ^2 distribution, $d\sigma/dt$, is modified by the five particle phase, $d\phi_5$, appropriate to the reactions

$$\pi^+ \; p \rightarrow N^* \; c^o \qquad c^o \rightarrow \pi^+\pi^+\pi^-\pi^-$$

or

$$\pi^+ \; p \rightarrow \rho^o \; c' \qquad c' \rightarrow \pi^+\pi^+\pi^-$$

so that

$$d\sigma_N/dt = \text{const.} \; |T|^2 \; . \; d\phi_5$$

The curves obtained for the contributions of N^* and determined from the mass plots are shown on the appropriate distributions of Δ^2. The agreement with the experimental histograms is much improved and also in the momentum distributions of the individual particles, the observed trends are well simulated (Figs. 34, 35 and 36).

It has been found, however, that the Δ^2 distribution for one vertex is not independent of the production process on the other vertex. Furthermore, the extrapolation of the differential cross section in to the region of larger momenta transfers may not be valid. The technique described therefore has no rigorous application but can only serve as an indication for subsequent theoretical analysis of high multiplicity events. Although the exact formulation of the differential production cross-section for these high multiplicity interaction is not known it is indeed likely that it exhibits a preference for low four-momentum transfers in a similar manner to the low multiplicity interactions.

Angular Decay Schemes

The distributions of the decay angles of the resonances were also examined in order to detect characteristic distributions that would indicate the existence and nature of any exchange particles. The angles investigated were θ which is defined in section 1.1. and θ_h the angle between the direction of the outgoing π^+ and the direction of motion of the resonance in the rest system of the resonance. For an exchange mechanism such as that described previously where there are more than two particles emitted from the top vertex (c.f. Fig. 2) no unique definition of the angle ϕ is possible.

The only distribution found to exhibit a significant

difference from isotropy was that of cos ϑ_h for the $\pi^+\pi^-$ combinations. In this distribution Fig. 45 a marked $\cos^2 \vartheta_h$ dependence is observed which is enhanced by restricting the sample to those $\pi^+\pi^-$ combinations which have at least one of the π^+p combinations containing the remaining positive pions, lying within the N^{*} mass region. The application of this condition increased the probability of the χ^2 for the fit to 80%.

This phenomenon would suggest that there is a large measure of spin alignment of the ρ^0 mesons and that the associated production of an isobar is related to this property.

The equivalent distributions for the neighbouring $\pi^+\pi^-$ mass regions were also calculated and found to be consistent with isotropy: Fig. 46(a) as was the distribution for $\pi^+\pi^+$ and $\pi^-\pi^-$ combination Fig. 46(c).

Fig. 4 5

$\cos \Theta_H (\pi^+\pi^-)$

if $M(\pi^+\pi^-)$ between 0.67 and 0.85 Gev

$u(\pi^+\pi^-) > 3$ Gev^2

403 entries

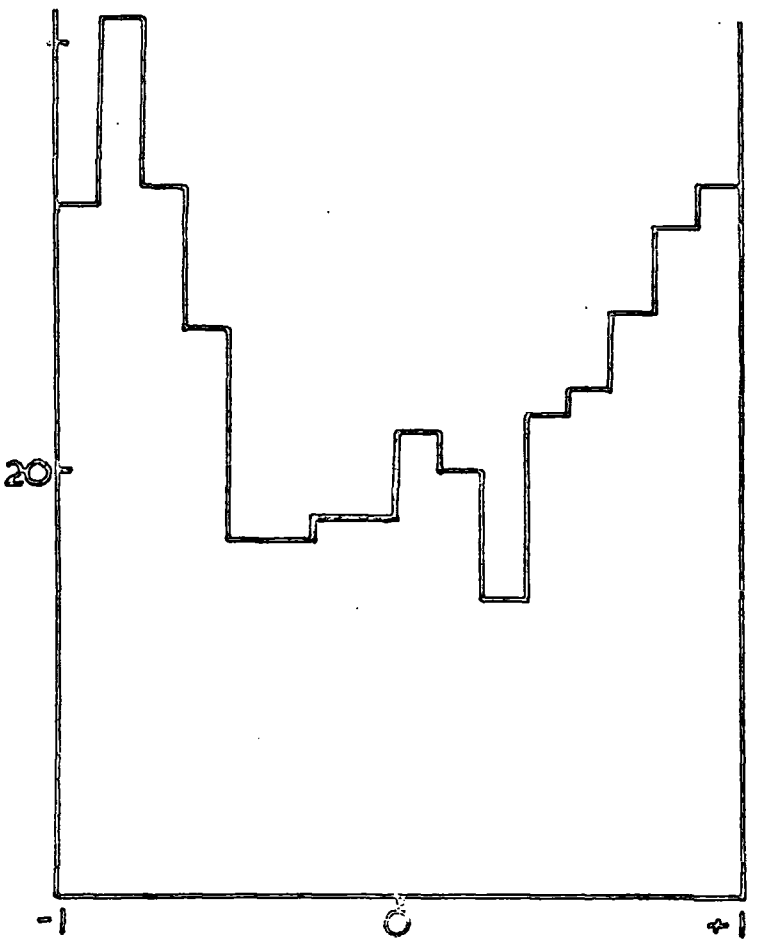

Fig. 46

(a)

Cos $\theta_H(\pi^+\pi^-)$

Cos $\theta_H(\pi^+\pi^-)$

If $M(\pi^+\pi^-)$ between 0.49 and 0.67

or 0.85 and 7.03 Gev

$u(\pi^+\pi^-) > 3$ Gev and $M(P\pi^{+\prime})$ bet.

1.12 and 1.32 Gev, $\pi^+ \neq \pi^{+\prime}$

$\chi^2 = 22$

$a = .94 \pm .07$

$P(\chi^2) = 10\%$

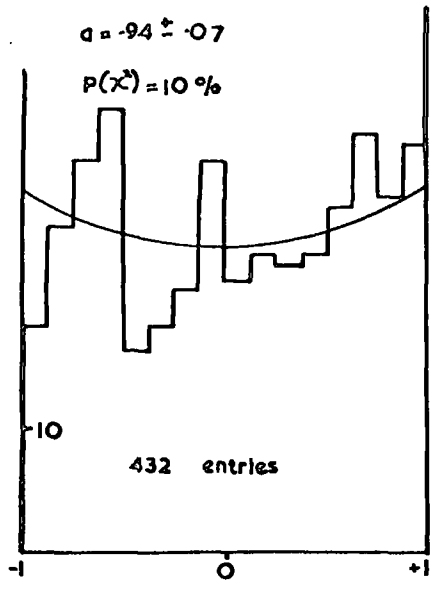

432 entries

(b)

Cos $\theta_H(\pi^+\pi^-)$

Cos $\theta_H(\pi^+\pi^-)$

If $M(\pi^+\pi^-)$ between 0.67 and 0.85 Gev

$u(\pi^+\pi^-) > 3$ Gev and $M(P\pi^{+\prime})$ bet.

1.12 and 1.32 Gev, $\pi^+ \neq \pi^{+\prime}$

$\chi^2 = 8$

$a = .69 \pm .06$

$b = .93 \pm .19$

$P(\chi^2) = 80\%$

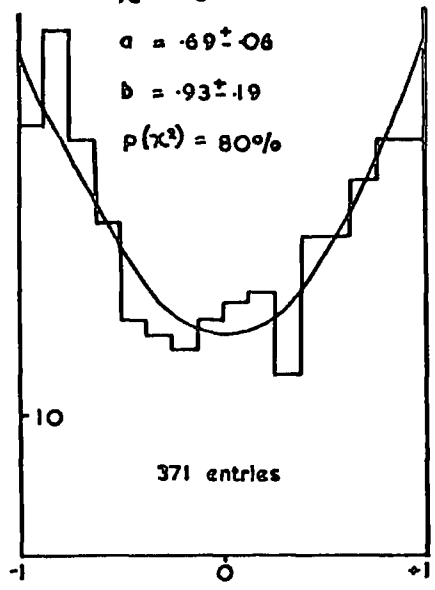

371 entries

(c)

Cos $\theta_H(\pi^+\pi^+)$ and

Cos $\theta_H(\pi^-\pi^-)$

If $M(\pi^+\pi^+)$ $M(\pi^-\pi^-)$ between

.67 and .85 Gev

$u(\pi^+\pi^-) > 3$ Gev and $(M\ P\pi^{+\prime})$ bet.

1.12 and 1.32 Gev, $\pi^+ \neq \pi^{+\prime}$

$\chi^2 = 26$

$a = 1.10 \pm .19$

$b = -.29 \pm .43$

$P(\chi^2) = 4\%$

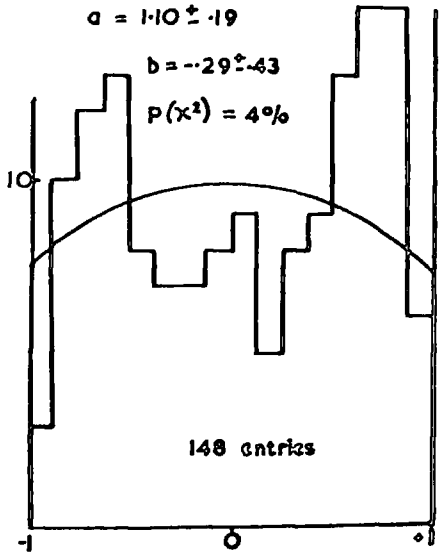

148 entries

4.4 Resonance Production in the 1c(π^0) Channel

Many of the physical effects that have been observed in the 4c channel are also found to occur in the sample of 1595 events available in the 1c(π^0) channel, and consequently the results were analysed in a similar manner. A comprehensive survey of all the possible distributions of effective masses of particle combinations was made.

Apart from the $N^*(1236)$ and the ω^0 (783), the only other resonance that could be resolved was the $X^0(959)$ of which a small number of examples was found. Some of these X^0 particles were found to be produced peripherally with an $N^*_{3/2}$ isobar to give the only evidence of quasi-two body production discovered in the six-pronged events.

The Two Particle Effective Mass Spectra

The effective mass spectra of the combinations of the proton and a positive pion is illustrated in Fig. 47 and exhibits a large enhancement in the mass region of the N^*. The central value of this peak is shifted downwards by some 30 MeV.

The corresponding $T_3 = -\frac{1}{2}$ and $+\frac{1}{2}$ states are absent from the π^-p and π^0p effective mass distributions illustrated in Figs. 48 and 49. Because of the distortion of the peak the fit to the π^+p distribution was made by varying the admixture of seven-body pure phase space and six-body phase space containing an $N^*_{3/2}$ particle whose mass distribution is described by the function

FIG 47

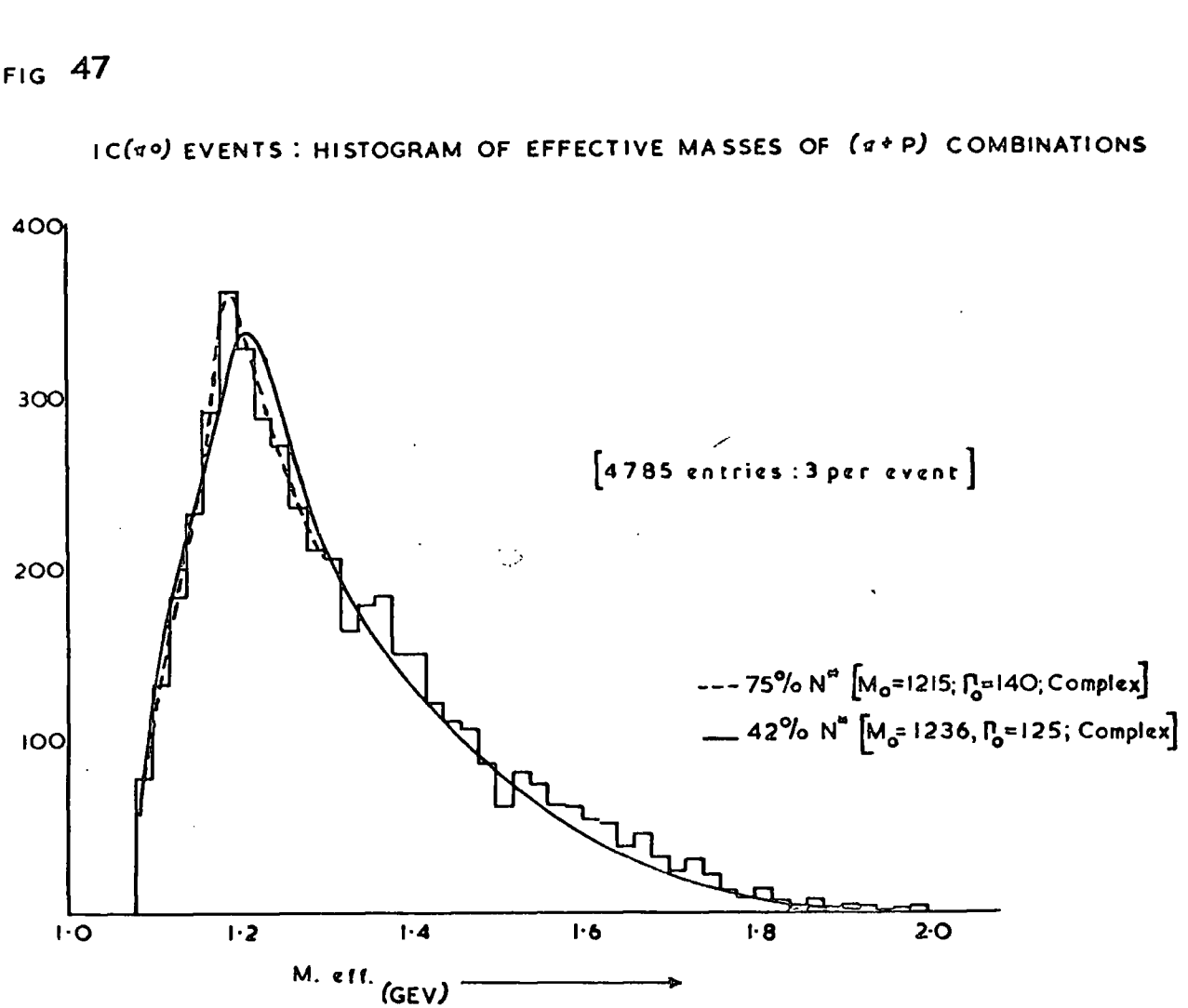
1C(π⁰) EVENTS : HISTOGRAM OF EFFECTIVE MASSES OF (π⁺P) COMBINATIONS
400
300
200
100
[4785 entries : 3 per event]
--- 75% N* [M₀=1215; Γ₀=140; Complex]
— 42% N* [M₀= 1236, Γ₀=125; Complex]
1·0
1·2
1·4
1·6
1·8
2·0
M. eff. (GEV)

FIG. 48

Ic (π⁰) events.

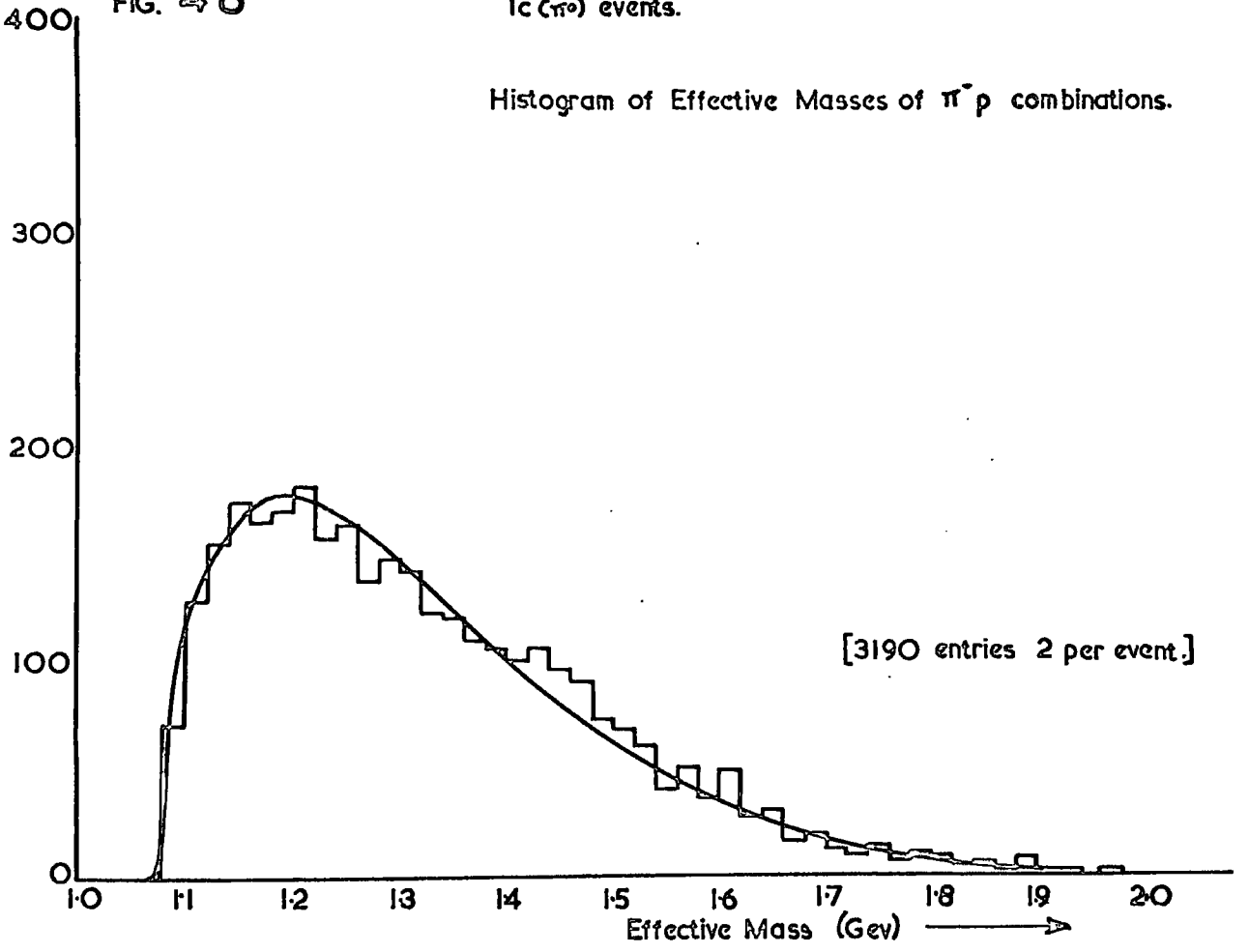

FIG. 49

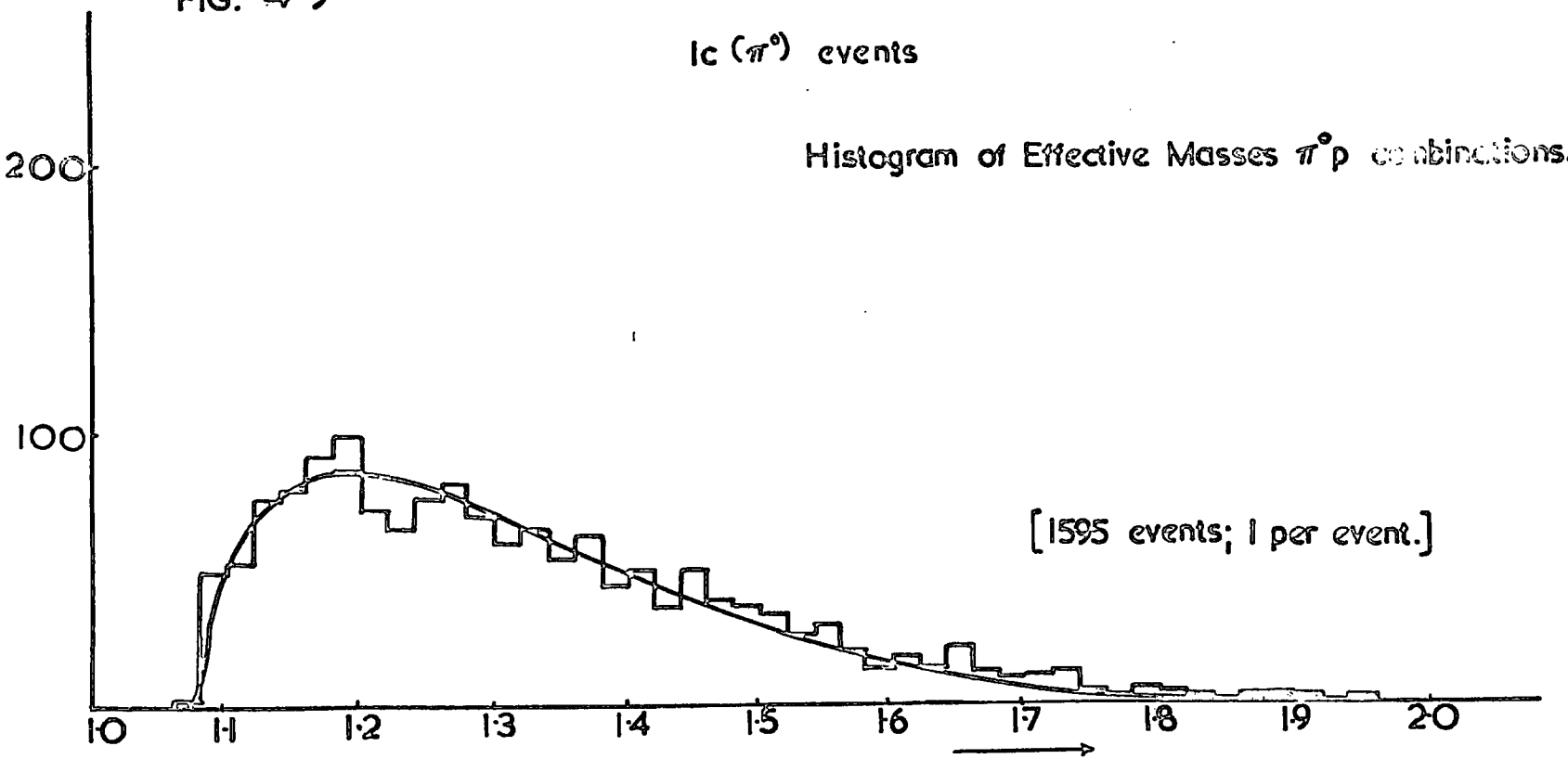
Ic (π^0) events
Histogram of Effective Masses π^0p combinations.
200
100
[1595 events; 1 per event.]
1·0
1·1
1·2
1·3
1·4
1·5
1·6
1·7
1·8
1·9
2·0

given in Section 4.4. The best fit to the overall spectrum corresponded to only 35 ± 6 of Δ^{++} with a low probability of fitting of only some 10^{-4}., which was attributed to a large deviation of the background from the pure phase space curve the estimate of isobar production was increased in a fit performed over the restricted mass region of the resonance viz. ($1320 \geq M_{p\pi^+} \geq 1120$) to 44 ± 6. but the probability of this fit rose to only 0.03 .

Thus it would appear that the description of the shape of the $N^*_{3/2}$ peak was not sufficiently accurate to allow fitting to take place. It was therefore necessary to vary the parameters of the central mass value m_o, and the width in the Breit-Wigner function, Γ_o. Furthermore the normalization condition was relaxed to allow for the inclusion of an unknown distribution of the distortion of the background in the area away from the resonance. The best value obtained for the fit was with m_o = 1215 MeV, Γ_o = 140 MeV and corresponded to a much larger Δ^{++} contribution of some 75 ± 7%. The probability of this fit $P(\chi^2 > \chi^2$ fitted) was 0.95.

The distortion of the background, is also evident in the $\pi^- p$ spectrum but no such distinction is possible in the histogram of the $\pi^0 p$ combinations where the number of entries is much smaller.

The distributions of the effective masses of the neutral and charged di-pions, Fig. 50, exhibit no peaking in the mass regions of either the ρ^o, the f^o or the $f^{o\prime}$.

The Three-particle Mass Spectra

The histograms of the effective masses of neutral tri-pion combinations is illustrated in Fig. 51. There are two peaks visible in this distribution; a large enhancement in the ω^o region and a smaller shoulder in the mass region of the η meson. The apparent width of the peak due to the ω^o meson is much larger than that expected from the decay of such a long-lived particle. This effect has been attributed to the dominance of experimental error in the estimation of the effective masses and consequently the fit to this distribution was made with a Gaussian function instead of the normal Breit-Wigner. As is explained later in this section, there was found in the $\pi^+\pi^+\pi^-\pi^-\pi^o$ effective mass spectrum a small enhancement corresponding to the production of a few X^o events which has a $\eta\pi\pi$ decay mode. Furthermore, the other two possible neutral tri-pion combinations that may be formed from the decay products of this resonance are dynamically constrained to fall within the a mass region $414 \leq M_{\pi^+\pi^-\eta} \leq 680$ which contains the η^o band. Therefore the fit carried out to estimate the contribution of ω^o particles was performed with a reduced sample of events with those events containing an X^o particle excluded. The best fit obtained

FIG. 50

1C.(π^0) EVENTS: HISTOGRAM OF EFFECTIVE MASS OF DI-PION COMBINATIONS.

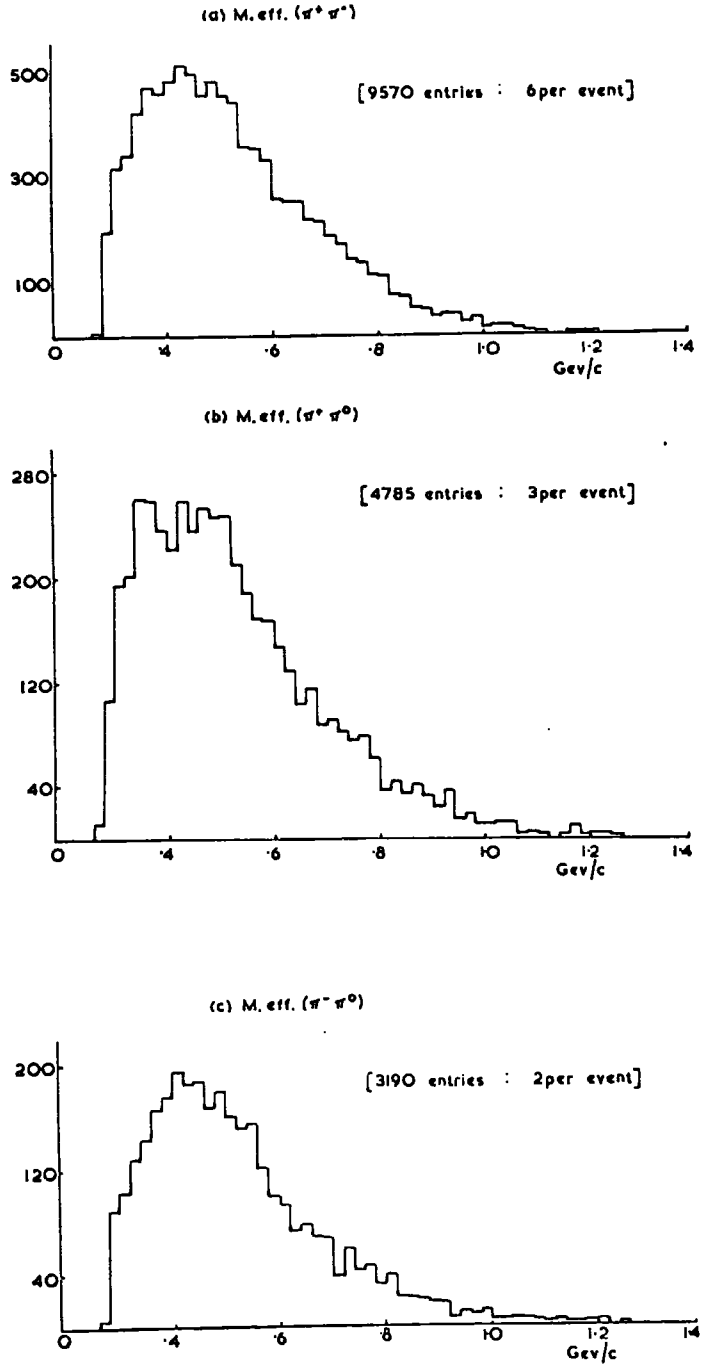

corresponded to a production of ω^o resonances in $40 \pm 5\%$ of all events although the contribution of η^o particles in the reduced sample was not statistically significant.

A further independent method was used to confirm the estimate of ω^o production viz. the investigation of the density of entries in the Dalitz plot of the π^+, π^- and π^o particles. Unlike the uniform density distribution expected for non-resonant combinations, for the decay of a 1^- particle such as the ω^o, the matrix element of the decay causes a centrally symmetric distortion of the density of points which is peaked at the centre.

The radius of each neutral tri-pion combination was computed by using a special CHARM subroutine of SUMX. The histogram subsequently obtained for all the events in the 1c(π^o) channel was compared with the pure phase space distributions generated with FOWL. The best fit to the observed excess was obtained with a production of ω^o resonances in $45 \pm 5\%$ of the events.

Higher particle resonances

A search for all the appropriate histograms of the effective masses of combinations of mesons with the proton failed to elucidate any significant enhancements due to known or unknown isobars. The proton, 2π distributions are illustrated in Fig. 52.

Fig 51

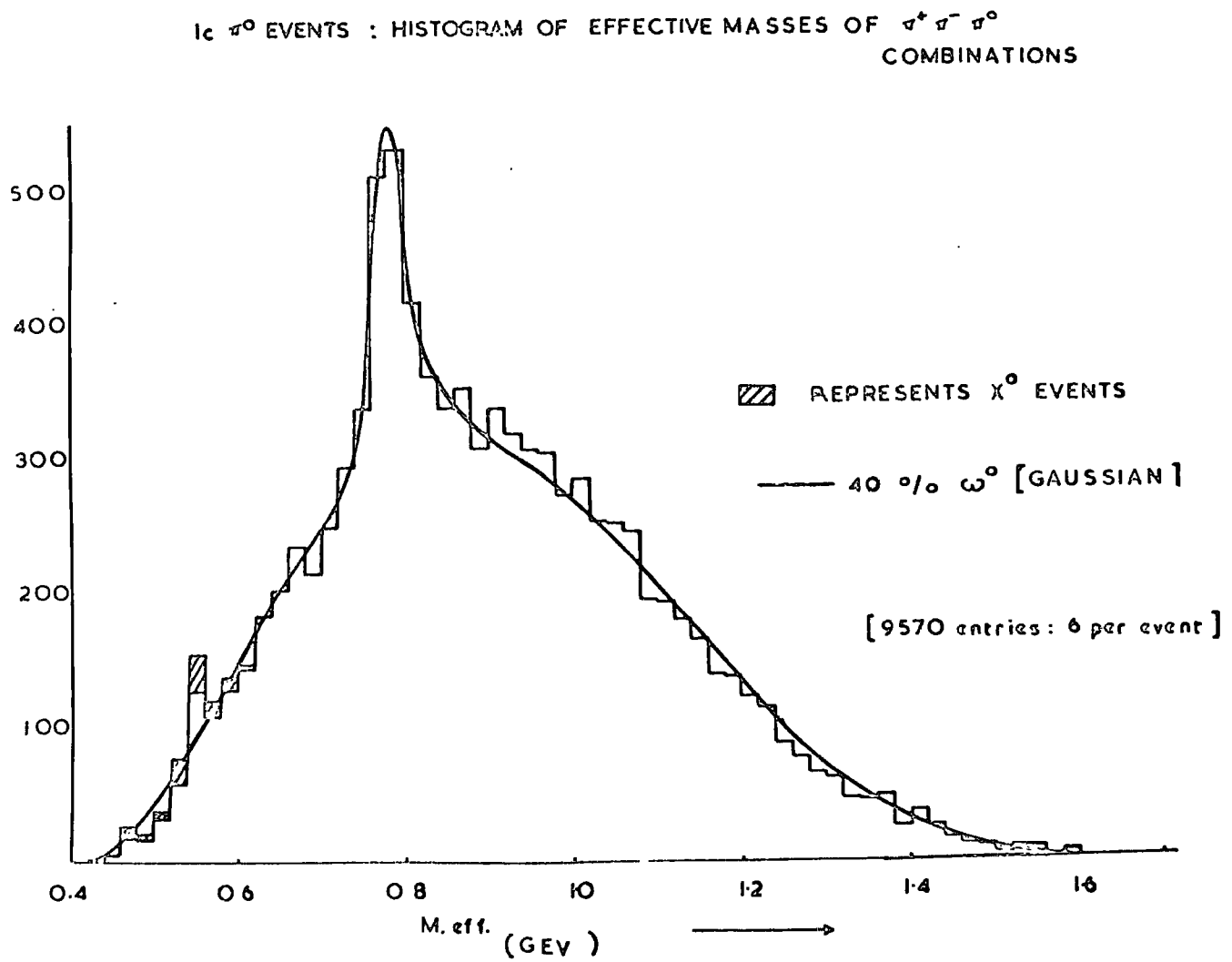
1c π^0 EVENTS : HISTOGRAM OF EFFECTIVE MASSES OF $\pi^+\pi^-\pi^0$ COMBINATIONS
500
400
300
200
100
REPRESENTS X° EVENTS
40 °/o ω° [GAUSSIAN]
[9570 entries : 6 per event]
0.4
0 6
0 8
10
1·2
1·4
1·6
M. eff. (GEV)

FIG. 52

Ic (π^0)EVENTS : HISTOGRAM OF EFFECTIVE MASSES OF COMBINATIONS OF THE PROTON AND TWO PIONS

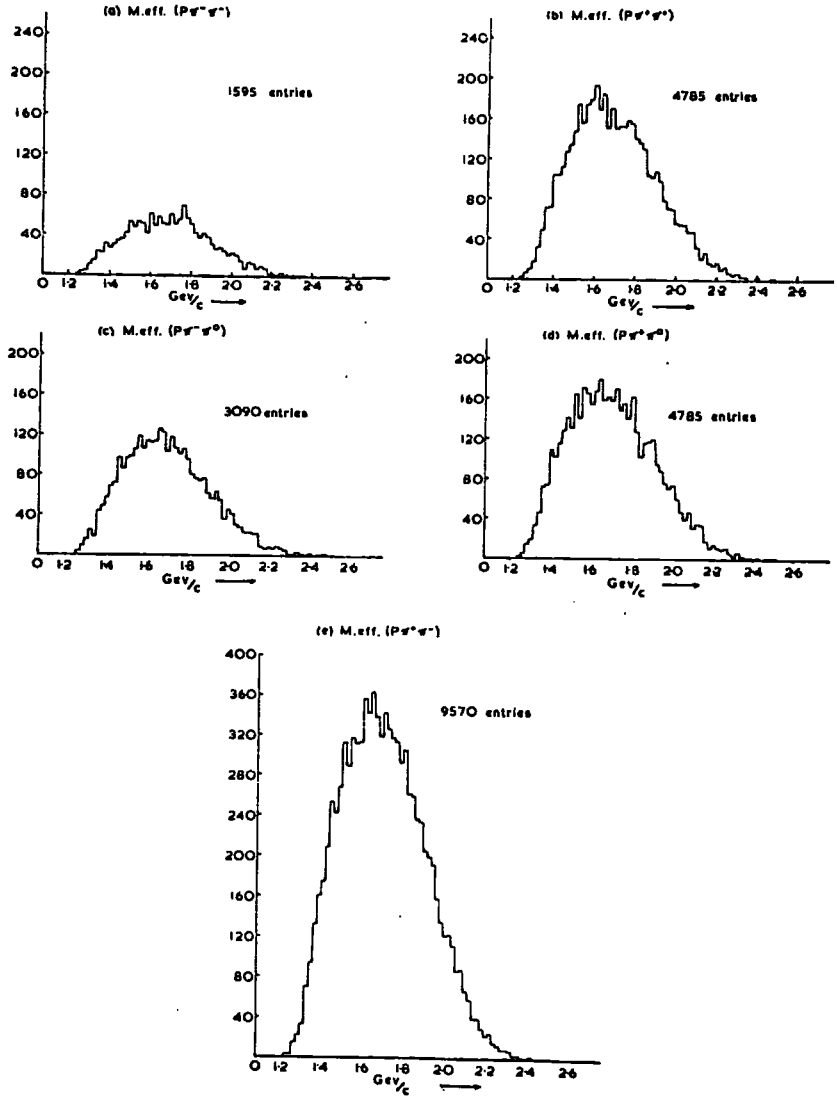

A similar phenomenon was apparent in the effective mass distributions of the mesons. No evidence was found in the $\pi^+\pi^+\pi^-\pi^0$ and $\pi^-\pi^+\pi^-\pi^0$ mass spectra, Fig. 53, for the B meson so that the copious production of the ω^0's could not be described to the decay of an $\omega\pi$ resonance.

There was, however, found some evidence for the production of X^0 (959) resonances. A small enhancement of some 17 events is observed at the leading edge of the $\pi^+\pi^+\pi^-\pi^-\pi^0$ effective mass distribution, Fig. 54, between 930 and 990 MeV where the phase space prediction for production in this mass region is only 1 ± 1 event. Of these events, 15 have at least one $\pi^+\pi^-\pi^0$ combination lying within the restricted η^0 mass region of $533 \leq M_{\pi^+\pi^-\pi^0} \leq 563$ MeV as seen in Fig. 55.

FIG. 53

1c (π^0) EVENTS · HISTOGRAM OF EFFECTIVE MASSES OF 4 PION COMBINATIONS.

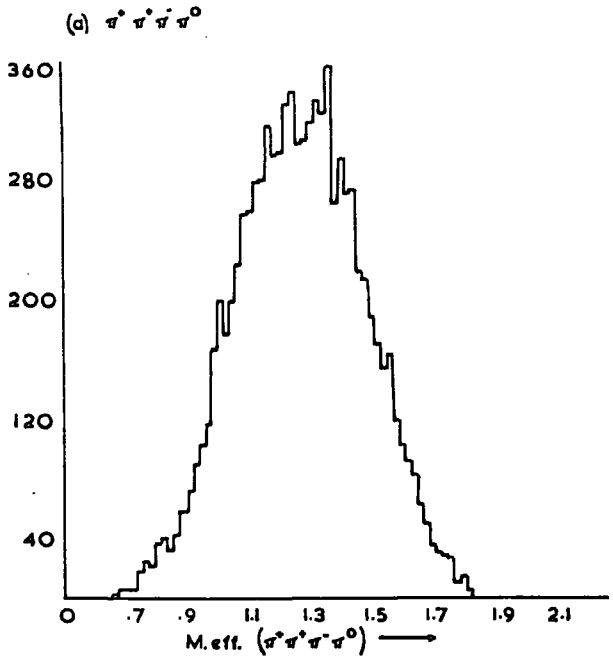

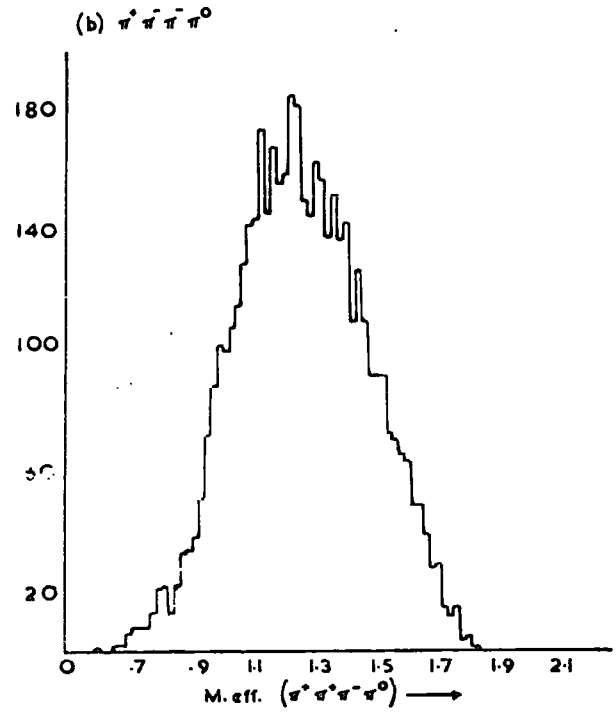

Fig. 54

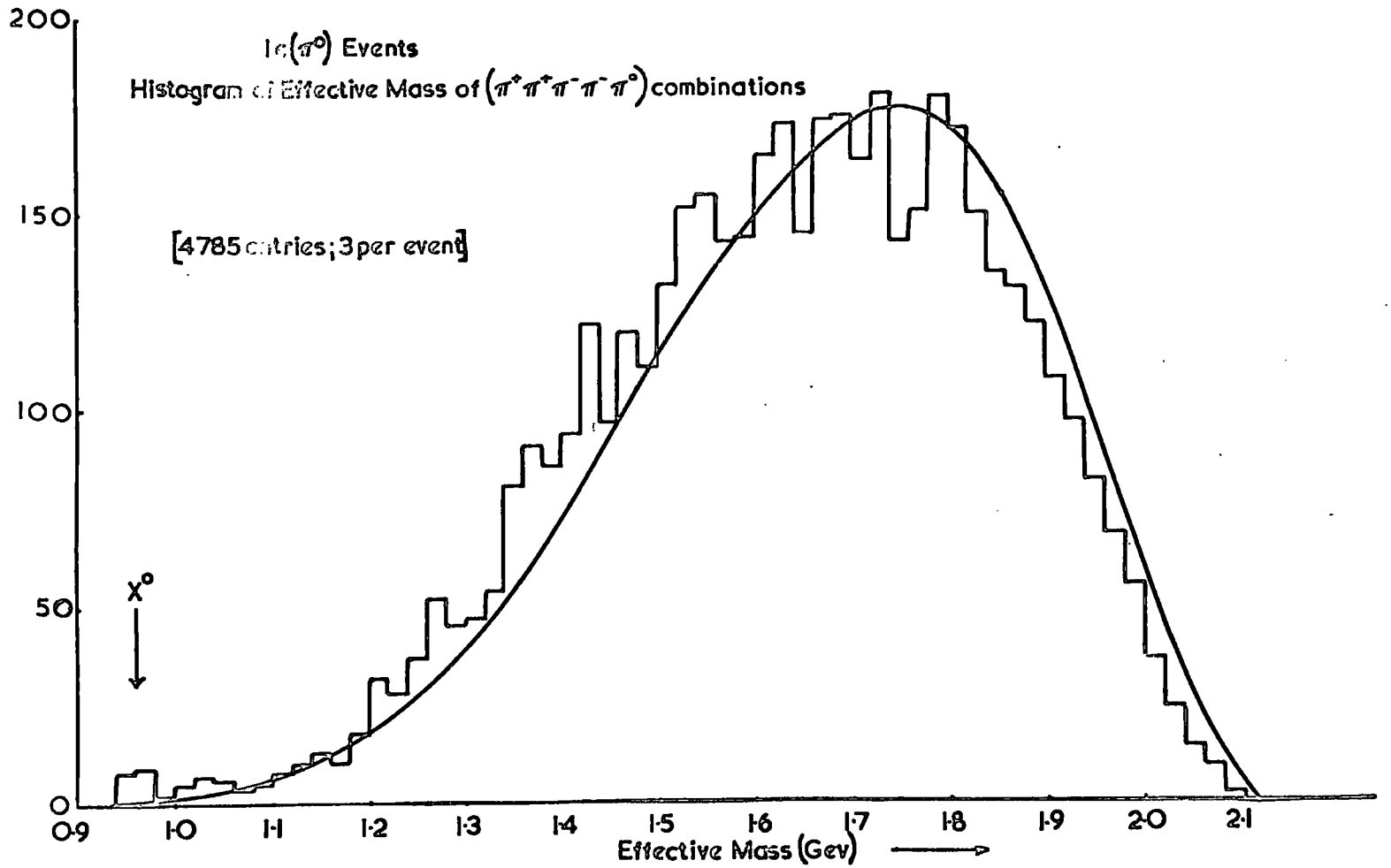
200
150
100
50
0
1c(π^0) Events
Histogram of Effective Mass of $(\pi^+\pi^+\pi^-\pi^-\pi^0)$ combinations
[4785 entries; 3 per event]
X°
0·9
1·0
1·1
1·2
1·3
1·4
1·5
1·6
1·7
1·8
1·9
2·0
2·1
Effective Mass (Gev)

Fig. 55

Ic (π^0) Events: Histogram of Effective Mass of Neutral Tri-pion Combinations from X^0 Events

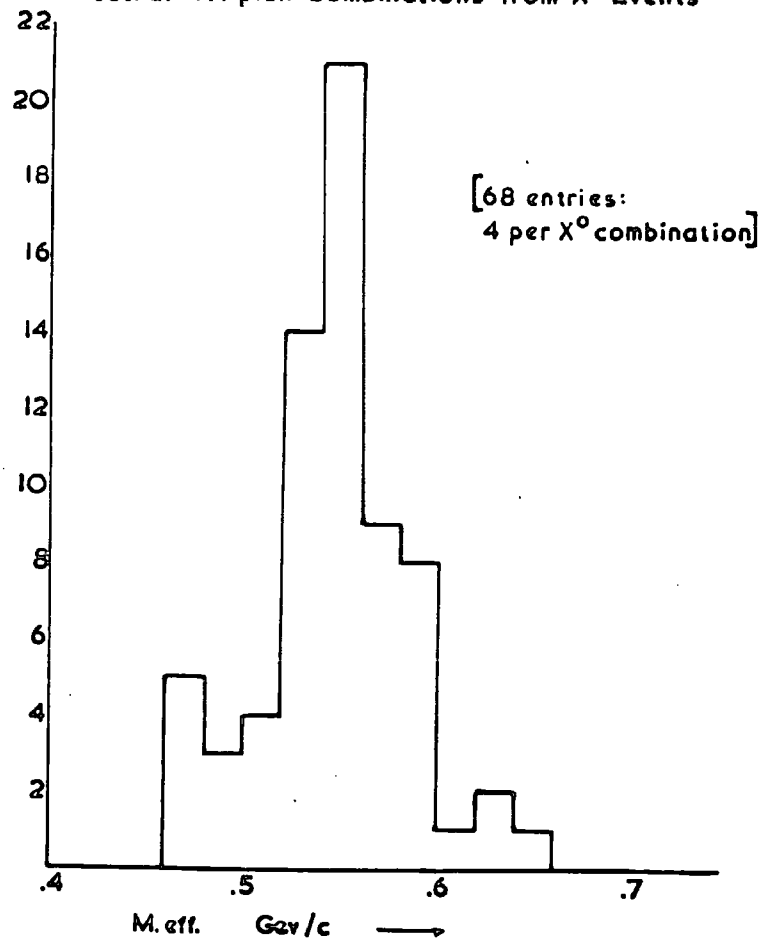

4.5 Dynamics of Resonance Production in the 1c(π^o) Channel

One particle distributions

The angular distributions of the individual particles are illustrated in Fig. 56 and the corresponding assymetry parameters are given in Table 10 below:

Table 10

1c(π^o) Events:

Assymetry Parameters, R, for the Individual Particles

Particle	R = (F-B)/(F+B)
p	-0.34 ± 0.02
π^+	0.06 ± 0.01
π^-	0.15 ± 0.02
π^o	0.19 ± 0.03

As found with the 4c events there is a significant tendency for the secondary proton to be produced in the backward direction, travelling in the same general direction in the centre of mass system as that of the incident proton. Forward peaking is observed for the negative and neutral pions which appears to be absent from the corresponding distribution for the positive pion.

The effects of assymetrical production are also visible in the distributions of the components of momentum, P_x and P_y,

FIG. 56

1c (π^0) EVENTS : ANGULAR DISTRIBUTION OF INDIVIDUAL PARTICLES IN CENTRE OF MASS SYSTEM

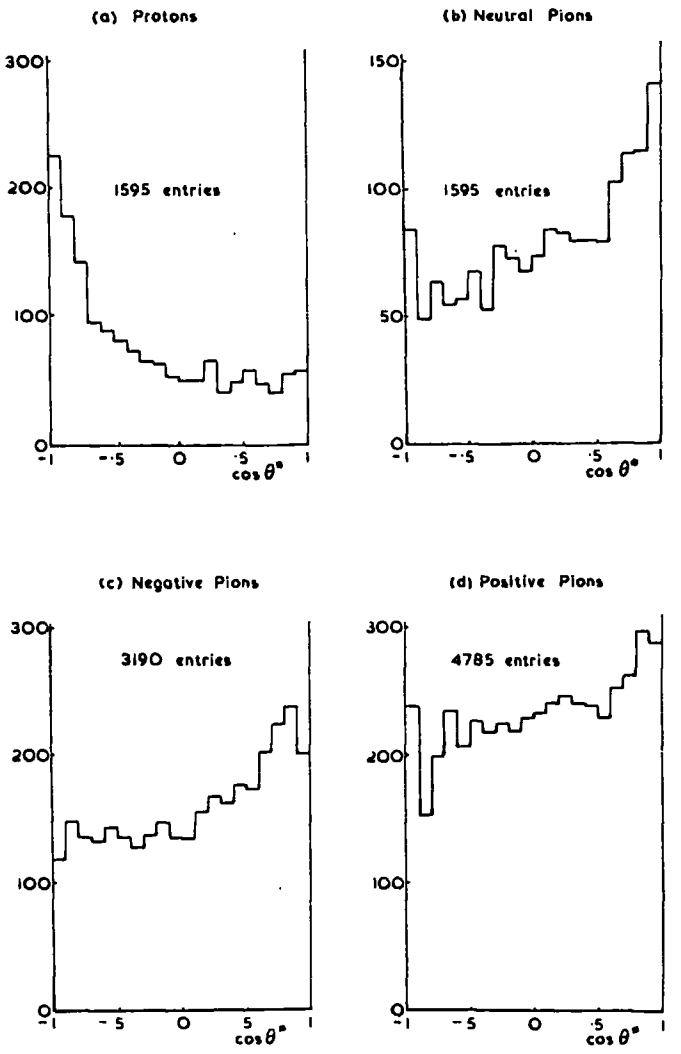

for the individual particles as shown in Figs. 57, 58, 59 and 60. The values of the elongation parameters α_x and α_y are given in Table 11 below:

Table 11

1c(π^o) Events:

Elongation Parameters, α, for the Individual Particles

Particle	α_x	α_y
p	+1.11 ± 0.03	0.93 ± 0.03
π^+	1.02 ± 0.01	0.95 ± 0.01
π^-	1.02 ± 0.02	0.92 ± 0.02
π^o	1.05 ± 0.03	0.92 ± 0.02

There is a significant distortion of the distribution of the proton in a similar manner to that observed with the 4c events. The elongations effects for the other particles are not so marked as was the case with the six body state.

Dynamics of Resonance Production

The angular distributions of those combinations of particles which show appreciable resonance production; viz. the $\pi^+p(N^{++}_{3/2})$ and $\pi^+\pi^-\pi^o(\omega^o)$ are illustrated in Figs. 61 and 62. The shaded areas represent the contributions of those combinations of particles lying within the mass regions of the resonances as defined by:

$$1120 \text{ MeV} \leq M(\pi^+p) \leq 1320 \text{ MeV}$$

FIG. 57

1c (π^0) EVENTS : HISTOGRAM OF MOMENTUM COMPONENTS OF PROTONS

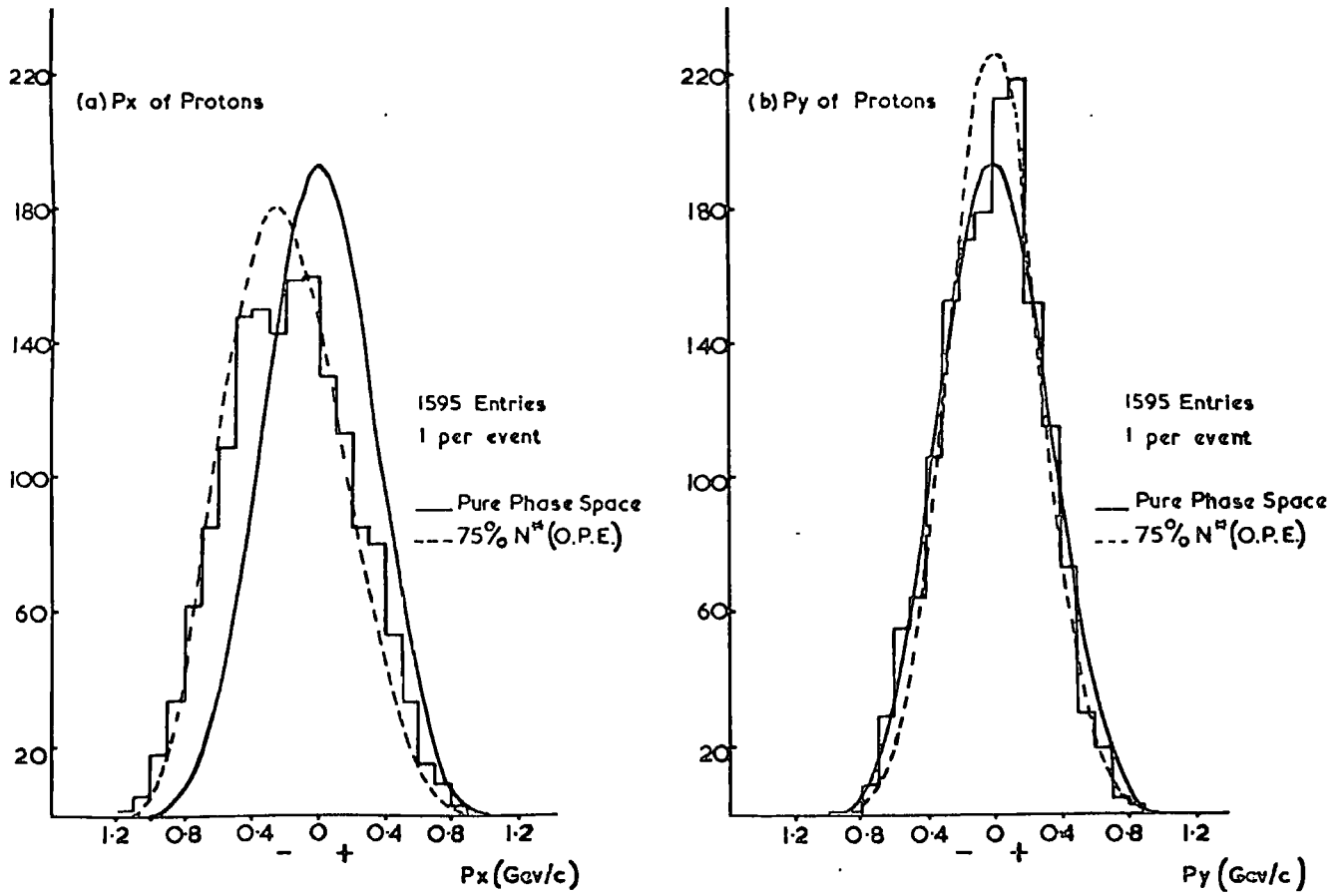

FIG. 58

1c(π^0) EVENTS: HISTOGRAM OF MOMENTUM COMPONANTS OF POSITIVE PIONS.

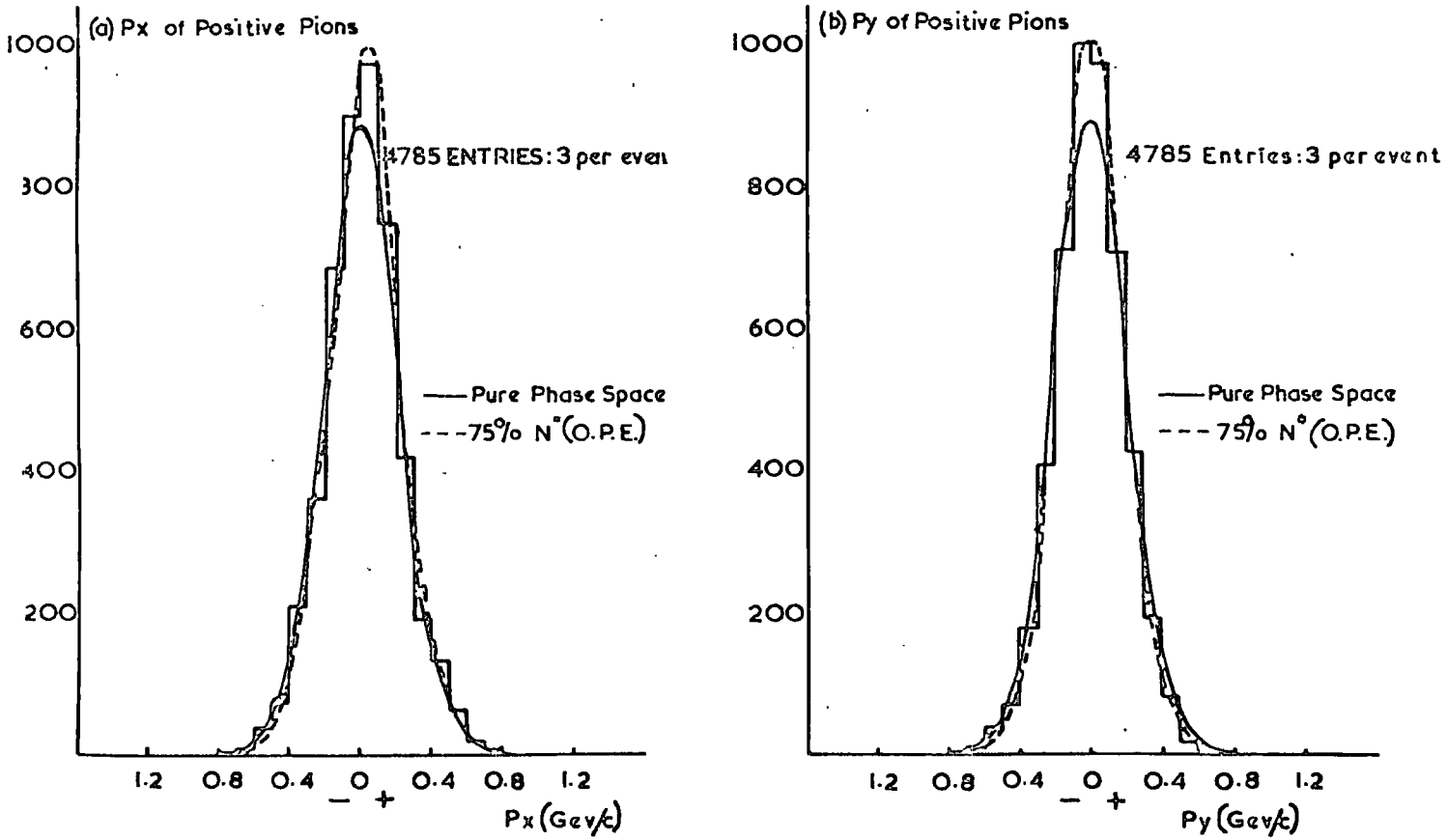

FIG. 59

Ic (π^0) EVENTS : HISTOGRAM OF MOMENTUM COMPONENTS OF NEGATIVE PIONS

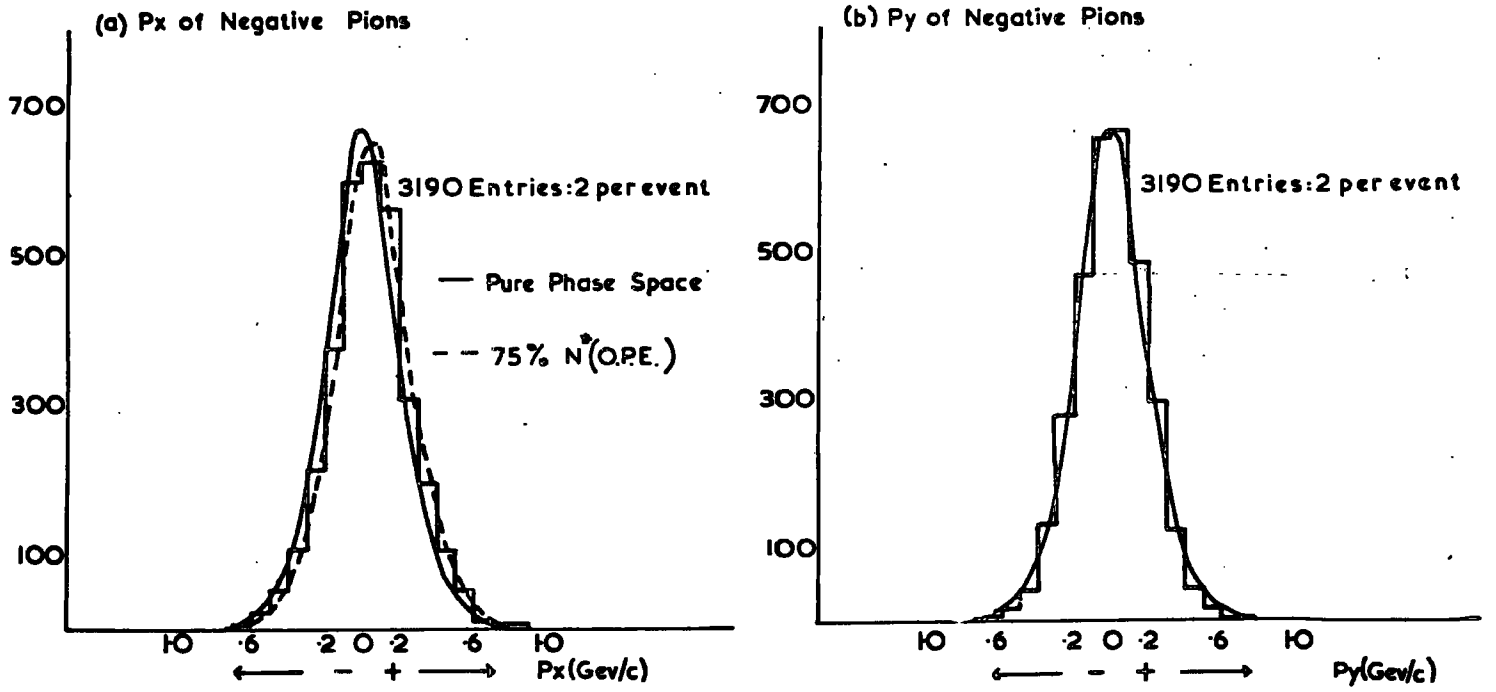

FIG. 60

Ic (π^0) EVENTS : HISTOGRAM OF MOMENTUM COMPONENTS OF NEUTRAL PIONS

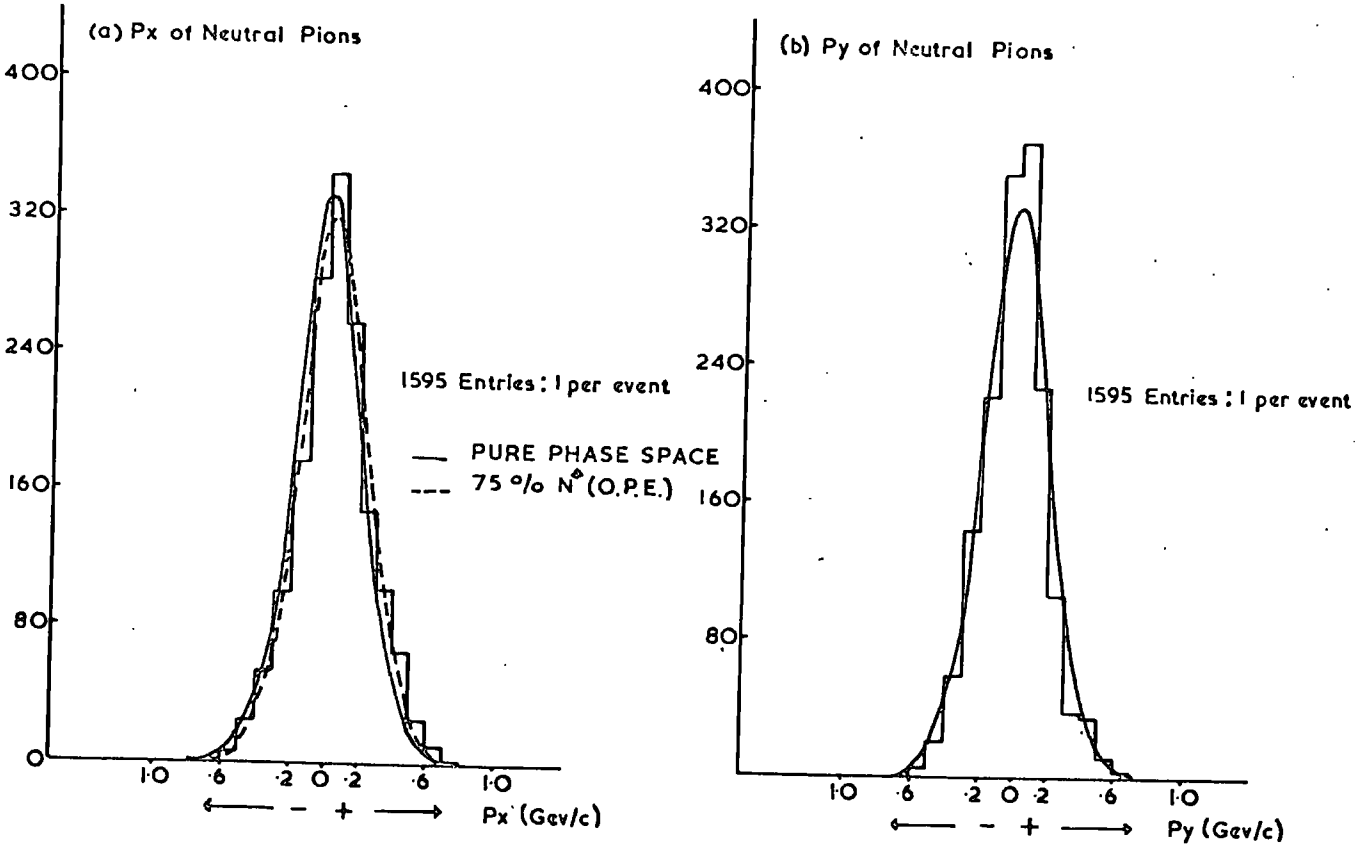

FIG. 61

1c(π^0) EVENTS: ANGULAR DISTRIBUTION OF π^+p COMBINATIONS IN THE CENTRE OF MASS SYSTEM.

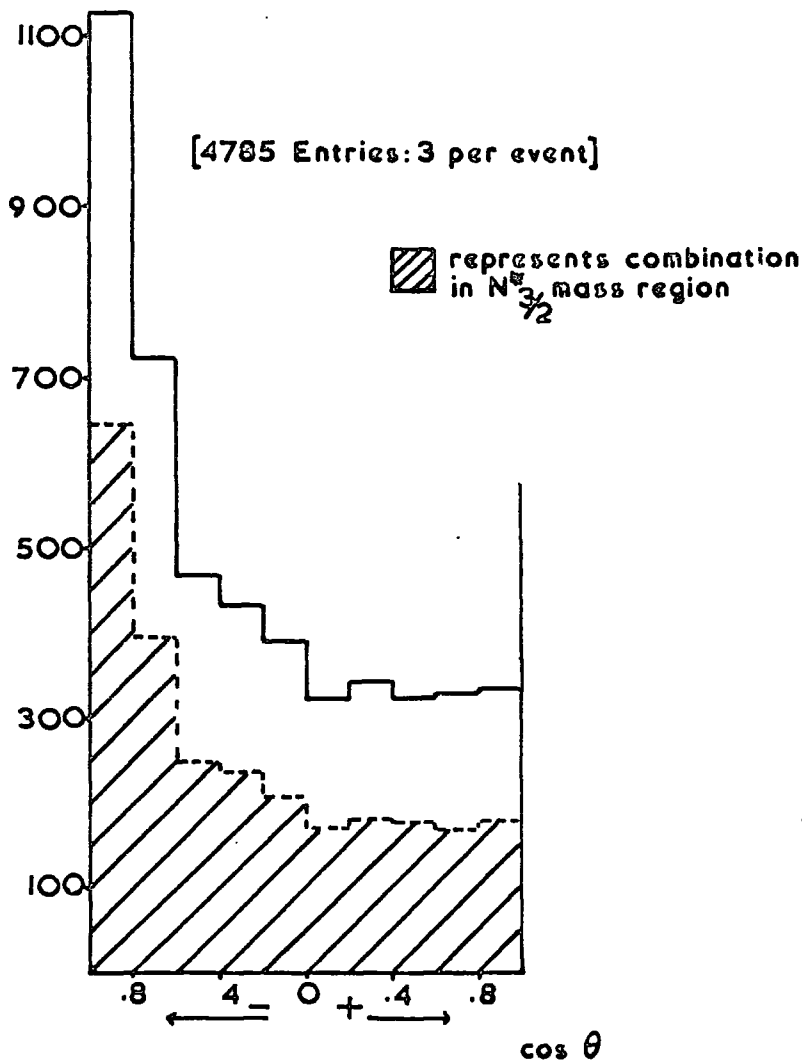

Fig. 62

Ic (π^0) EVENTS: ANGULAR DISTRIBUTION OF NEUTRAL TRI-PION COMBINATION IN THE CENTRE OF MASS SYSTEM

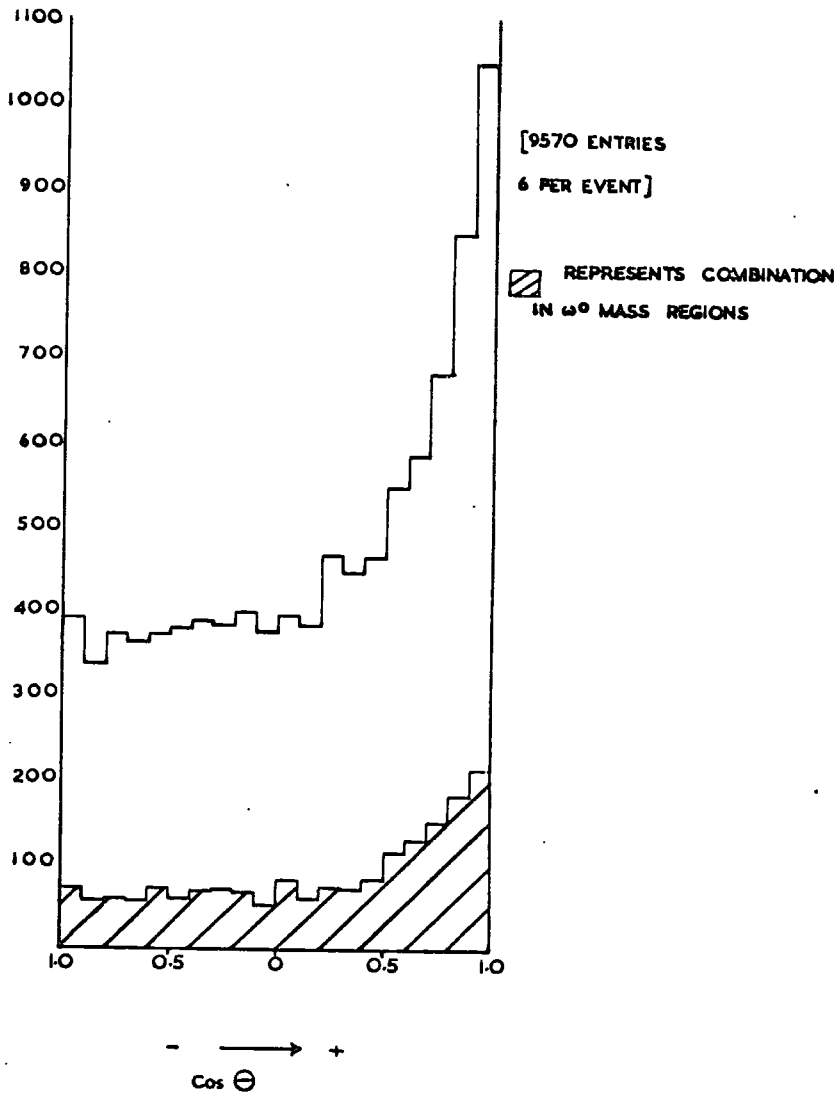

and

$$740 \text{ MeV} \leq \text{ } (\pi^+\pi^-\pi^0) \leq 810 \text{ MeV}.$$

The corresponding assymetry parameters are given in Table 12 below:

Table 12

1c(π^0) Events:

Assymetry Parameters, R, for Particle Combinations

Combination	$R = \frac{(F-B)}{(F+B)}$
π^+p	-0.31 ± 0.01
$\pi^+p(N^*_{3/2}$ region)	-0.33 ± 0.01
$\pi^+\pi^-\pi^0$	$+0.22 \pm 0.02$
$\pi^+\pi^-\pi^0(\omega^0$ region)	$+0.30 \pm 0.02$

The value for the sample of π^+p combinations in the N^* region is almost equal to that of the individual proton which is -0.34 ± 0.02. The slight enhancement is the values of the parameters for the restricted mass regions of N^* and ω^0 lends some support to the interpretation that the overall assymetry is due to the collimated production of the resonances in the centre of mass system.

Velocity Distributions

There is evidence that the $N^*_{3/2}$ isobars are produced with velocities greater than those predicted by the statistical model.

In the normalized velocity distribution of the π^+p combinations which is illustrated in Fig. 63 a broad excess of events is observed in the region of high velocities. This excess can be well simulated if the N^{*} isobars are produced in 75 of the interactions by a peripheral mechanism at the nucleon vertex, as described previously. It cannot be simulated if this number of isobars are only produced statistically in which case the resulting distribution is almost identical with the pure phase space curve.

Peripheral Production

The distribution of the four-momentum transfer from the incident proton to the π^+p combination is illustrated in Fig. 64 A large excess of entries over the pure phase space prediction is observed in the region of low Δ^2. This excess can be accounted for if the N^{*} isobar is produced by a one pion exchange process at the nucleon vertex as described for the 4c events. The expected Δ^2 distribution for such an interaction shows quite good agreement with the experimental histogram.

No peripheral calculation was possible in the case of the distribution of four-momentum transfer from the incident pion to the neutral tri-pion combinations as pions exchange to the $\pi\omega$ vertex is forbidden by conservation of g-parity. Furthermore the corresponding distribution for ρ exchange has been shown to be of doubtful significance. An excess at low values of Δ^2

Fig. 63

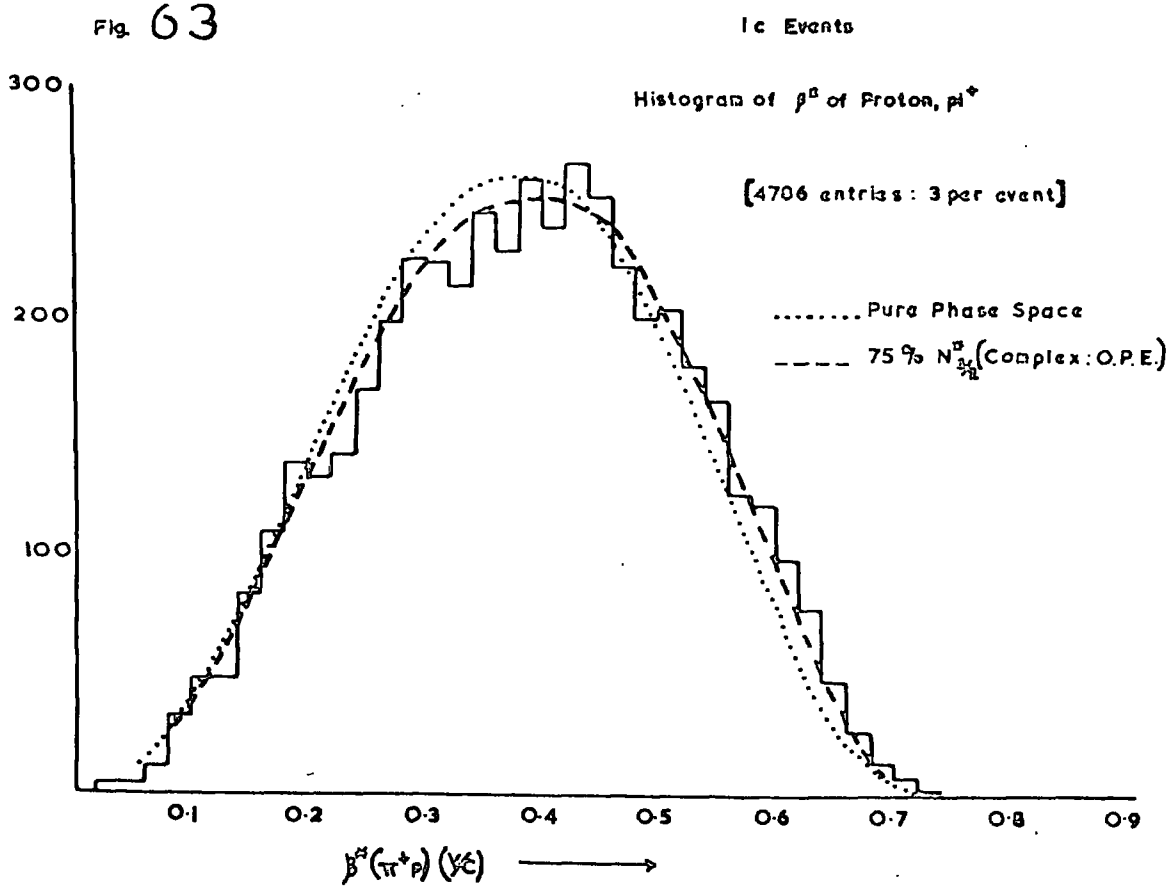
Ic Events
Histogram of β^{α} of Proton, pi^{+}
[4706 entries : 3 per event]
..... Pure Phase Space
---- 75 % $N^{\alpha}_{\frac{3}{2}\frac{3}{2}}$ (Complex : O.P.E.)
300
200
100
0·1
0·2
0·3
0·4
0·5
0·6
0·7
0·8
0·9
$\beta^{\alpha}(\pi^{+}p)$ (V/C)

Fig. 64

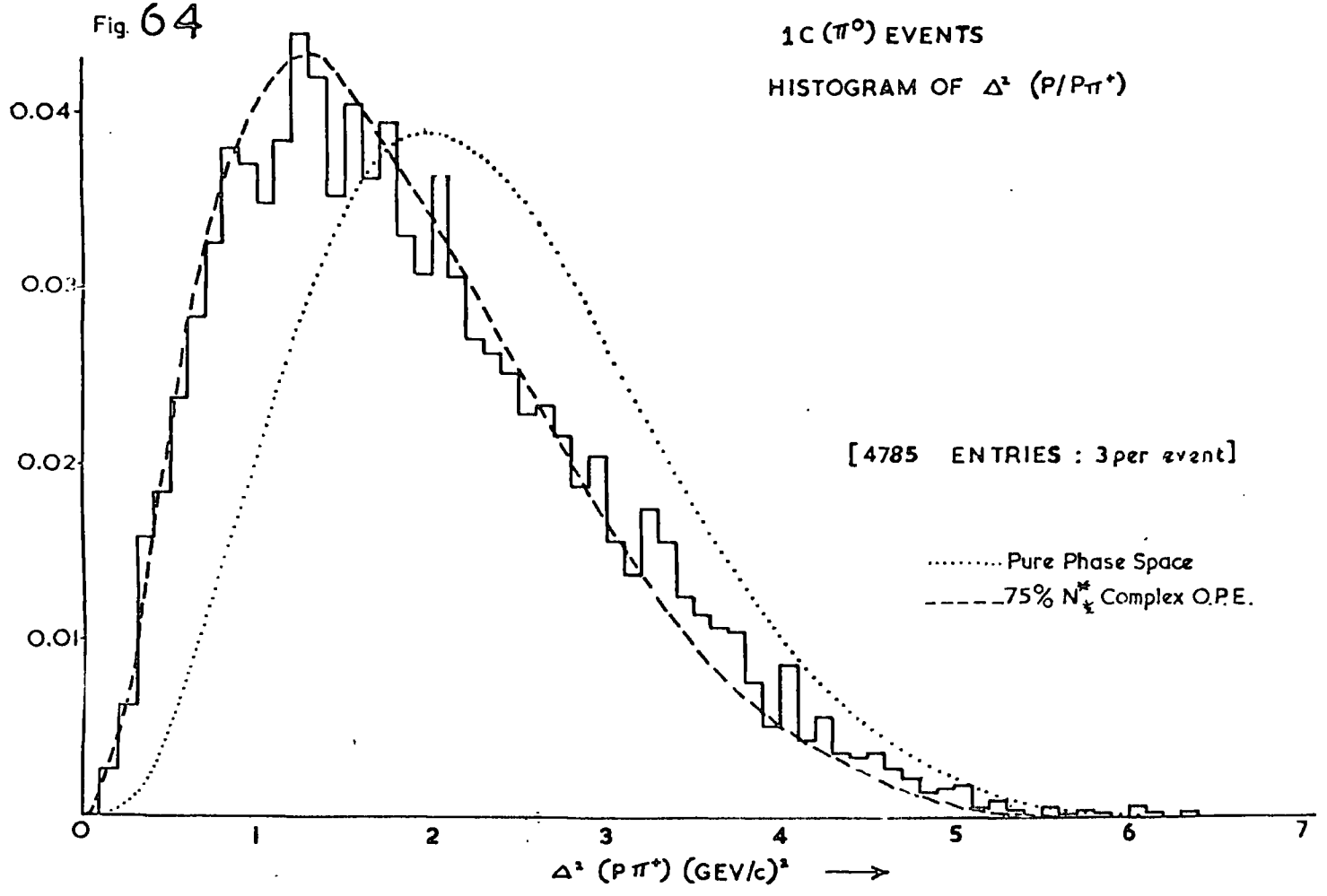
1C (π^0) EVENTS
HISTOGRAM OF Δ^2 (P/Pπ^+)
[4785 ENTRIES : 3 per event]
..... Pure Phase Space
_____ 75% $N^*_{\frac{3}{2}}$ Complex O.P.E.
0.04
0.03
0.02
0.01
0
1
2
3
4
5
6
7
Δ^2 (Pπ^+) (GEV/c)^2 ⟶

is however to be noticed in the histogram of $\Delta^2(\pi^+/\pi^+\pi^-\pi^0)$ shown in Fig. 65.

Angular Decay Distributions

Although the decay distribution of the π^+p combinations in their own rest system did not show significant assymetries, an effect was observed in the cosθ distribution for the $\pi^+\pi^-\pi^0$ combinations in the ω^0 mass region (Fig. 66(a)). This assymetry is enhanced by considering a further refined sample of forward going neutral tri-pion combinations Fig. 66(b).

Quasi Two-Body Interactions

The production of the X^0 (959) events exhibits some characteristic features. In the Peyrou plot of those neutral five-pion combinations that fall within the X^0 mass region (930 MeV $\leq M(\pi^+\pi^+\pi^-\pi^-\pi^0) \leq$ 990 MeV), Fig. 67, there is an accumulation of 8 events produced with low momentum transfer values. The effective mass of the remaining combination of a positive pion with the proton all have effective masses lying within the mass region of the $N^{*}_{3/2}$ isobar (1120 $\leq M(\pi^+p) \leq$ 1320). This small sample of eight events is the only evidence of quasi-two-body production in the total of 2647 events in the two reaction channels that have been considered.

FIG. 65

1c (π^0) EVENTS : HISTOGRAM OF Δ^2 ($\pi^+/\pi^+\pi^-\pi^0$)

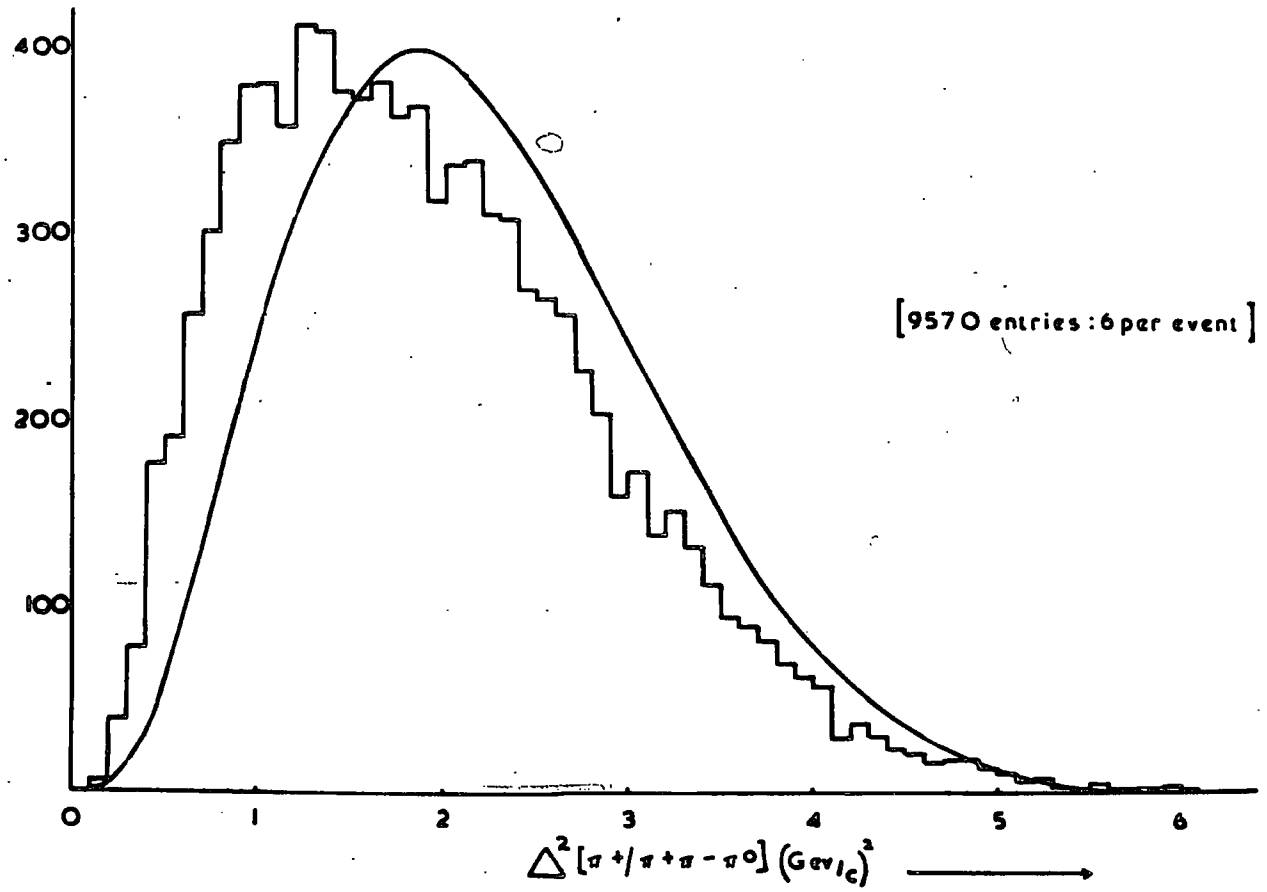

Fig. 66

Ic EVENTS : HISTOGRAM OF COSINE OF THE ANGLE BETWEEN NORMAL TO ω DECAY PLANE AND INCIDENT π^+ DIRECTION

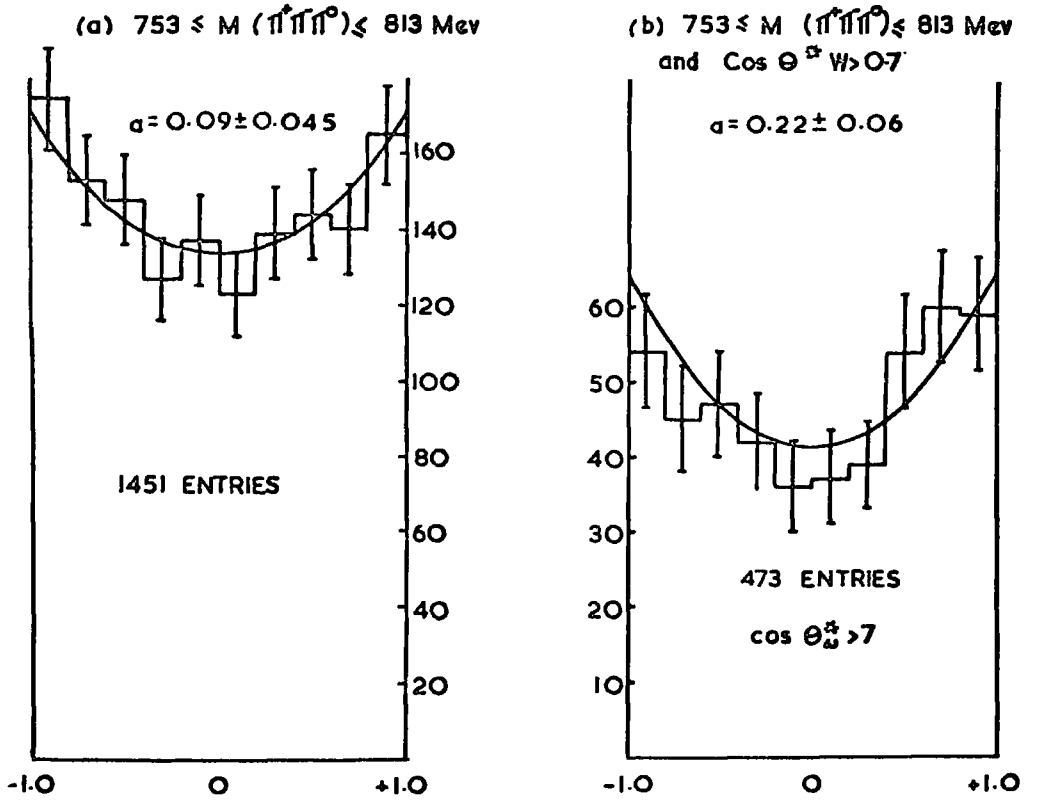

FIG. 67

1C(π^+)EVENTS:PEYROU PLOT OF X^0 (930Mev < M(++--o)<990Mev) EVENTS.

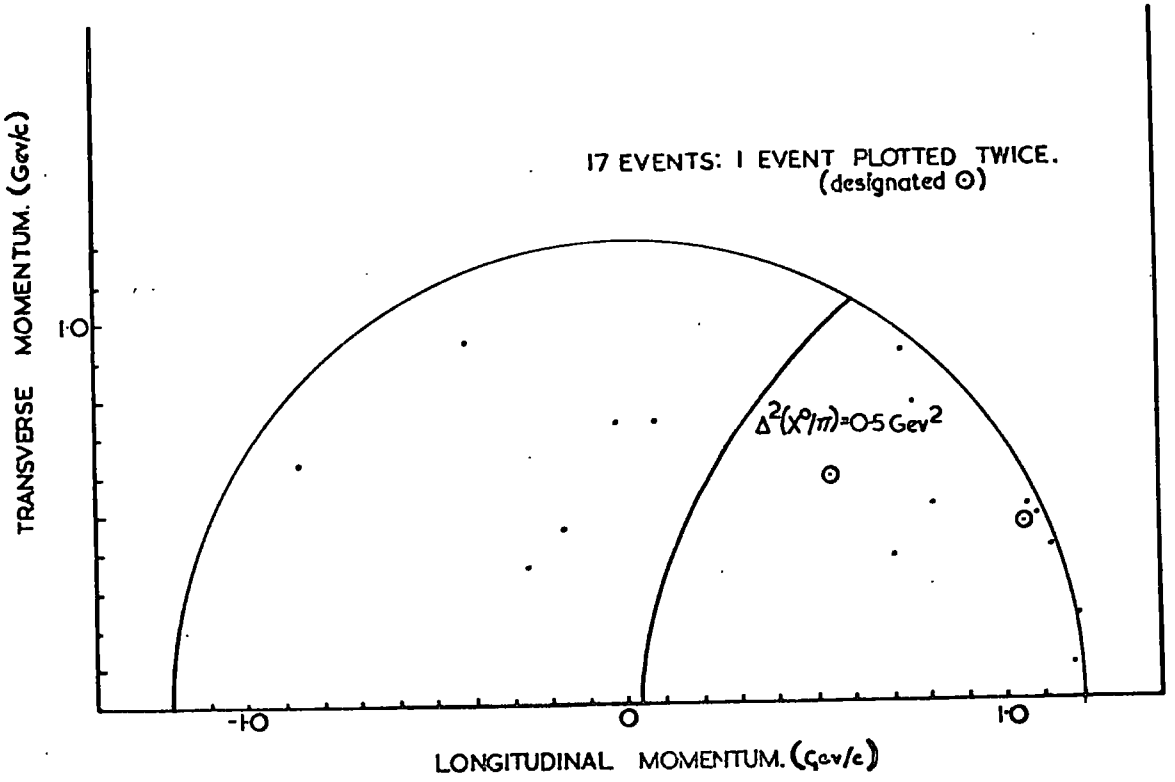

CONCLUSION

An experiment has been reported on the high multiplicity interactions of 5 GeV/c positive pions with the protons of a liquid hydrogen bubble chamber. The total and partial cross-sections that have been established at this energy give support to the observed trend of the increasing importance of the high multiplicity interactions at the higher energies.

The extensive investigations that have been carried out with this comparatively large sample of these types of interactions, have revealed a copious production of the well-known resonances: the $N^{*}(1236)$, ρ^{o}, ω^{o} and also a few X^{o} particles. No evidence was found for a corresponding production of the heavier resonances the A_1, A_2 and the B of which the and the ω^{o} form one of the decay products. Furthermore, no significant evidence was found for the production of any other resonances.

Only a small fraction of the events in the seven body final state could be attributed to the simultaneous production of an X^{o} and an N^{*}. It would therefore appear that quasi two-body interactions are absent from these types of interaction in contrast to the situation for the lower multiplicity interaction where they have been shown to be the dominant mode of resonance production.

The absence of any multi-particle intermediate state implies that the observed resonances are produced directly in 4, 5 and

6 body reactions. There is, however, strong evidence of a non-statistical mode of production. The dynamical mechanism of the production of the resonances has been shown to exhibit similar characteristics to those observed in lower multiplicity interactions. There is a significant effect of the forward-backward collimation of the resonances in the centre of mass system. The isobar appears to be produced in the same general direction as that of the incident proton and the mesonic resonance is produced predominantly in the forward direction. Furthermore the velocities of the resonances are higher than would be expected from a purely statistical mode of production.

The dynamical effects of the production of the resonances have caused significant departures of the experimental backgrounds of the histogram of the effective masses from the predictions of the statistical model. Such effects are extremely important in these types of interaction as the ratio of signal to background must always remain small because of the high number of particle combinations. It is therefore suggested that an adequate description of these dynamical processes is a necessary pre-requisite to the full exploitation of these high multiplicity interactions for the discovery of new many-particle resonances.

A limited success has been achieved with the peripheral model calculations based upon the differential production cross-sections that have been used for the lower multiplicity interactions.

Such functions appear to simulate the general features of the experimental distributions of momentum transfer and the momentum components. The evidence from the decay distributions of the resonances is inconclusive as significant assymetries are only observed for the decays of the mesonic resonances.

The observed non-statistical mode of production of the resonances in reactions that are not of the quasi two-body type would suggest the existence of a more complex interaction mechanism, and it may become necessary to consider the multiperipheral type of interaction.

It is only recently that the subject of high multiplicity interactions has begun to be of interest to theoretical physicists and work begun to try and develop a model to describe these types of interaction. The results obtained in this experiment therefore should be of use in testing any theory that may be developed.

ACKNOWLEDGEMENTS

The author wishes to thank Professor G.D. Rochester for his encouragement and his interest in the work. He wishes to thank Professor A.J. Apostolakis and Dr. J.V. Major for their guidance throughout and also his colleagues in the High Energy Physics Group for their assistance with various stages of this work.

His thanks are due also to the technical staff of the Physics Department, in particular to Mr. E. Lincoln and Mr. D. Jobling who were responsible for the construction of the I.E.P.; Mrs. A. Errington, Miss T. Jopling and Miss J. Watson for their painstaking work in scanning and measuring the events and Miss P. Stewart for typing this thesis.

In addition he would like to express his thanks to the personnel of the B.N.H.B.C. and the Universities of Bonn and Paris for many hours of computer time. Finally he would like to thank the D.S.I.R. for a postgraduate studentship and travel grants.

Appendix I

Constancy of Curvature Test

Derivation of Curvature Relation

A circle can always be fitted to any three points, let it have radius ρ.

Then for a configuration as illustrated in Fig. 68

$$L_3^2 = L_1^2 + L_2^2 - 2L_1L_2 \cos\theta$$

or

$$\cos\theta = (L_1^2 + L_2^2 - L_3^2)/2L_1L_2 \qquad \ldots (1)$$

also

$$\sin\theta = \sin\phi = \frac{L_3}{2\rho} \qquad \ldots (2)$$

i.e.

$$\rho = \frac{L_3}{4}\ \frac{2}{\sin\theta}$$

or

$$\frac{1}{4\rho^2} = \frac{1}{L_3^2}\ (1 - \cos^2\theta) \qquad \ldots (3)$$

Substitute in (3) for $\cos\theta$ from (1) to give

$$\frac{1}{4\rho^2} = \frac{1}{L_3^2} \times \left(1 - \frac{(L_1^2 + L_2^2 - L_3^2)^2}{4\ L_1^2\ L_2^2}\right)$$

$$\frac{1}{\rho^2} = \frac{(2L_1L_2 - L_1^2 - L_2^2 + L_3^2)(2L_1L_2 + L_1^2 + L_2^2 - L_3^2)}{L_1^2\ L_2^2\ L_3^2}$$

$$\frac{1}{\rho^2} = \frac{(L_3 - L_1 + L_2)(L_3 + L_1 - L_2)(L_1 + L_2 + L_3)(L_1 + L_2 - L_3)}{L_1^2\ L_2^2\ L_3^2} \qquad \ldots (4)$$

FIG. 68

DIAGRAM OF FITTED CIRCLE

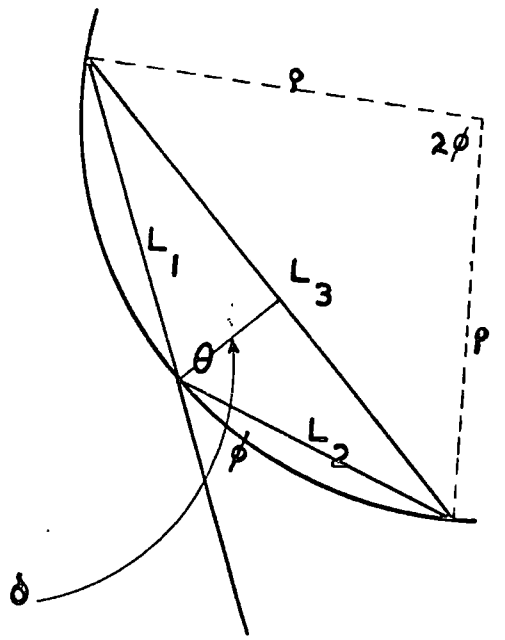

Approximation for case of small curvatures

Since we are dealing with small curvature and $L_1 + L_2 \simeq L_3$ we may justifiably make the approximation

$$L_3 = L_1 + L_2 - \delta$$

substituting into (4)

$$\frac{1}{\rho^2} = \frac{(L_1+L_2-\delta-L_1+L_2)(L_1+L_2-\delta+L_1-L_2)(L_1+L_2+L_1-L_2-\delta)}{(L_1+L_2-L_3)/(L_1^2\ L_2^2\ L_3^2)}$$

$$= \frac{(2L_2-\delta)(2L_1-\delta)(2L_3+\delta)(\delta)}{L_1^2\ L_2^2\ L_3^2}$$

Thus, to first approximation

$$\frac{1}{\rho^2} = \frac{8L_1L_2L_3 \times \delta}{L_1^2\ L_2^2\ L_3^2} + \text{higher terms in } \delta$$

$$\frac{1}{\rho^2} = \frac{4(L_1+L_2-L_3)}{L_1^2\ L_2^2 L_3^2} \quad \text{or} \quad K = \frac{(L_1+L_2-L_3)}{L_1^2\ L_2^2\ L_3^2} \qquad \ldots \quad (5)$$

If a track is nearly straight then the error of measurement, x, gives rise to an apparent curvature.

In this case

$$L_3 = L_1\left(1 - \tfrac{1}{2}\frac{x^2}{L_1^2}\right) + L_2\left(1 - \tfrac{1}{2}\frac{x^2}{L_2^2}\right)$$

but

$$\delta = L_1 + L_2 - L_3$$

$$= L_1 + L_2 - L_1 + \tfrac{1}{2}\frac{x^2}{L_1} - L_2 + \tfrac{1}{2}\frac{x^2}{L_2}$$

$$= \frac{x^2}{2}\left(\frac{L_1 + L_2}{L_1 L_2}\right)$$

Therefore

$$K = \frac{\delta}{L_1 L_2 L_3} = \frac{x^2}{2}\,\frac{L_1 + L_2}{L_1^2 L_2^2 L_3}$$

$$= \frac{x^2}{2}\,\frac{(L_3 + \delta)}{L_1^2 L_2^2 L_3} \longrightarrow \frac{1}{2}\left(\frac{x^2}{L_1^2 L_2^2}\right)$$

i.e. $\delta_s = \frac{1}{2}\left(\frac{x^2}{L_1^2 L_2^2}\right)$ ... (6)

If track is not straight then

$$\frac{dK}{dx} = \frac{x}{L_1^2 L_2^2}$$

error in K is $dK = \sqrt{2K_1}\;\frac{dx}{L_1 L_2}$ ... (7)

Application in REAP

Each track was investigated for constancy of curvature by taking triplets of consecutively measured points $x_i y_i$, $x_{i+1} y_{i+1}$, $x_{i+2} y_{i+2}$, and evaluating the lengths l_{1i}, l_{2i}, l_{3i} where

$$l_{1,i} = ((x_{i+1} - x_i)^2 + (y_{i+1} - y_i)^2)^{1/2}$$

$$l_{2,i} = ((x_{i+2} - x_{i+1})^2 + (y_{i+2} - y_{i+1})^2)^{1/2}$$

$$l_{3,i} = ((x_{i+2} - x_i)^2 + (y_{i+2} - y_i)^2)^{1/2}$$

A parameter K_i was determined from these lengths where

$$K_i = \frac{l_{1,i} + l_{2,i} - l_{3,i}}{l_{1,i} l_{2,i} l_{3,i}}$$

This is the first order approximation to the square of the curvature of the circle which may be fitted to the three points. (c.f. equation 5).

From the co-ordinates of the first triplet two extra parameters M_s and M_c were calculated by putting the x values at 40 in equations (6) and (7) so that

$$M_{s_i} = (1/2).(40/(l_{1,i} l_{2,i}))^2 \qquad \ldots \quad (8)$$

and

$$M_{c_i} = (2K_1)^{1/2}.(40/(l_{1,i} l_{2,i}) \qquad \ldots \quad (9)$$

These correspond to the maximum errors in K for an error of measurement of some 40 fringes in the two cases of a straight and a curved track. If the curvature of the track is appreciable this made $M_c > M_s$. The larger of these two parameters was

selected and subsequent values of F_i used in the condition

$$(F_i - F_{i-1}) \leq M \qquad \ldots \quad (10)$$

$$i = 1, \ldots, n.$$

REFERENCES

The A-B-B-H-M Collaboration,
Il Nuovo Cimento 44A, 530 (1966).

D. Amati, S. Fubini, and A. Stanghellini,
Il Nuovo Cimento, 5, 896 (1962).

H.L. Anderson,
Proceedings of 6th Annual Rochester Conference on High-Energy Nuclear Physics (1965).

J.S. Ball and W.R. Frazer,
Physical Review Letters 14, 746 (1965).

M. Bardidin-Otwinowska, L. Michejda, S. Otwinowski and R. Sosnowski,
Physics Letters 21, 351 (1966).

M. Bardidin-Otwinoska, M. Danyz, T. Hofmokl, S. Otwinoski, H. Pietrowska, R. Sosnowski, K. Szeptycka and A. Wreblewski,
Contribution to the International Conference on High Energy Physics, Berkeley 1966.

V.E. Barnes, P.L. Connolly, D.J. Crennell, B.B. Culwick, W.C. Delaney, W.B. Fowler, P.E. Hagerty, E.L. Hart, N. Horwitz, P.V.C. Hough, J.E. Jenson, J.K. Kopp, K.W. Lai, J. Leitner, J.L. Lloyd, G.W. London, T.W. Morris, Y. Oren, R.B. Palmer, A.G. Prodell, D. Radojicic, D.C. Rahm, C.R. Richardson, N.P. Samois, J.R. Sanford, R.P. Shutt, J.R. Smith, D.L. Stonehill, R.C. Strand, A.M. Thorndike, M.S. Webster, W.J. Willis and S.S. Yamamoto,
Physical Review Letters 12, 204, (1964).

J. Bartke, O. Czyzewski, J. Danysz, A. Esbreys, J. Loskiewcz, D. Malecki, K. Esbreys, K. Jusczak, D. Kisielewskz and W. Zielinski,
Contribution to the International Conference on High Energy Physics, Berkeley (1966).

L. Bartke and O. Czyzewski,
Contribution to International Conference on High-Energy Physics, Berkeley (1966).

L. Bertocchi and K. Zalewski,
CERN Internal Report TH/708 (1966).

W. Blum,
CERN Internal Report TC/NBC 63-2 (1963).

H. Bradner,
Annual Reviews of Nuclear Science 10, 109 (1960).

B.H. Bransden, P.J.O'Donnell and R.G. Moorhouse,
Physical Review 139, B 1566 (1966).

G.F. Chew and F.E. Low,
Physical Review Letters 113, 1640 (1959).

A. Donnachie, A.T. Lea, P. Auvil and C.A. Lovelace,
Physics Letters 12, 76 (1964).

T. Ferbel,
Ph.D. Thesis, Yale University (1963).

E. Fermi,
Progress in Theoretical Physics 5, 570 (1950).

E. Ferrari and F. Selleri,
Il Nuovo Cimento Supplemento, 24, 453 (1962).

M. Ferro-Luzzi, G.R. Lynch, R. George, Y. Goldschmitt-Clermont and V.P. Henri,
Physical Review Letters 12, 336 (1964).

P. Fleury, R. Sheppard and R. Vanderhagen,
CERN Internal Report TC/NBC 65-2 (1965).

B. French, A. Acconsi, V. Alles-Borelli, A. Frisk, J.M. Howie, W. Krischer, L. Michejda, W.G. Moorhead, E.W. Powell, P. Seyboth, and P. Villimoes,
Physics Letters 20, 557 (1966).

M. Gell-Mann,
California Institute of Technology, Synchrotron Report, CTSL 20 (1961).

C. Goebel,
Physical Review Letters 1, 337 (1958).

G. Goldhaber,
Contribution to the Conference on Particle and High Energy Physics at Boulder, Colorado (1964).

G. Goldhaber, W. Chinowsky, S. Goldhaber, W. Lee and T. O'Halloran,
Physical Review Letters 9, 330 (1962).

G. Goldhaber, S. Goldhaber, W. Lee and A. Pais,
Physical Review 120, 300 (1960).

G. Goldhaber, J.L. Brown, S. Goldhaber, J.A. Kadyk, B.C. Shen, and G.H. Trilling,
Physical Review Letters, 12, 336 (1964).

M. Goldberg, F. Judd, G. Vegni, H. Winzeler, P. Fleury, J. Huc, R. Lestienne, G. de Rosny, R. Vanderhaghen, J.F. Allard, D. Drijard, J. Hennessy, R. Huson, J. Siz, J.J. Veillet, A. Lloret, P. Musset, G. Bellini, M. Di Corats, E. Fiorini, P. Negri, M. Rollier, J. Crussard, J. Ginestet, and A.H. Tran,
Physics Letters 17, 354 (1965).

F. Gursey and L.A. Radicati,
Physical Review Letters 13, 173 (1964).

R.W. Huff,
Physical Review 133, B1078 (1964).

J.D. Jackson,
Il Nuovo Cimento 34, 1644 (1964).

J.D. Jackson and H. Pilkuhn,
Il Nuovo Cimento 33, 906 (1964).

J.D. Joseph and H. Pilkuhn,
Il Nuovo Cimento 33, 1407 (1964).

E. Keil and W. Neale,
CERN Internal Report TC/02 63-3 (1963).

G. Kellner,
CERN Internal Report TC/NBC 65-4 (1965).

B.C. Maglic, B. Levrat, C.A. Tolstrup, P. Schukelin, C. Nef M. Martin, W. Kunzle, M.N. Focacci, L. Dubal and G. Chekovani,
Physics Letters 22, 714 (1966).

D.R.O. Morrison,
Physics Letters 22, 528 (1966).

D.R.O. Morrison, F. Crijns, M. Deutcshmann, P. Schmitz, H. Weber, W. Woischnig, C. Grate, J. Klugow, S. Nowak, A. Pose, D. Pose, A. Bailas, S. Brandt, V.T. Cocconi, O. Czyzewski, P.F. Dalpiaz, E. Flaminio, H. Hrodmadnik and G. Kellner,
Physics Letters 22, 533 (1966).

Y. Ne'eman,
Nuclear Physics 26, 222 (1961).

S. Okubo,
Progress in Theoretical Physics (Kyoto) 27, 949 (1962).

R. Omnes,
Physical Review 137, B649 (1965).

B. Peters,
CERN Yellow Report 66-22 (1966).

B.E.Y. Svennsson,
Il Nuovo Cimento 37, 714 (1964).

N.J. Sopokovich,
Il Nuovo Cimento 26, 186 (1962).

A. Salam, R. Debourgo and J. Strathdee,
Proceedings of the Royal Society (London) A284, 146 (1965)
Proceedings of the Royal Scoeity (London) A285, 312 (1965).

R.I. Thews,
M.I.T. Internal Report (1966).

W.T. Welford,
Applied Optics 2, 981 (1963).

W.T. Welford,
CERN Internal Report TC/NBC 64-1 (1964).

A. Werbrouck,
CERN Yellow Report 64-13 (1964).

Zweig
CERN Internal Report Th/412 (1964).